


Defect-characterized phase transition kinetics

Cite as: Appl. Phys. Rev. **9**, 041311 (2022); <https://doi.org/10.1063/5.0117234>

Submitted: 31 July 2022 • Accepted: 24 October 2022 • Published Online: 15 November 2022

 Xie Zhang,  Jian Zhang,  Hongcai Wang, et al.

COLLECTIONS

 This paper was selected as Featured



View Online



Export Citation



CrossMark

ARTICLES YOU MAY BE INTERESTED IN

[Cubic GaN and InGaN/GaN quantum wells](#)

Applied Physics Reviews **9**, 041309 (2022); <https://doi.org/10.1063/5.0097558>

[Charge-transfer-enhanced d-d emission in antiferromagnetic NiPS₃](#)

Applied Physics Reviews **9**, 041406 (2022); <https://doi.org/10.1063/5.0107065>

[Oxide magnonics: Spin waves in functional magnetic oxides](#)

Applied Physics Reviews **9**, 041312 (2022); <https://doi.org/10.1063/5.0112794>

Applied
Physics Letters

SPECIAL TOPICS

Submit Today!

Defect-characterized phase transition kinetics

Cite as: Appl. Phys. Rev. **9**, 041311 (2022); doi: [10.1063/5.0117234](https://doi.org/10.1063/5.0117234)

Submitted: 31 July 2022 · Accepted: 24 October 2022 ·

Published Online: 15 November 2022



View Online



Export Citation



CrossMark

Xie Zhang,^{1,a)}  Jian Zhang,^{2,a)}  Hongcai Wang,^{3,a)}  Jutta Rogal,^{4,5}  Hong-Yi Li,^{6,7,a)}  Su-Huai Wei,¹ 
and Tilmann Hickel^{8,9} 

AFFILIATIONS

¹Materials and Energy Division, Beijing Computational Science Research Center, Beijing 100193, China

²Jiangsu Key Laboratory of Advanced Food Manufacturing Equipment and Technology, Jiangnan University, Wuxi 214122, China

³Institut für Werkstoffe, Ruhr-Universität Bochum, Bochum 44801, Germany

⁴Department of Chemistry, New York University, New York, New York 10003, USA

⁵Fachbereich Physik, Freie Universität Berlin, Berlin 14195, Germany

⁶College of Materials Science and Engineering, Chongqing University, Chongqing 400044, China

⁷National Engineering Research Center for Magnesium Alloys, Chongqing University, Chongqing 400044, China

⁸Max-Planck-Institut für Eisenforschung GmbH, Düsseldorf 40237, Germany

⁹BAM Federal Institute for Materials Research and Testing, Berlin 12489, Germany

^{a)}Authors to whom correspondence should be addressed: xiezhang@csrc.ac.cn; jianzhang@jiangnan.edu.cn; hongcai.wan-g@rub.de; and hongyi.li@cqu.edu.cn

ABSTRACT

Phase transitions are a common phenomenon in condensed matter and act as a critical degree of freedom that can be employed to tailor the mechanical or electronic properties of materials. Understanding the fundamental mechanisms of the thermodynamics and kinetics of phase transitions is, thus, at the core of modern materials design. Conventionally, studies of phase transitions have, to a large extent, focused on pristine bulk phases. However, realistic materials exist in a complex form; their microstructures consist of different point and extended defects. The presence of defects impacts the thermodynamics and kinetics of phase transitions, but has been commonly ignored or treated separately. In recent years, with the significant advances in theoretical and experimental techniques, there has been an increasing research interest in modeling and characterizing how defects impact or even dictate phase transitions. The present review systematically discusses the recent progress in understanding the kinetics of defect-characterized phase transitions, derives the key mechanisms underlying these phase transitions, and envisions the remaining challenges and fruitful research directions. We hope that these discussions and insights will help to inspire future research and development in the field.

Published under an exclusive license by AIP Publishing. <https://doi.org/10.1063/5.0117234>

TABLE OF CONTENTS

I. INTRODUCTION	2	C. Relevance of defects for phase transition kinetics	5
II. BASIC CONCEPTS OF DEFECT-CHARACTERIZED PHASE TRANSITION KINETICS	2	III. THEORETICAL AND EXPERIMENTAL APPROACHES	6
A. Phase transition kinetics	2	A. Theoretical techniques	6
1. Concepts and definitions	2	1. Molecular dynamics (MD) simulations	6
2. Stages of phase transitions	3	2. Nudged elastic band (NEB) calculations	7
3. Classification of phase transitions	3	3. Kinetic Monte Carlo	8
B. Defects	4	4. Phase-field simulations	9
1. Point defects	4	B. Experimental techniques	9
2. Line defects	4	1. X-ray diffraction (XRD)	9
3. Planar defects	5	2. Transmission electron microscopy (TEM)	10
		3. Video microscopy	10

4. Differential scanning calorimetry (DSC)	11
IV. PROGRESS IN DEFECT-CHARACTERIZED PHASE TRANSITION KINETICS	11
A. Point defects	11
1. Interstitials	11
2. Vacancies	12
3. Substitutional defects	13
4. Impurities	14
B. Dislocations	15
1. Dislocation traps	15
2. Strain-glass formation	15
C. Grain boundaries	16
1. Assisting nucleation kinetics	16
2. Grain-boundary transformation	17
3. Grain-boundary premelting	18
D. Stacking faults	19
1. Transformation-induced plasticity	19
2. Intermediate phase formation	21
E. Surfaces	22
1. Undercooling of liquid droplets	22
2. Phase transitions in nanoparticles	22
3. Surface reconstruction and ordering	23
F. Interfaces	24
1. Adaptive martensite	25
2. Heterophase interfaces	26
3. Interfacial complexions	28
4. Morphology of nanoprecipitates	30
V. SUMMARY AND OUTLOOK	30

I. INTRODUCTION

There are four basic states of matter: solid, liquid, gas, and plasma;¹ for each of these states, there may further exist different phases. In particular, for solid-state materials with a specific chemical composition, there can be different ways of atomic bonding and packing, characterized by lattices of different symmetries. This degree of freedom leads to the formation of a variety of possible solid-state phases. Different phases can exhibit a wide range of physical and/or chemical properties, giving rise to diverse materials properties that can be manipulated via phase engineering.

A phase corresponds to a thermodynamically stable (global) or metastable (local) minimum on the free-energy landscape at certain temperatures and pressures. When the temperature or pressure varies or external fields are applied to the system, a stable phase may become unstable; and even if it is still metastable, it may become energetically more favorable to transition to another phase, i.e., a phase transition may occur.

As phase transitions naturally allow to tune the materials properties, they play a critical role in modern materials design. The thermodynamics and kinetics of phase transitions have, thus, generated enormous research interest.^{2–13} Most of the existing studies of phase transitions have focused on defect-free pristine phases, which is oftentimes sufficient to capture the general thermodynamic trends. However, in most cases intrinsic and extrinsic defects are present in materials,^{14–22} and they may alter the thermodynamics and kinetics of phase transitions.^{23–47} In particular, phase transition kinetics that is

characterized by atomic displacements or reconstructions can easily be impacted by the presence of point and extended defects.

Despite a large number of existing research works on phase transition kinetics, the effect of defects on phase transition kinetics has seldom been systematically assessed or discussed. The specific roles that each type of defect may play in the kinetics of a certain type of phase transition have not been well established or documented. There are two main reasons for this: first, conceptually the importance of defects in phase transition kinetics has not been sufficiently recognized; the corresponding research paradigm is yet to be properly constructed or demonstrated. Second, studying and understanding the impact of defects on phase transition kinetics is challenging because it frequently requires the development and application of advanced theoretical and experimental approaches.

In this review, we highlight the critical roles of point and extended defects in phase transition kinetics. Defects may not only affect the kinetics of phase transitions, but might, in some cases, even dictate it. Hence, we introduce the concept of “defect-characterized phase transition kinetics” and discuss recent research progress along this direction.

Indeed, there have been significant advances in theoretical and experimental techniques in recent years that allow to probe the microscopic mechanisms of defect-characterized phase transition kinetics.^{48–62} Conceptually, the idea of “defect phases” has recently been proposed,⁶³ which focuses more on the thermodynamic aspects. In this review, we will use selected examples to demonstrate the various roles that defects can play in phase transition kinetics.

This article is organized as follows. We first discuss the basic concepts and knowledge of defect-characterized phase transition kinetics in Sec. II, which covers phase transition kinetics, defects, and the relevance of defects for phase transition kinetics. We further describe commonly employed theoretical and experimental techniques for simulating and characterizing phase transition kinetics in Sec. III. The central part of this article is the discussion of representative examples in various materials to illustrate recent progress in the investigation and understanding of defect-characterized phase transition kinetics in Sec. IV. Finally, we summarize the currently known roles of defects in phase transition kinetics in Sec. V. This research field is still in its infancy and extensive studies are yet in critical demand. We also outline remaining challenges and envision fruitful research directions in Sec. V, which we hope may serve as an inspiration for future studies in the field.

II. BASIC CONCEPTS OF DEFECT-CHARACTERIZED PHASE TRANSITION KINETICS

A. Phase transition kinetics

1. Concepts and definitions

A solid phase has a uniform structure and composition, and is separated from other phases by sharp boundaries, where discontinuous changes occur in structure and/or composition. A phase may become thermodynamically unstable due to a sudden change in external conditions such as temperature, pressure, stress, electric field, and magnetic field. Consequently, a phase transition may occur as driven by minimization of the thermodynamic free energy. The variation in the thermodynamic free energy during the transition is associated with

structural and/or compositional changes.⁶⁴ The thermodynamics concentrates on the origin and the driving force $-\Delta G_v$ (see Fig. 1) of phase transitions.⁶⁵ As the phase transition kinetics focuses on the evolution of a system from an unstable or metastable state to another lower-energy metastable state or the energetically most favorable equilibrium state, it studies the mechanisms and rates of transitions as well as the factors that influence them.⁶⁶ There has been intense research interest on the phase transition kinetics over the past few decades, as the underlying physical processes are of great fundamental and technological importance. Problems in this field arise from diverse disciplines such as physics, chemistry, metallurgy, materials science, and biology.

One may think that the magnitude of the thermodynamic driving force has something to do with the phase transition kinetics: the larger the driving force, the larger the rate of transition. In fact, this is incorrect. The orange line in Fig. 1 schematically shows the free energy of a system as a function of a reaction coordinate. During the phase transition, the system proceeds from higher to lower energies, but has to overcome an energy barrier. It becomes immediately clear that the driving force by itself does not provide the full kinetic description; for two cases with the same thermodynamic driving force, the kinetic barriers can be quite different (orange vs blue curves in Fig. 1). There is no apparent connection between $-\Delta G_v$ and ΔG^* . The situation here is analogous to the idea of catalysts. A catalyst does not impact the relative stability of the initial and final states, but only changes the barrier that the reaction has to overcome.

In fact, many existing materials are in a metastable rather than stable state; the central reason why they do not transform is due to the presence of the barrier. Despite the existence of a thermodynamic driving force for transitions to the most stable state, it may take extremely long time to reach thermodynamic equilibrium if the barrier is sufficiently large. The coupling of thermodynamics to kinetics is one of the most exciting areas of phase transitions, and may be considered as the “holy grail” of materials science. No generally valid approach has been formulated so far.

2. Stages of phase transitions

Phase transition kinetics consists of three stages: nucleation, growth, and impingement, which are generally overlapping upon

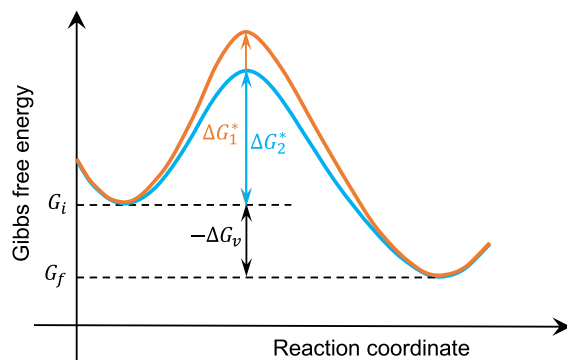


FIG. 1. Schematic showing the Gibbs free energy as a function of a reaction coordinate. The thermodynamic driving force of the transition is given by $-\Delta G_v$, with $\Delta G_v = G_f - G_i$; the activation energy barriers to overcome in two cases with identical ΔG_v are ΔG_1^* and ΔG_2^* , respectively.

transition. Phase transitions are extremely slow at the exact critical temperature or pressure for transition, because the free energies of the parent and product phases are equal, i.e., the lack of thermodynamic driving force. Measurable rates become pronounced when changing external conditions to a certain degree away from the equilibrium. According to the conventional view of homogeneous nucleation, the formation of the product phase is caused by thermal fluctuations, which bring the atoms to new positions corresponding to the product phase. A large number of such fluctuations are unstable, since they are below a critical size and cause a net increase in free energy. Such an unstable minute region of product phase is known as an “embryo” of the product phase. When the sizes of the embryos exceed a minimum critical value, they are capable of continued existence and are called “nuclei” of the product phase. The process of formation of the nuclei is known as nucleation.

Homogeneous nucleation takes place when all volume elements of the parent phase are chemically, energetically, and structurally identical. Since most of the solids contain defects, perfectly homogeneous nucleation almost never occurs. Instead, preferred nonrandom nucleation takes place at defect centers, referred to as heterogeneous nucleation. Theoretically, heterogeneous nucleation can be treated as an extension of the theory of homogeneous nucleation. If defects are randomly distributed and are in sufficiently large numbers compared to that of critical-sized nuclei, the classical view is that the only modification will be in the interface free energy. However, in this picture, the complicated atomistic processes are not considered, which may actually play a profound role here.

Phase transformations proceed toward completion by the growth or propagation of the critical-sized nuclei of the product phase. The growth of nuclei requires transfer of atoms from the material in the interface onto these nuclei of the product phase. This process causes net free energy decrease, and is almost spontaneous, as the barrier to growth is usually small.

As the product phase grows inside the matrix, the growth continues until the product phase impinges on a growth barrier such as pre-existing domains and defects. Then the impingement occurs: new nuclei cannot develop at locations occupied by growing product phase domains; growth of product phase domains cannot extend to locations occupied by other product phase domains and/or can be influenced by the surrounding matrix via growing neighboring product phase domains.

3. Classification of phase transitions

Based on the relation between the thermodynamic quantity exhibiting discontinuity and the Gibbs free-energy function, proposed by Ehrenfest,⁶⁷ a transition is of the same order as the derivative of the Gibbs free energy that shows a discontinuous change at the transition. For a first-order transition, the free energy of the system remains continuous, but thermodynamic quantities like entropy and volume undergo discontinuous changes. Thus, first-order transitions are characterized by latent heat, volume change, and hysteresis effects. The presence of hysteresis is associated with the activation energy barrier ΔG^* illustrated in Fig. 1, which is, however, not present in a second-order transition.

By the extent of atomic displacements, phase transition can be classified into diffusional and diffusionless transitions, which is distinguished by the presence or lack of long-range diffusion. Precipitation

and eutectoid reactions are typical diffusional transitions in solids. Technologically important martensitic transitions fall into the diffusionless category. Martensitic transitions correspond to a homogeneous deformation that may be different in small adjacent domains. It also generates an invariant planar strain, through which the parent and product phases are related by a substantial lattice correspondence, a habit plane, and a precise orientation relationship.

B. Defects

In crystalline materials, any interruption in the periodic atomic arrangement of a crystalline solid is referred to as a “defect.” However, contrary to the “negative” meaning the term itself may suggest, defects can also play a profoundly positive role in the design of modern materials, as their presence can significantly improve the materials properties. When using dimensionality as a criterion, defects can be categorized into zero-dimensional (e.g., point defects), one-dimensional (e.g., dislocations), two-dimensional (e.g., grain boundaries, stacking faults, surfaces, and phase boundaries), and three-dimensional (e.g., precipitates). Through decades of research, the intimate relationship of different defects in their behavior and effects on the material has been well-established. Here, we briefly recapitulate each type of defect. For precipitates, the dominant effect stems from the matrix/precipitate interfaces, which are, in fact, planar defects themselves. Hence, we do not discuss precipitates separately, but focus on their interfaces to the matrix.

1. Point defects

Crystals have well-defined atomic structures, i.e., all the atoms in a perfect crystal are at specific lattice sites (plus thermal vibrations). When an atom moves away from its ought-to-be site, an intrinsic point defect is created. There are usually three types of intrinsic defects: interstitials, vacancies, and antisites. For instance, as shown in Fig. 2, B_i denotes an interstitial of atom type B, V_A means a vacancy at a site of atom A, and A_B is an antisite defect with an atom A “mistakenly” sitting on the B site.

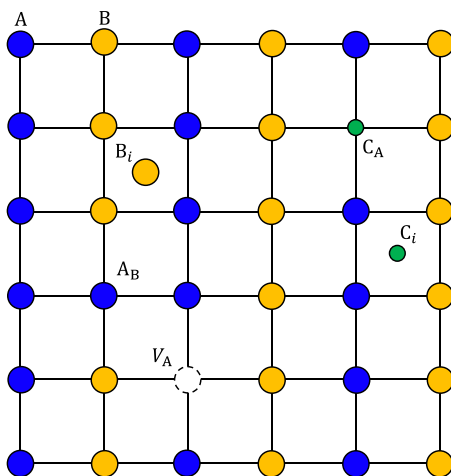


FIG. 2. Schematic illustration of intrinsic and extrinsic point defects in a binary compound AB within a square lattice. C denotes an impurity.

Extrinsic point defects are, on the contrary, created by impurity atoms introduced in a crystal. Two different types of sites can be taken by foreign atoms: either substitute atoms of the host lattice (e.g., C_A in Fig. 2) or occupy interstitial spaces (e.g., C_i in Fig. 2). These scenarios constitute the basic simple point defects in a material. However, in reality these simple point defects may also bind together, forming energetically favorable defect complexes; as a result, the number of possible combinations and configurations is huge.

2. Line defects

The concept of dislocations was first introduced to explain the large discrepancy between experimentally measured strength and its theoretical value. That is, when the crystal is deformed, atomic planes do not slip over each other as rigid bodies, but instead slip starts at a localized region and then spreads gradually over the remainder of the plane. The slip plane can be, therefore, divided into two regions: one where slip has occurred and the other which remains unaltered. The line defect that marks the boundary between these two regions is referred to as a dislocation line or dislocation.

Similar to point defects, dislocations also distort the regular atomic array of a perfect crystal in their vicinity. As shown in Fig. 3, a dislocation is characterized by the Burgers vector, \mathbf{b} , which measures the distortion associated with the defect, and the unit line vector, \mathbf{t} , that points along the local orientation of the dislocation.

There are three generic dislocation types identified: (i) edge dislocations with \mathbf{b} normal to \mathbf{t} , (ii) screw dislocation with \mathbf{b} parallel to \mathbf{t} , and (iii) mixed dislocations which combine characteristics of edge and screw dislocations.

Dislocations are important for the plastic deformation of materials. Nevertheless, they are not favored by thermodynamics, as in (meta)stable materials the formation of a defect usually costs energy. The enthalpy of formation of the dislocation is not compensated by the change in configurational entropy associated with the dislocation. However, this may be a blessing for its role in phase transformations, which has been discovered in recent years. The strain field induced by a dislocation might create energetically favorable regions for solute atoms, which may trigger changes in the local chemical composition around the dislocation; a different phase (than the parent one) that is thermodynamically unstable in bulk may become locally metastable.⁶⁸

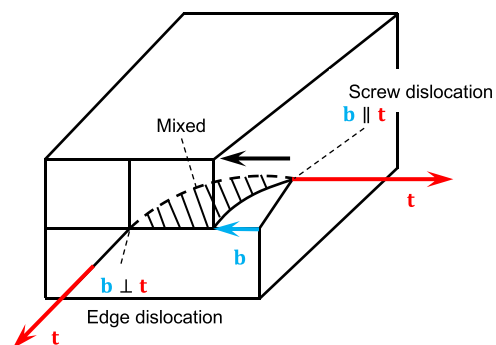


FIG. 3. Schematic showing different types of dislocations. \mathbf{b} is the Burgers vector, and \mathbf{t} is a unit vector along the slip direction.

3. Planar defects

Compared to crystallographic line defects, a planar defect is a discontinuity of the perfect crystal structure across a plane, which includes grain boundaries, phase boundaries, stacking faults, surfaces, and other types of interfaces.

A grain boundary is an interface between two grains of the same crystalline phase that have different spatial orientations. The atoms in the grain boundary (of thickness on the order of only 2–4 atomic distances) are generally not in perfect crystalline arrangement. The grain structure is formed when growing grains collide and thus form the grain boundaries. Depending on the misorientation angle (ϕ) between the grains on both sides of the boundary, grain boundaries can, in general, be categorized into either large-angle ($\phi > 15^\circ$) or small-angle ($\phi < 15^\circ$) grain boundaries. In the latter case, the deviation of the crystal orientation often arises from several superimposed dislocations, changing the lattice orientation by only a few degrees ($\phi < 15^\circ$). A special type of grain boundary is twin boundaries, in which the crystals on either side of a plane are mirror images of each other. The boundary between the twinned crystals is a single plane of atoms. There is no region of disorder as in normal grain boundaries and the boundary atoms can be viewed as belonging to the crystal structures of both twins. As a result, a twin grain boundary has a high symmetry and thus low energy.

Crystallographically, a phase is a region with a uniform crystal structure and chemical composition. Thus, a phase boundary spatially separates two regions with different crystal structures and/or chemical compositions, which is also called a heterophase interface. Depending on how the structures of the different phases merge, a distinction is made between coherent, semicoherent or incoherent phase boundaries (see Fig. 4). At a coherent phase boundary, the interface atoms of the two structures align almost perfectly without any gaps. This is usually the case if the two phases have comparable or commensurate lattice constants. If the phases differ somewhat in their lattices, dislocations must be present at regular intervals for the lattice structures to match one another. The corresponding boundary is then characterized as

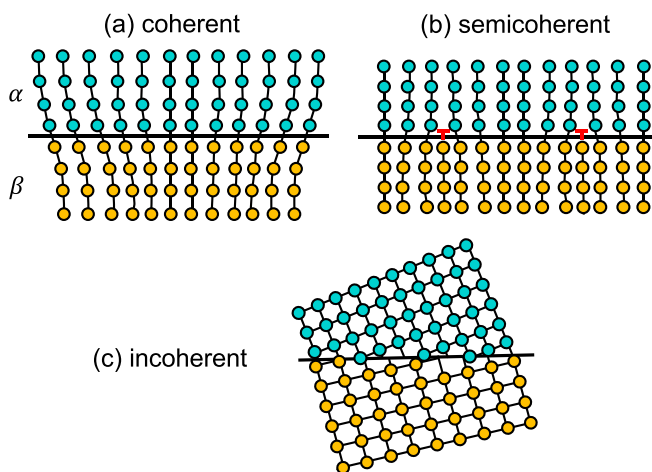


FIG. 4. Schematic showing different types of phase boundaries: (a) coherent, (b) semicoherent, and (c) incoherent. Blue and orange spheres represent atoms in two different phases α and β .

partially coherent/semicoherent phase boundary. By contrast, at an incoherent phase boundary, the lattice structures of the two phases cannot be matched to reflect any periodic arrangement. Incoherent interfaces are similar to large-angle grain boundaries but separate two different phases.

A perfect crystal can be described as a stack of atom layers along any given crystallographic direction arranged in a regular sequence. For example, the stacking sequence of the closest packed planes in the face-centered cubic (fcc) lattice along the $[111]$ direction is ABCABC, in which A, B, and C denote different atom layers (see Fig. 5). If the stacking sequence is locally altered to, for example, ABABCA stacking, then a stacking fault is created. A stacking fault is a planar defect, as its name implies, where the regular stacking sequence is locally interrupted. As a matter of fact, stacking faults are always related to other defects such as point defects and dislocations. They can be created either by condensing vacancies in the crystal or by splitting a dislocation into two partials.

In reality, crystals are finite in size and terminate at free surfaces with different orientations [Fig. 6(a)]. Free surfaces of materials are defects in the sense that the periodic repetition of the structural units of a crystal is terminated. Such surfaces may be entirely clean, i.e., consisting of the same atom types as the bulk material, or they may also contain other elements or adsorbates. In either case, atoms at the surface have a different (usually lower) coordination than bulk atoms which in most cases leads to an increase in free energy.⁶⁹ Therefore, the arrangement of atoms in the outer few atomic layers often differs from that in the bulk material. That is to say, in order to minimize the energy, atoms in the surface may relax by small displacements with respect to the translationally symmetric positions of the bulk atoms [Fig. 6(b)], or rearrange to form distinctive structures by reconstructive displacements with a different in-plane symmetry than the bulk [Fig. 6(c)].

C. Relevance of defects for phase transition kinetics

We discussed phase transition kinetics and defects separately in Secs. II A and II B, which are useful to illustrate the basic concepts and underlying physical ideas. However, realistic phase transitions happen in the presence of defects, or, in a more general picture, it is the phases and defects of different types that constitute a material.

As schematically depicted in Fig. 7, real materials exhibit complex microstructures. Colin Humphreys, a renowned materials scientist at the University of Cambridge, once said: “Crystals are like people, it is the defects in them which tend to make them interesting.”⁷⁰ Indeed, crystal phases contain and are surrounded by different defects, and the thermodynamics and kinetics of phase transitions are certainly affected by the defects. What makes it particularly interesting is that the impact of defects on phase transition kinetics and ultimately on the mechanical or electronic performance of materials is not always negative. Sometimes, defects play a positive and beneficial role. In some extreme cases, certain stages of phase transitions, such as nucleation, are even unlikely to occur without the presence of defects.

Hence, in this review, we introduce the concept of defect-characterized phase transition kinetics, which highlights the importance of defects for phase transition kinetics, discusses the specific roles that defects may possibly play in various types of phase transitions, and hopefully may also inspire effective pathways to manipulate phase transition kinetics via defect engineering.

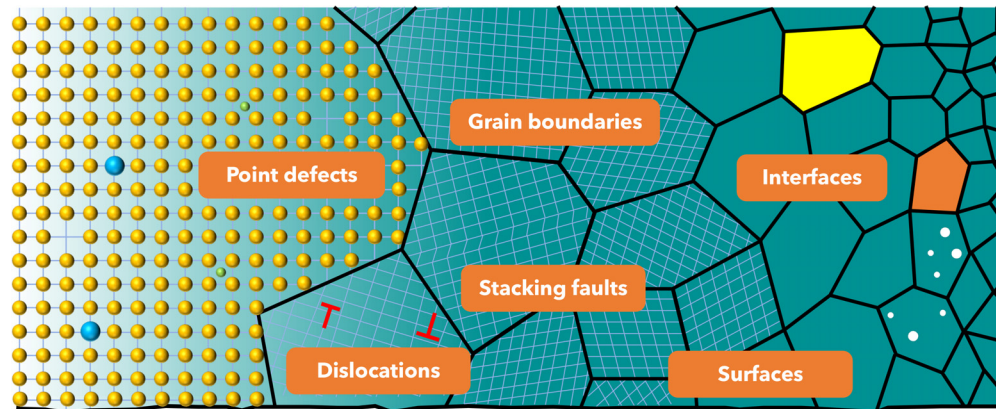


FIG. 7. Schematic microstructure of a material, showing the presence of different defects.

disadvantage is, however, that machine-learning potentials are generally not transferable and need to be refitted for any new phase to be studied. It also becomes increasingly difficult to fit machine-learning potentials for multicomponent systems with a large number of atomic species,^{90–92} not only because of the increasing complexity of the model, but also because creating suitable training data to fit the machine-learning model becomes intractable.

Different phases are usually energetically preferred at different temperatures as determined by their Gibbs free energies. Between each two phases, there is a critical temperature at which the Gibbs free energies of the two phases are identical; below or above this temperature structural or magnetic transition from one phase to the other is expected. To simulate the phase transition kinetics using MD, one may start from the energetically less favorable phase and perform MD simulations at a temperature higher (or lower) than the critical temperature. With such a setup, one may observe the kinetic process of the phase transition. Similar is also true for pressure-induced phase transitions.

However, it is not guaranteed that one can always observe the phase transition in MD simulations, because the phase transition kinetics is affected by the transformation barrier, as discussed in Sec. II A 1. If the barrier is very large, the simulation may have to be run at very high (possibly unrealistic) temperatures in order to kinetically cross the barrier. Or, worst-case scenario, it might even not be possible to observe the phase transition within the limited timescale of MD. As the typical MD time step is on the order of femtoseconds, reaching a microsecond timescale is already very difficult. In order to overcome this limitation, there are a number of advanced MD techniques that have been developed, such as accelerated MD,^{93–95} metadynamics,^{96–98} adiabatic free energy dynamics,^{99–101} or path sampling techniques.^{102–108} Furthermore, kinetic Monte Carlo (KMC) is also a powerful alternative that can help to overcome the timescale issue, which will be discussed in Sec. III A 3.

2. Nudged elastic band (NEB) calculations

A central aim of studies of phase transition kinetics is to identify the phase transition pathway and associated kinetic barriers. This is, however, a non-trivial task and oftentimes challenging. The basic information we know is the atomic structures of the parent (initial)

and product (final) phases, which are usually two local minima on the potential energy surfaces [see Fig. 8(a)]. Based on first-principles or empirical-potential calculations, one can further extract information about the first and second derivatives of the potential energy surfaces. Also, phase transitions tend to follow the energetically most favorable pathway, which is commonly referred to as the minimum-energy path (MEP). The MEP provides direct insights into the transformation barriers at the ground state ($T = 0$ K) and intuitively shows how the transition happens at the atomic scale. Then, the key question is how to make use of the above information to identify a proper reaction coordinate and the MEP. This challenging task can be addressed by nudged elastic band (NEB) calculations, which have been one of the most popular methods¹⁰⁹ for finding saddle points and the MEPs of reactions, diffusion processes, or phase transitions, as it is physically intuitive and computationally very efficient. Here, we describe the basic idea and formalism of the NEB method.

The MEP links the initial and final phases on the potential energy surface [Figs. 8(a) and 8(b)] and has the feature that any point on the path is at an energy minimum in all directions perpendicular to the path. Hence, the MEP can also be defined as the union of steepest descent paths from the saddle point(s) to the minima. To transform the initial phase to the final phase, one or more saddle points need to be crossed [Fig. 8(b)], which creates also an energy barrier [shown as ΔE in Fig. 8(c)] for the transition.

The first step to calculate the MEP is to set up an initial path. Specifically, one needs to identify a consistent lattice correspondence between the initial and final states. For simple diffusion events with atomic hops, this is very straightforward. A linear interpolation between the initial and final coordinates of the hopping atom is already suitable. However, for phase transitions between two different crystal structures with all of the atoms moving simultaneously, the identification of the lattice correspondence can be arbitrarily complicated. Usually, one needs to carefully investigate the orientation relationships between the initial and final phases to construct a consistent unit cell with an identical number of atoms that can naturally evolve between the initial and final phases. The lattice mapping can then be formulated as a function of the coordinates of all atoms in the unit cell.

As schematically depicted in Fig. 8(a), a set of images (copies of the system with atomic configurations connecting the initial and final

phases) is introduced to describe a transition pathway in the NEB approach. Between each two adjacent images, a spring is used to ensure that the images mostly relax on the hyperplane perpendicular to the path. Starting from an initially specified path, e.g., a linearly interpolated one, the forces on image i are evaluated and the NEB forces ($\mathbf{F}_i^{\text{NEB}}$) consist of two independent components [Fig. 8(a)],¹¹⁰

$$\mathbf{F}_i^{\text{NEB}} = \mathbf{F}_i^\perp + \mathbf{F}_i^{\parallel}, \quad (1)$$

where \mathbf{F}_i^\perp is the force component due to the potential perpendicular to the band, and \mathbf{F}_i^\parallel is the spring force parallel to the band.

Using the above scheme, the MEP can be calculated iteratively by constrained structural relaxations of all involved images based on energetics and forces obtained from first principles or empirical potentials. To improve the efficiency in converging the transition-state configuration, a so-called climbing-image NEB (CI-NEB) has been developed.¹¹¹ In this improved scheme, the highest energy image feels no spring forces and climbs to the saddle via a reflection of the force along the tangent of the path.

The standard NEB (including CI-NEB) approach does not allow to vary the shape and lattice constants of the simulation cell, which is fine for atomic diffusion or phase transitions with simple atomic shuffle. However, for realistic solid–solid transformations, the process involves more degrees of freedom, and the lattice constants and cell shape are usually quite different, even if it is possible to identify a consistent lattice correspondence. In general, there are two types of variables during the phase transition, i.e., those describing atomic motion and those describing the geometry of the periodic cell. Hence, the so-called generalized solid-state NEB (SSNEB)⁵³ approach was developed to allow also changes in the geometry of the simulation cell, which can be coupled with atomic motion considered in “normal” NEB.

Since the MEP is calculated at $T=0$ K, temperature-induced entropies are not included. At finite temperatures, the relative phase stabilities and the energy barrier of the transition might be different.^{112–114} Hence, the MEP might not correctly capture the mechanism of phase transitions at elevated temperatures. Nevertheless, in many material systems, the MEP already yields qualitative or even quantitative insights into the phase transition pathways and energy barriers, which are extremely helpful for understanding the mechanisms and kinetics of phase transitions. In cases where temperature-induced effects are crucial, one can compute the minimum free-energy path (MFEP) that takes into account lattice vibrations and electronic excitations at finite temperatures (see, e.g., Ref. 115).

3. Kinetic Monte Carlo

As discussed in Sec. III A 1, the time scales accessible in classical MD simulations can be insufficient to capture phase transformations, in particular, if the corresponding atomistic mechanisms are associated with sizeable energy barriers. NEB, on the other hand, can be used to explore energy barriers but does not provide any dynamical information. In KMC,^{116–119} the dynamics are coarse-grained to represent the transition between different metastable states (local minima on the energy landscape) of the system and can, therefore, be observed on extended time scales.

An illustrative example is interstitial diffusion where atoms move between different interstitial sites of the host lattice. While the small time step in MD simulations captures the fast atomic vibrations, every KMC step moves the diffusing atom from one interstitial site to the next. Each transition process is associated with a microscopic rate constant, which also accounts for the averaged short-time dynamics (the vibrations in this case) within each state. Consequently, a KMC

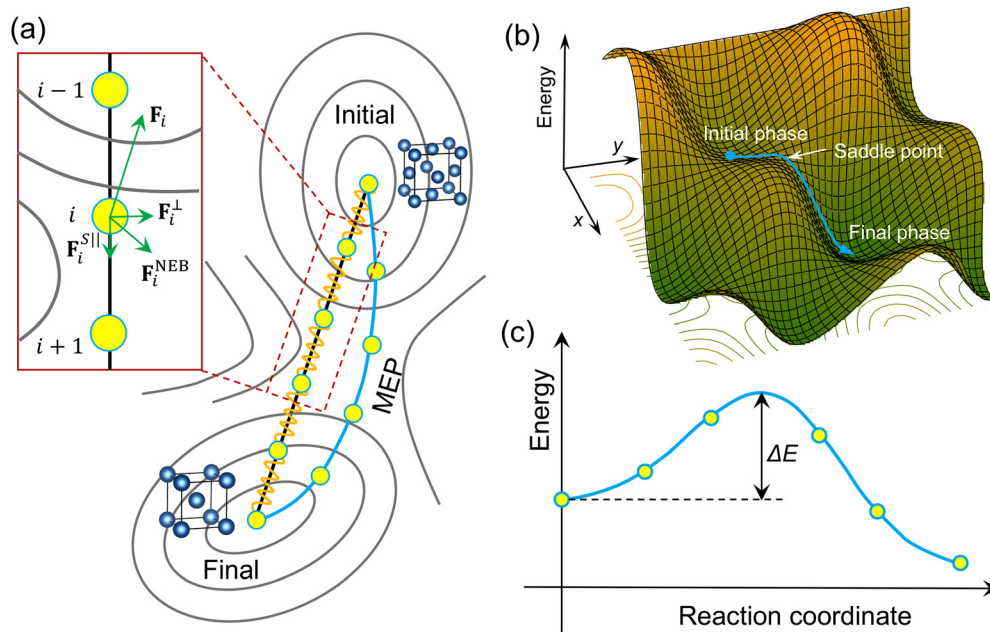


FIG. 8. (a) Schematic illustration of the principle of nudged elastic band simulations. (b) A schematic three-dimensional potential energy surface and the minimum-energy path connecting the initial and final phases through a saddle point. (c) Minimum energy path along the reaction coordinate and the energy barrier of the transition (ΔE).

simulation yields a stochastic trajectory of the state-to-state dynamics. The processes between metastable system states are not restricted to single-atom motion, but can also comprise complex multi-atom rearrangements within the system.

The key ingredients in a KMC model are (i) the definition of the state space (i.e., the metastable states), (ii) the processes connecting different states, and (iii) the rate constants for these processes. In each KMC step, all possible processes for the escape from the current state are determined together with the corresponding rate constants. The system is then advanced to the next state by randomly picking one of the processes p weighted by their rate constants, with

$$\sum_{i=0}^{p-1} k_i \leq \rho_1 k_{\text{tot}} < \sum_{i=0}^p k_i, \quad (2)$$

where k_{tot} is the sum overall rate constants and ρ_1 is a uniform random number $\in [0, 1]$. The time for this Poisson process is correspondingly updated with $\Delta t = -\ln(\rho_2)/k_{\text{tot}}$, where ρ_2 is a second uniform random number.

There are two distinct scenarios when setting up a KMC model depending on whether or not the state space and corresponding processes are known *a priori*. For instance, in the case of interstitial diffusion, the metastable states correspond to configurations where the moving atoms reside in any of the interstitial sites and the processes are single-atom hops between the interstitial sites. Here, the state space can be mapped onto a lattice and the rate constants for the processes can be computed in advance and tabulated. In condensed phase systems, harmonic transition-state theory (hTST)¹²⁰ is often a good approximation to the rate constants with $k_i = \nu_i \exp(-\Delta E_i/k_B T)$, where ν_i is the attempt frequency that, within hTST, can be obtained from the vibrational frequencies in the metastable state and at the transition state, ΔE_i is the energy barrier of the process and k_B is the Boltzmann constant. The energy barriers can, for example, be computed with NEB (Sec. III A 2) based on accurate first-principles calculations (depending on the complexity of the system).

Such a lattice model is computationally fairly cheap, but will fail if not all the important processes are included in the model. Complex rearrangements of entire groups of atoms, for example, within the interface of a moving phase boundary, are usually not easily mapped onto a lattice model. Approaches, such as adaptive KMC (AKMC)^{121,122} or kinetic activation relaxation technique (kART),^{123,124} explore the state space and transition processes on-the-fly without requiring any prior knowledge. Starting from a configuration within a metastable state, the surrounding energy landscape is explored to find adjacent local minima and the connecting processes as well as their respective energy barriers. This can be done by, for example, the (solid-state) dimer method^{54,125} or a combination of high-temperature MD and quenching to discover new states¹²⁶ followed by NEB to determine the barrier. AKMC is extremely flexible but computationally very demanding as in every KMC step, a large number of searches have to be performed in the full $3N$ dimensional configuration space for a system with N atoms. It is, thus, limited to moderate system sizes and usually used in combination with empirical potentials.

4. Phase-field simulations

During the transition from one phase to another, an interface is formed between the two regions. While atomistic simulations have

provided many important insights into the structural evolution of the interface, it can sometimes be very challenging to simulate the complex microstructure evolution with different new phases and interfaces formed, as well as the complicated atomic diffusion at/across interfaces at relatively large length and time scales. In this case, mesoscale phase-field simulations provide a more suitable alternative.

The central idea of phase-field simulations is to employ an order parameter (phase-field variable) as a function of position and time to replace the complicated interface structure.¹²⁷ The dynamical structural evolution is determined by minimization of the total free energy of the system, which is a function of the order parameter. While the exact atomic structure of the interface is lacking, the simplified description of the microstructure allows to reach much larger simulation sizes and longer simulation times.

There are primarily two types of phase-field models, which differ in the choice of the phase-field variable. The first type of models is based on the microscopic theory formulated by Khachatryan,¹²⁸ and further developed by Chen¹²⁹ and Wang.¹³⁰ This model employs microscopic parameters such as the local composition or long-range order parameter to construct the phase-field variable. Hence, the first type of model is particularly suited for solid–solid phase transitions that involve symmetry changes and has been widely used to study, e.g., martensitic transformation,^{131,132} precipitation,^{133,134} and ferroelectric^{135,136} or magnetic¹³⁷ domain evolution.

The second type of phase-field models introduces a phenomenological variable termed also phase field to avoid explicit tracking of the interface. This approach has been widely used in simulating solidification-related processes, such as dendrite growth and eutectic solidification coupled with solute segregation.^{138,139} Based on the original idea, a number of variants of the model have been developed by different groups.^{140–142} For instance, Steinbach *et al.*^{142–144} extended the dual-phase boundary to multiphase scenarios by considering all pairs of phases. The total free-energy functional is expressed by a series of all possible pair energies and the phase evolution is simulated by minimizing the total free energy.

The phase-field method is capable of simulating complicated microstructure evolution but, as mentioned above, detailed atomistic information of the interface is lacking. There also exists an intermediate method between phase field and MD simulations, that is, phase-field crystal.^{145,146} The phase-field crystal is based on classical density functional theory, and it employs a local time-averaged numerical density field instead of a spatial average as the continuous field, which allows to capture the lattice periodicity. Hence, this method combines the advantages of atomistic simulations and traditional phase field but is numerically faster because of the coarse-graining, thus allowing to reach much longer time scales. The phase-field crystal approach has been successfully utilized in simulating different processes and phenomena, such as grain-boundary premelting,^{147–150} eutectic solidification,¹⁵¹ epitaxial growth,^{152,153} and phase separation.^{154,155}

B. Experimental techniques

1. X-ray diffraction (XRD)

X-ray diffraction (XRD) is one of the most commonly used tools in solid-state physics and chemistry, for delineating information of crystalline materials on phases, structures, textures, and different

structural parameters. It can therefore be used to detect phase transitions, as well as providing an access to defect densities and grain sizes.

XRD depends on the fact that the wavelengths of typical x rays are on the order of atomic dimensions (i.e., ~ 1 Å). XRD peaks on a detector are designed by the constructive intervention of a monochromatic beam of x rays scattered at different angles from each family of lattice planes in a specimen, being separated by a distance d_{hkl} .

If the angle of incidence is θ , then the difference in the path lengths of the two beams striking and reflecting from the two (hkl) planes must be a multiple of the wavelength λ , if diffraction is to occur, i.e.,

$$n\lambda = 2d_{hkl} \sin \theta, \quad (3)$$

which is also referred to as Bragg's law;^{156,157} it is a simpler mathematical treatment to avoid some unnecessary complexities in the more accurate Laue equations.¹⁵⁸

XRD can be performed both *ex situ* or *in situ*, for both cases we may extract useful information regarding the phase evolution during transformation. With *ex situ* XRD, one may quench the sample that undergoes phase transition to freeze the atomic structure of the phase at certain degree of transformation, and XRD allows to probe the structural information at this particular stage of transformation. While doing this at different times during the phase transition, "snapshots" of the structural phase evolution can be extracted, which allows to profile the phase transition kinetics.

In contrast, *in situ* XRD enables direct characterization of the phase transition kinetics in a real-time and on-site fashion. Since an *in situ* XRD measurement records the peak evolution with time, kinetics of the related phase transformation can be readily derived by the well-established Rietveld method.¹⁵⁹ In this case, one does not need to quench the experimental sample, which is a significant advantage, since quenching itself does not always guarantee that the atomic structure after quenching is still the same as the one at finite temperatures and at the targeted degree of transition. There is also another term that is similar to *in situ*, i.e., *operando*, which means that the experiments (e.g., XRD) are not only performed real-time and on-site, but are also directly under realistic operation conditions (or at least conditions that could mimic the actual operation ones). *Operando* experimental characterizations have been commonly used in electrochemistry.¹⁶⁰

2. Transmission electron microscopy (TEM)

In transmission electron microscopy (TEM), typically a thin sample with a thickness less than 200 nm is illuminated by parallel beams of single-energy electrons. The incident beam has enough energy for the electrons to be transmitted through the sample, either being unscattered or scattered. The emergent electron signal can then be observed by a few common techniques:¹⁶¹

- (i) Transmission electron diffraction: The scattering events in TEM are, in fact, very similar to the ones in the XRD method, hence Bragg's law applies here as well. Nevertheless, discrete spots are obtained through manipulating the magnetic lenses inside the TEM. Such diffraction patterns help to determine the crystallographic structure of a material.
- (ii) Amplitude-contrast imaging: Amplitude contrast results from variations in mass-thickness; the mass-thickness variation can produce contrast because when the electron interacts with either heavier elements or thick parts of the specimen, it

encounters more atoms (equivalently more mass). In addition, diffraction can vary locally because the crystal is not perfect. Therefore, this imaging technique yields information about the chemistry and defects in a material.

- (iii) Phase-contrast imaging: scattered electron waves exiting from the thin specimen differ in their phase. The contrast in such images is very sensitive to small changes in the thickness, orientation, or scattering factor of the specimen, as well as variations in the focus or astigmatism of the objective lens. This sensitivity is the basic principle to form images of microstructure at the atomic scale, i.e., high-resolution TEM (HRTEM) imaging. HRTEM images provide information about the microstructure and defects at an atomic resolution.

With scanning TEM (STEM), the electron beams are highly focused to form a probe to raster-scan across the material. Various types of scattering are then collected from different geometric positions with respect to the specimen. The transmitted electrons at high scattering angles can be collected to form high-resolution, chemically sensitive, atomic-number contrast images. The x rays generated can be collected using an energy-dispersive x-ray spectroscopy (EDS) detector and used to form high-spatial-resolution compositional maps. Electron energy losses can be detected using an energy image filter to map the compositional and electronic properties of materials.

Observations of dynamical processes, like in the XRD measurements, can also be performed in TEM or STEM. Moreover, *in situ* TEM or STEM bear the benefit that the involved evolution of the crystal structure and defects during a phase transformation can be directly visualized in real time.

3. Video microscopy

Direct observations of the nucleation process of the solid-state (diffusional or diffusionless) phase transitions down to single-atom scale are hard to achieve in the practical materials. In order to address this challenge, nucleation processes of the solid-state transitions in colloidal crystals, a model thermodynamic system composed of micrometer-sized colloidal particles, can be directly visualized with single-particle resolution using video microscopy.¹⁶²

Video microscopy has already provided many general insights into phase transitions, including the dynamics of crystallization/melting and glass formation.^{163–166} Few studies, however, have probed solid-state phase transitions, especially rare on its kinetics.^{167–169} The recent advances of the high-quality large crystalline domains and of the local heating technique^{170,171} made it possible to employ video microscopy to study nearly homogeneous and heterogeneous nucleation at a desired type of defect during the diffusive and martensitic transitions between square (\square) and triangular (\triangle) lattices.

In such video-microscopy studies, temperature-sensitive poly(N-isopropylacrylamide) (NIPA) microgel colloidal spheres are employed to make the volume fraction tunable, as their effective diameters change linearly with temperature. The NIPA spheres are little charged with short-range steric repulsions and exhibit almost the same phase behavior as hard spheres. They may form fcc crystals in three dimensions or triangular lattices in two dimensions. To obtain the multiple crystalline phases needed for probing solid-state transitions, the colloidal spheres are confined between two glass walls. Such samples are well known to

exhibit a cascade of crystalline phases while increasing the wall separation: 1 Δ , 2 \square , 2 Δ , 3 \square , and 3 Δ , etc.^{172,173} Here, 1 Δ denotes a monolayer triangular lattice; 2 \square refers to a two-layer square lattice.

The equilibrium state of these samples is controlled by two thermodynamic variables: the ratio of wall separation to particle diameter and the particle volume fraction. If temperature is varied quasi-statically, then such systems evolve along an angled trajectory in the phase diagram. To study the phase transition kinetics, temperature is varied suddenly to produce a superheated metastable \square -lattice, and then one can monitor its evolution toward the equilibrium Δ -lattice at a constant temperature. To prevent invasion from preexisting Δ -domains, a local heating technique is developed whereby a beam of light passing through the microscope objective lens locally heats the interior of a \square -crystalline domain. The particle motions are recorded with a charged-coupled device camera at 10 frames s^{-1} . Particle positions are tracked using standard image analysis. The Lindemann parameter¹⁷⁴ based on the local coordinates of neighboring particles is used to characterize the system because the volume fraction is ambiguous for soft spheres.

4. Differential scanning calorimetry (DSC)

Many studies of phase transitions involve measurements of properties as a function of temperature, which oftentimes employ the differential scanning calorimetry (DSC). DSC is a thermoanalytical technique for measuring the energy necessary to establish a nearly zero temperature difference between a sample and an inert reference, as the sample and reference are maintained at nearly the same temperature in an environment heated or cooled at a controlled rate.

DSC measures the temperature and heat flows associated with transitions in materials as a function of time and temperature. Such measurements provide qualitative and quantitative information of phase transitions, including thermodynamic variables like transition temperatures and latent heat, and kinetic factors such as degree of transition (f), effective activation energy, and the growth exponent. The transition temperature and latent heat can be determined directly from the DSC curves by tangential and peak area integration methods, respectively.

The degree of phase transition f can be obtained from the DSC signal, recorded upon isochronal annealing as a function of temperature as follows.⁶⁴ Before phase transition, heat is absorbed upon heating in accordance with the heat capacity of the initial phase. During the phase transition extra latent heat is taken up or released. After completing the phase transition, heat is absorbed upon further heating in accordance with the heat capacity of the final phase. By extrapolating the heat capacities of the untransformed and fully transformed specimens to the temperature range where the transition occurs, it is possible to determine the degree of transition.

The extrapolation of the measured heat absorption rates can be made from either side of the DSC peak associated with the phase transition. After subtracting the baseline from the recorded signal, one obtains the released/absorbed heat rate due to the transition alone. The determination of f as a function of temperature or time is then straightforward, where the effective activation energy and the growth exponent can be obtained by fitting to the classical Avrami equation of phase transition kinetics,^{175–177}

$$f(t) = 1 - \exp(-kt)^n, \quad (4)$$

where t is time, k is a temperature-dependent rate constant, and n is the growth exponent that depends on the geometry of the transformation. The kinetic rate constant k can be further related to the activation energy (E_a) by

$$\ln k = -\frac{E_a}{RT} + \ln k_0, \quad (5)$$

where R is the ideal gas constant, T is absolute temperature, and k_0 is a material-specific constant.

IV. PROGRESS IN DEFECT-CHARACTERIZED PHASE TRANSITION KINETICS

In this section, we use representative examples to illustrate the recent progress in understanding defect-characterized phase transition kinetics. We cover different types of defects including point defects, dislocations, grain boundaries, stacking faults, surfaces, and interfaces, and discuss how their presence may influence the phase transition kinetics.

A. Point defects

During a martensitic transformation, the host lattice transitions from one type of crystal structure to another in a diffusionless manner, which has been investigated thoroughly by both theory and experiment. However, attention has been seldom paid to the behavior of point defects during the martensitic transformation. As we will show in the following with selected examples, point defects may play a critical role in the phase transition kinetics, which ultimately impacts the product phase and its properties.

1. Interstitials

A prototypical example is the fcc \rightarrow body-centered tetragonal (bct) martensitic phase transition in the Fe–C system, which is critical to improving the strength of steels. Figure 9(a) shows the lattice correspondence between austenite (fcc) and martensite (bct). Carbon atoms are incorporated as interstitials in both austenite and martensite. There is only one type of octahedral interstitial sites for C to occupy in fcc austenite, but there are three octahedral interstitial sublattices available for C in bct martensite associated with three principal directions for tetragonal distortion. During the fcc \rightarrow bct transition of the Fe host lattice, the C atoms in fcc austenite need to be redistributed into three octahedral interstitial sublattices. With conventional transformation paths such as the Bain path¹⁷⁹ and Kurdjumov–Sachs (KS)¹⁸⁰ or Nishiyama–Wassermann (NW)¹¹³ path, the octahedral interstitial sites in austenite naturally correspond to one particular octahedral interstitial sublattice in martensite [see Fig. 9(a)]. In this case, the Fe–C martensite undergoes a tetragonal distortion with the c/a ratio linearly dependent on the C concentration. This was indeed confirmed by various experimental data for tempered Fe–C martensite¹⁸¹ as shown by the squares and black dashed line in Fig. 9(b).

However, in the freshly formed martensite, it was found that the c/a ratio is substantially lower than the expected values [see blue circles and line Fig. 9(b)]; detailed neutron diffraction analyses revealed that only 80% of the C atoms are sitting on the same octahedral interstitial sublattice,¹⁸² which could not be explained by the conventional transformation mechanisms. To address this discrepancy, Zhang *et al.*¹⁷⁸ proposed a new two-step transformation path: austenite first

transitions to a metastable intermediate structure (MIS), and then MIS transforms to martensite. For this new transformation path, the octahedral interstitial sites no longer always correspond to a single octahedral sublattice in martensite [see Fig. 9(a)]. Instead, there are three scenarios for the redistribution of C atoms: S1, S2, and S3.

Using SSNEB calculations, Zhang *et al.*¹⁷⁸ investigated the MEPs for the three scenarios. For the austenite \rightarrow MIS transition, the interstitial C atom at the octahedral site in austenite only displaces slightly, following the rearrangement of the Fe lattice. This is also the case for the first two scenarios (S1 and S2) during the MIS to martensite transition [Figs. 9(c) and 9(d)], leading to C redistribution into a particular octahedral interstitial sublattice in martensite. However, in scenario S3 it is almost equally favorable for C to be redistributed into the three octahedral interstitial sublattices. Hence, there should only be a fraction of C that gets redistributed into the major octahedral interstitial sublattice. As the three scenarios occur with equal probabilities, the resulting fraction of C in the major sublattice is $1/3 + 1/3 + 1/3 \times 1/3 = 7/9 \approx 78\%$, which nicely agrees with the experimentally observed result ($\approx 80\%$).

This example demonstrates that interstitial point defects might not simply follow the transformation of the host lattice, but they can also undergo short-range displacements to neighboring interstitial sites. If the interplay between the displacive lattice transformation and the local interstitial redistribution is ignored in simulations and interpretation of experimental results, the atomic structure of the product phase of the transformation can be incorrect and the transformation mechanisms can be wrong.

2. Vacancies

Vacancies are another common type of point defects in materials. However, vacancies may play quite different roles than other point defects. Here, we use examples in metallic alloys and oxide cathode materials to demonstrate the impacts of vacancies on phase transition kinetics.

The first important function that vacancies may have in phase transition kinetics is reducing nucleation barriers and the critical size of the nucleus by introducing new transformation pathways. For instance, using an Al-1.7at.%Cu alloy, Bourgeois *et al.*¹⁸³ revealed a template-directed nucleation (TDN) pathway and the important contribution of vacancies for the formation of the θ' phase. A precursor phase (θ'') with excess vacancies serves as a structural template for the phase (θ') to nucleate, which reduces both the nucleation barrier and the critical size of a θ' nucleus.

It is well established experimentally that for bulk Al-1.7at.%Cu alloy with a conventional heat treatment below $\sim 220^\circ\text{C}$, the θ'' phase [Fig. 10(a)] would form before θ' [Fig. 10(b)]. This is due to the much lower nucleation barrier of θ'' compared to θ' , as it only requires Cu diffusion and direct replacement of Al atoms by Cu solutes. Therefore, the probability that θ' nucleates from the supersaturated solid solution (SSS) before θ'' is very low. The difficult nucleation of θ' is reflected in a low precipitate density [see Fig. 10(c)]. However, Bourgeois *et al.*¹⁸³ found that the same transformations are considerably faster in an *in situ* heated nanometer-thick specimen. Of particular interest here is that the nuclei seem to form exclusively at the cut surface of θ'' precipitates, but not in precipitates that are fully embedded in the Al matrix [Fig. 10(d)]. Based on experimental observations that the high

nucleation rate is linked with the proximity to the specimen surface and systematic atomistic simulations, vacancies were identified as the key and sole factor for such accelerated kinetics of $\theta'' \rightarrow \theta'$ transformation.

The atomic-scale mechanisms of the $\theta'' \rightarrow \theta'$ transformation promoted by vacancies are schematically illustrated in Figs. 10(e) and 10(f). First, a small number of vacancies are generated through well-thought heat treatment procedures or by high-energy electron beam irradiation in θ'' [see pink circles in Figs. 10(e) and 10(f)]. These vacancies kinetically facilitate the stacking change from θ'' to θ' by lowering the barrier for shuffling Cu atoms, thus enabling high nucleation rates of the θ' phase. Second, additional vacancies [green circles in Figs. 10(e) and 10(f)] surrounding the nucleus help to relieve the compressive volumetric misfit strain as well as to lower the semicoherent interfacial energy through its structural component, which thus lower the barrier to nucleation.

In addition, the driving force associated with the removal of excess vacancies from the Al matrix to the nucleus was evaluated via an established theoretical framework,^{184,185} as shown in Figs. 10(g) and 10(h). On the one hand, the classical nucleation theory for the SSS nucleation shows a much larger critical radius R^* and a much higher nucleation barrier ΔG^* [Fig. 10(g)] compared to TDN without considering the effect of vacancies [solid curves in Fig. 10(h)]. On the other hand, the calculated energy changes as a function of precipitate radius for TDN and vacancy-relieved strain [dashed curves in Fig. 10(h)] show that both ΔG^* and R^* decrease significantly in the case of vacancy supersaturation (VSS—excess vacancies compared to the equilibrium concentration) for the two thinnest nuclei. A reasonably small value for $\ln(\text{VSS})$ of ~ 5 (i.e., $\text{VSS} \approx 150$) can already reduce R^* from 2.3 to ~ 1.3 nm, which is close to the experimentally observed value.

In addition to assisting nucleation, vacancies can also play other roles in phase transition kinetics. For instance, in electrode materials of rechargeable metal-ion batteries and pseudocapacitors, vacancies can help to block unfavorable phase formation and assist ion migration during discharging,³³ which can be utilized to improve the energy storage performance of electrode materials.

Shimokawa *et al.*¹⁸⁶ utilized cation vacancies in a spinel-type cathode material of rechargeable magnesium batteries to improve the cycling stability of the cathode material. In stoichiometric spinel oxide of ZnMn_2O_4 , Mg^{2+} ions are inserted into the octahedral 16c vacant sites during discharging and electrostatically repulse Zn^{2+} ions at the tetrahedral 8a sites, leading to migration of Zn^{2+} ions from tetrahedral 8a to adjacent 16c sites [Fig. 11(a)]. This migration results in the formation of rock salt clusters, which block the migration path of Mg^{2+} in the ZnMn_2O_4 cathode and are thus responsible for the poor cycling stability of ZnMn_2O_4 cathode.

In contrast, when cation vacancies are incorporated at the 16d sites of the spinel structure, a defect-spinel-type cathode material of ZnMnO_3 is obtained. In this case, the inserted Mg^{2+} ions can hop from 16c vacant sites to 16d deficiency sites and the strong electrostatic repulsion thus disappears between Mg^{2+} and Zn^{2+} ions, which prevents the unfavorable phase transition of the cathode material from spinel to rock salt [Fig. 11(b)]. The defect spinel is thermodynamically more stable than the rock salt structure, and its structure is thus well maintained during discharging due to the existence of cation vacancies [Figs. 11(c) and 11(d)]. At the same time, the Mg migration path is

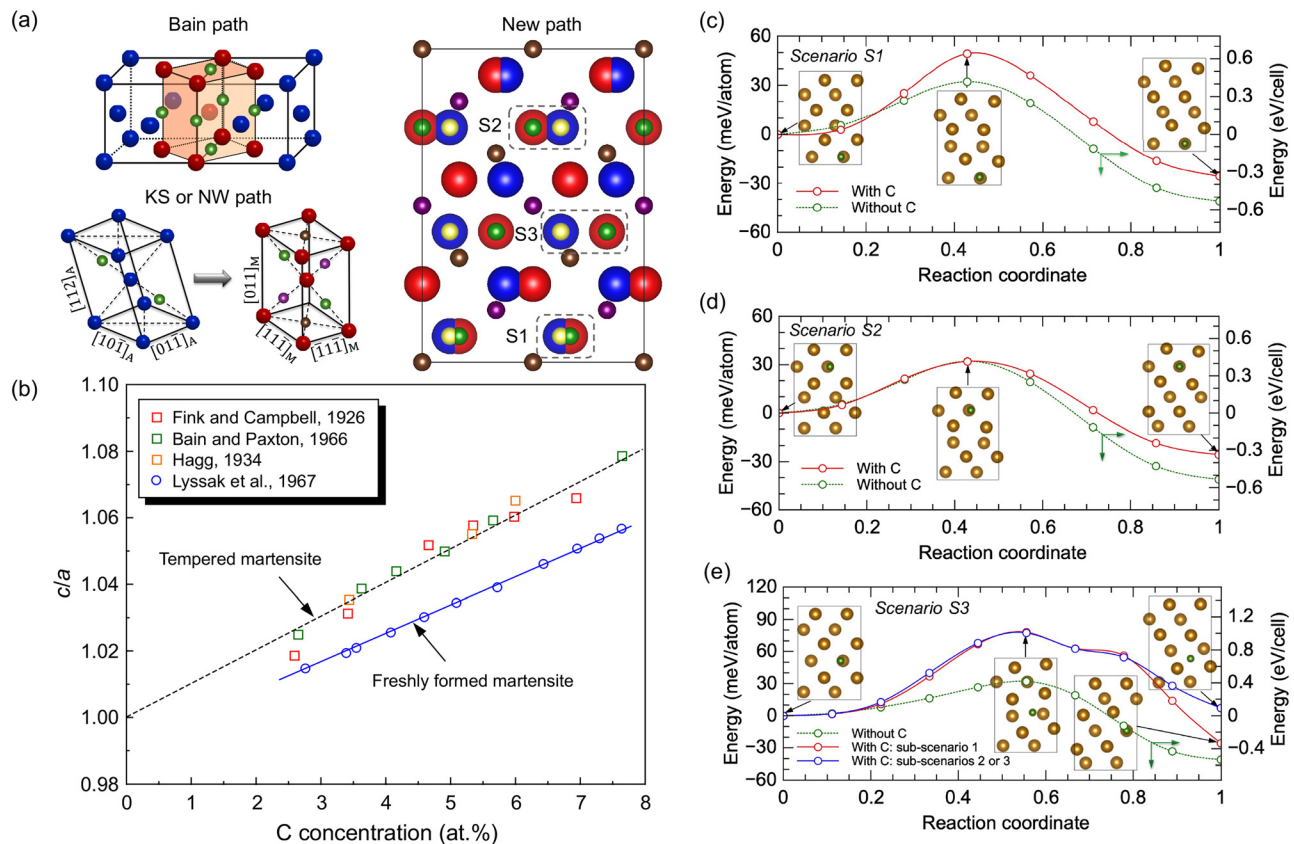


FIG. 9. (a) Lattice correspondence between austenite and martensite and the corresponding octahedral interstitial sites. Three phase transition paths are shown: Bain path, Kurdjumov–Sachs (KS) or Nishiyama–Wassermann (NW) path, and a new path proposed in Ref. 178. The large blue (red) spheres represent Fe atoms in austenite (martensite). The small yellow spheres denote all octahedral interstitial sites for C in austenite. The other small colored spheres correspond to the octahedral interstitial sites for C in martensite; there are three octahedral sublattices: green is sublattice 1; brown is sublattice 2; purple is sublattice 3. S1–S3 correspond to three scenarios for C redistribution within the octahedral sublattices in martensite. (b) Experimentally measured c/a ratios of freshly formed martensite and tempered martensite for different C concentrations, where c and a are the two lattice parameters of martensite. (c)–(e) Minimum-energy path and structural evolution of the metastable intermediate structure (MIS) → martensite transition in three scenarios: (c) S1, (d) S2, and (e) S3. Reproduced with permission from Zhang *et al.*, *Phys. Rev. B* **94**, 104109 (2016). Copyright 2016 American Physical Society.¹⁷⁸

also secured. Both advantages lead to the significantly improved cycling stability of defect-spinel ZnMnO_3 cathode.

3. Substitutional defects

Alloying is commonly employed to engineer the materials performance. The alloying elements may substitute on the lattice sites, forming substitutional defects (Fig. 2). It has been demonstrated that these substitutional defects can also promote the nucleation of martensite¹⁸⁷ through the local stress fields induced by the defects. More interestingly, their presence is actually central to the strain-glass transition.

Strain-glass transition is a thermodynamically driven but kinetically controlled process. Theorists have made many attempts to unveil the nature of strain-glass states^{189,190} and considerable interesting insights have been borrowed from a similar type of materials—spin glasses. It was suggested that a strain-glass state is induced by concentration fluctuations of random point defects, which result in spatial fluctuations in the local transition temperature (M_s). At very high

defect concentrations, the martensite nuclei persist upon cooling without transforming into martensite, but freeze into a strain-glass state. Since point defects induce an isotropic or non-symmetry-breaking effect, their impact on the global anisotropy of the host lattice seems limited. However, a nearly isotropic host lattice is key to enable the strain-glass formation. Hence, the local transition temperature fluctuation caused by point defects alone did not seem to be able to explain the phase diagram of the strain states.

Wang *et al.*¹⁸⁸ proposed an alternative model assuming two roles played by the substitutional defects: (i) they change the stability of martensite globally rather than locally, and (ii) they produce local lattice distortions that interact with the local strain order parameters of ferroelastic or martensitic transition and break the symmetry of the Landau potential [Figs. 12(a)–12(d)]. The global temperature fluctuations affect the thermodynamic free-energy landscape and, thus, the transition pathways and martensitic transition temperatures. The local field effect impacts the transition kinetics and leads to preferential nucleation and confined growth of martensite.

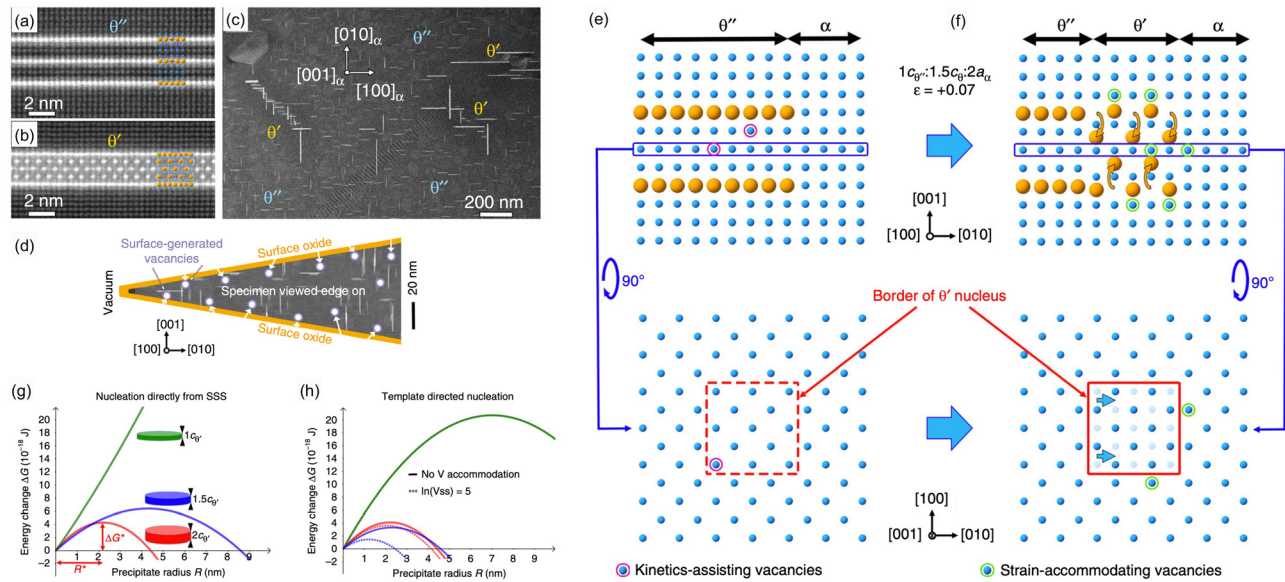


FIG. 10. (a) θ'' and (b) θ' precipitates in a conventionally heat-treated Al-1.7at.%Cu alloy. (c) Microstructure of the alloy, showing heterogeneous regions of θ'' and θ' precipitates. (d) A TEM image of the specimen. (e) and (f) Schematic illustration of the atomic mechanisms for the $\theta'' \rightarrow \theta'$ transformation assisted by vacancies. (g) and (h) Computed nucleation energy barrier for the θ' phase based on the classical nucleation theory for (g) the supersaturated solid solution (SSS) nucleation and (h) template directed nucleation (TDN) processes. Reproduced with permission from Bourgeois *et al.*, Nat. Commun. 11, 1248 (2020). Copyright 2020 Authors, licensed under a Creative Commons Attribution (CC BY) License.¹⁸³

As shown in Fig. 12(e), through phase-field simulations of a single crystal undergoing a generic improper square to rectangle martensitic transition, Wang *et al.*¹⁸⁸ showed that the model not only reproduces the crossover from martensite to strain glass at a critical concentration, but also captures all the important features of the experimental phase diagram. While the global transition temperature fluctuations stabilize the parent phase, the local field effect promotes the formation or freezing of local strain ordering (i.e., nanodomain martensite), but prevents the formation of long-range ordered martensite.

4. Impurities

In addition to intentional alloying elements, there could also be unintentional impurities. Impurities can be incorporated in the lattice at interstitial or substitutional sites (Fig. 2), which may significantly impact the phase transition kinetics as well.

An interesting example relates to the role of impurities in the $\alpha \rightarrow \omega$ martensitic transformation in Ti. For pure Ti, its ductile α phase transitions to brittle ω phase at a critical pressure of 9 GPa,¹⁹¹ which leads to serious technological issues. It has been empirically established that the presence of impurities in commercial Ti alloys such as A-70 and Ti-6Al-4V (wt. %) can enhance the critical pressure associated with the $\alpha \rightarrow \omega$ transition up to 35 GPa,^{192,193} which significantly improves the technological utility of Ti alloys in aerospace applications. However, the fundamental mechanisms were not directly accessible from experiments. Hennig *et al.*¹⁹⁴ studied the impacts of different impurities on the $\alpha \rightarrow \omega$ martensitic transformation pathways and energy barriers in Ti.

For interstitial impurities, there exist octahedral, tetrahedral, and hexahedral sites in both α and ω Ti. However, for the interstitial

impurities studied (O, C, and N) by Hennig *et al.*¹⁹⁴ the impurities are unstable at the tetrahedral site in α Ti, and relax to the near hexahedral site in the basal plane.

Thermodynamic calculations showed that for all the three types of interstitial impurities, it is energetically more favorable to occupy the octahedral sites in both α - and ω -Ti. Nevertheless, from a kinetic perspective, there is a redistribution effect of the octahedral interstitials in α -Ti into different interstitials in ω -Ti, similar to the case of C interstitials in Fe discussed in Sec. IV A 1. This is because the hexagonal symmetry is broken during the $\alpha \rightarrow \omega$ phase transition. As a result, only one-third of the octahedral sites in α -Ti are transformed to the octahedral sites in ω -Ti; the other two-thirds are, in fact, transformed to the hexagonal sites in ω -Ti.

Based on the MEPs from NEB calculations (see Sec. III A 2), all three types of interstitial impurities substantially enhance the phase transformation barrier as compared to pure Ti, which nicely explains why impurities could suppress or even block the $\alpha \rightarrow \omega$ phase transition in Ti alloys.

In a similar way, Hennig *et al.*¹⁹⁴ also investigated the impact of substitutional impurities (Al and V) considering two possible substitutional sites. The two possible substitutional sites also share one third and two thirds in probability based on crystallographic symmetry analysis, respectively. Similar to the behavior of interstitials, Al increases the transformation barrier, irrespective of the final substitutional site in ω -Ti. In contrast, the presence of V actually slightly decreases the energy barrier. This qualitative difference was explained in terms of d -electron concentration:¹⁹⁶ transition metals with more d electrons such as V, Mo, Fe, and Ta stabilize the ω phase, while early transition metals and simple metals such as Al tend to favor the α phase.

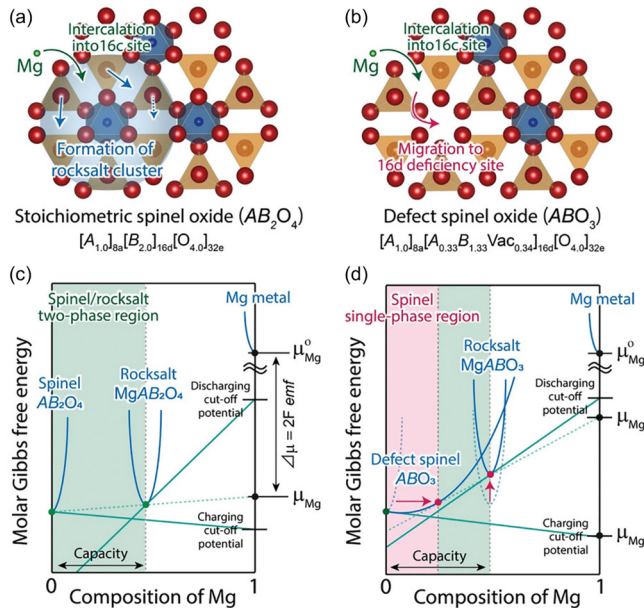


FIG. 11. (a) and (b) Mg insertion pathways proposed for stoichiometric spinel and defect spinel oxides. (c) and (d) Chemical potential diagrams of each pristine spinel and corresponding rock salt produced after phase transition during Mg insertion. Reproduced with permission from Shimokawa *et al.*, *Adv. Mater.* **33**, 2007539 (2021). Copyright 2021 Authors, licensed under a Creative Commons Attribution (CC BY-NC-ND) License.¹⁸⁶

Overall, impurities have a propensity to suppress the $\alpha \rightarrow \omega$ phase transitions in Ti, which provides a rationale for the shift of the critical pressure toward higher values in commercial Ti alloys. This example again demonstrates the important impact of point defects on martensitic phase transitions, in particular, with regard to the kinetic pathways and barriers. The suppression of the $\alpha \rightarrow \omega$ phase transition by point defects enhances the stability of the ductile α phase and widens the pressure window of application for commercial Ti alloys.

B. Dislocations

As a typical extended defect, dislocations are much more complex than point defects. Concerning phase transition kinetics, similar to the case of vacancies, dislocations can also help to promote nucleation through a two-step process with substantially reduced nucleation barriers.¹⁷⁰ Here, we highlight two additional functions that dislocations may have in phase transition kinetics: (i) acting as traps for alloying elements, and (ii) triggering the formation of strain-glass states.

1. Dislocation traps

Alloying elements are usually intentionally added to materials in order to stabilize certain phases or promote the formation of new phases, which in turn improve the mechanical or electronic performances of materials. As discussed in Sec. IV A 1, in one of the most studied materials Fe, C is added in order to trigger the formation of bct Fe-C martensite, which is critical to achieving high strength. In Sec. IV A 1, we illustrated the role of alloyed C atoms as interstitial point

defects, and their impact on the martensitic phase transformation of the Fe lattice. However, in addition to occupying the octahedral interstitial sites in the bct Fe lattice, C atoms can also segregate to extended defects such as dislocations and grain boundaries [see Fig. 13(a)]. Consequently, the presence of dislocations in the material may indirectly influence the martensitic phase transition.

From the perspective of C atoms, when they are alloyed into the material they will distribute into the energetically most favorable sites. In the current case, there are two options for C: (i) octahedral interstitial sites in the Fe lattice, and (ii) trapping sites at extended defects. For option (i), there exists an additional degree of freedom that C atoms can either randomly occupy three octahedral sublattices or selectively occupy only one octahedral sublattice, which corresponds disordered (body-centered cubic, bcc) and ordered (bct) martensite; this ordering is commonly referred to as Zener ordering.¹⁹⁸

For C to decide whether they prefer option (i) or (ii), the key is the chemical potential of C in these two places. Zhang *et al.*¹⁹⁵ developed a self-consistent approach that allows to quantitatively compute the chemical potential of C in both ordered and disordered Fe-C martensite as a function of C concentration, which can be further compared with the chemical potential of C inside dislocations or grain boundaries. As shown in Fig. 13(b), at dilute C concentrations, it is energetically more favorable to form disordered martensite as compared to the ordered one; the chemical potential of C gradually increases with increasing C concentration. Above 0.8 at. % of C, the ordered martensite is preferred and the chemical potential of C decreases dramatically with the increasing C concentration. However, below 2.6 at. % of C, it is energetically most favorable for C to simply segregate to extended defects such as dislocations; only above 2.6 at. %, ordered martensite becomes the favorable place for C. Notably, when the C concentration exceeds the critical concentration of 2.6 at. %, C atoms will not segregate to extended defects. Considering a grand canonical scenario, where the C concentration is varied from low to high, C atoms will first segregate to extended defects and then diffuse back to the Fe lattice, forming ordered martensite.

With the above understanding, the experimentally observed dependence of the c/a ratio of Fe-C alloys on the C concentration can be well understood and interpreted [see Fig. 13(c)]. There has actually been an active debate^{181,199–201} on the occupation behavior of C at low concentrations: segregation to dislocations vs martensite formation. This discussion can, thus, be clarified and unified.

This example demonstrates the importance of extended defects in trapping alloying elements and, in turn, their effect on martensitic phase transition kinetics in the host lattice. With the presence of extended defects, the alloying elements may not be able to realize their desired functionalities in phase transitions.

2. Strain-glass formation

As discussed above, point defects can effectively suppress martensitic transitions and trap the system in a frozen strain-glass state. Similar behavior has been identified for precipitates as well.^{202,203} Recently, Zhang *et al.*¹⁹⁷ demonstrated that dislocations could also lead to a crossover from martensite to strain glass by introducing random stress fields in a compressed Ti₅₀Ni₄₅Fe₅ shape-memory alloy.

The phase diagram of the Ti₅₀Ni₄₅Fe₅ ferroelastic system with respect to dislocation density was constructed and presented in

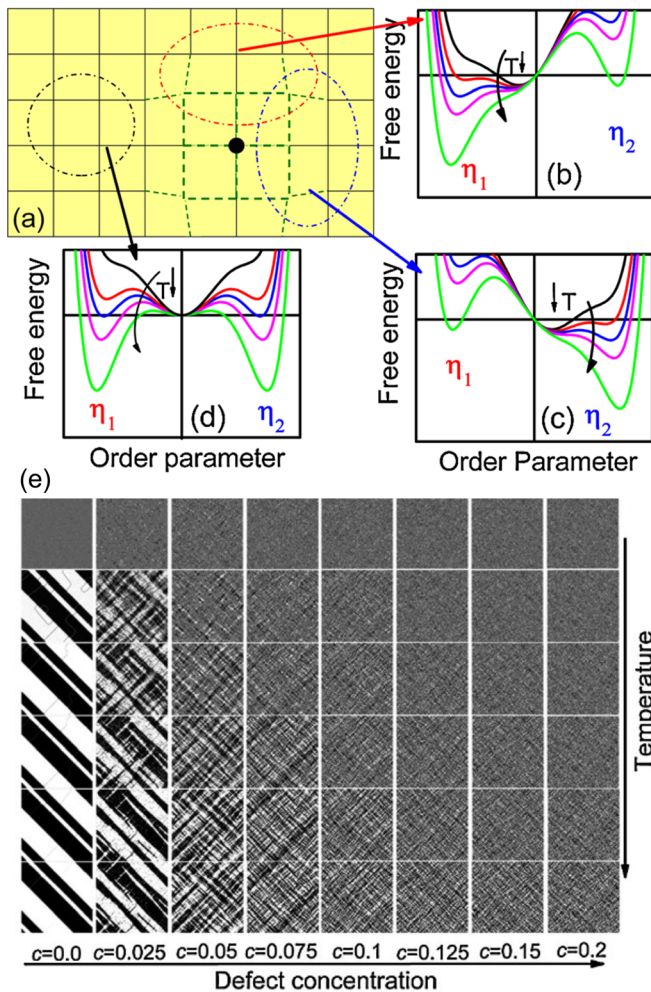


FIG. 12. (a) Local lattice distortions caused by a substitutional point defect (black dots). (b)–(d) Landau potential corresponding to three different locations. The curved arrows indicate the change of local Landau potential with lowering temperature. (e) Strain states as functions of defect concentration and temperature from phase-field simulations. Reproduced with permission from Wang *et al.*, Phys. Rev. Lett. **105**, 205702 (2010). Copyright 2010 American Physical Society.¹⁸⁸

Fig. 14(a). It was found that a huge dislocation density ($\rho_c = 564 \mu\text{m}^{-2}$) is required to fully suppress the formation of R-martensite and to enable the strain-glass transition, even though the current $\text{Ti}_{50}\text{Ni}_{45}\text{Fe}_5$ matrix already contains a considerable amount of point defects (5 at. % Fe). Careful analyses suggested that dislocations promote the strain-glass transition via a kinetic mechanism by limiting the scale of R-like nanodomain growth as depicted in **Fig. 14(b)**. It is consistent with the fact that dislocations do not change the chemical composition of the matrix and consequently do not affect the transition temperature much.

A unified transition kinetics was proposed for both R-martensite and strain-glass transitions, which were divided into three stages. Stage 1 ($T = T_{\text{nd}}$): nucleation of quasidynamic R-like nanodomains. Stage 2 [R_s (or T_0) $< T < T_{\text{nd}}$]: initial growth of R-like nanodomains within the size of 50 nm. Stage 3 ($T \leq R_s$): the formation of R-martensite

with domain size over 50 nm. Under such a scheme, the strain-glass transition can be treated as an “incomplete R-martensite transition” only involving the first two stages; after the nucleation of R-like nanodomains below T_{nd} , the system is frozen into the strain-glass state with the nanodomain size < 50 nm at T_0 .

C. Grain boundaries

Similar to dislocations, grain boundaries can also assist the nucleation process.¹⁷⁰ We did not explore this type of mechanism in detail for dislocations, but here we use an example of grain boundaries in colloidal crystals to illustrate how planar defects can promote nucleation. Colloidal crystals have been used extensively as model systems since the particle sizes are large enough to allow an intuitive observation of phase transition kinetics using video microscopy. Furthermore, various interactions between particles can be mimicked by tuning the properties of the colloidal particles. The physics and mechanisms extracted from these model systems can oftentimes be transferred or extended to more complicated materials as well. In addition to this function of grain boundaries, we will also introduce the concept of grain-boundary phases and grain-boundary phase transitions, which highlight the atomic structure of grain boundaries and their kinetic evolution upon internal insertion of point defects or external temperature variations. We will also discuss a special type of phase transition at grain boundaries—grain-boundary premelting.

1. Assisting nucleation kinetics

Figures 15(a)–15(d) show the experimental observation of the nucleation kinetics of a triangular (Δ) phase from the square (\square) phase in the vicinity of a grain boundary in a colloidal crystal. Peng *et al.*¹⁷¹ found that nucleation of the Δ -phase occurs more often at the grain boundary, which was explained by a lowering of the nucleation barrier, resulting from the fact that grain boundaries usually act as a sink for small defects. We mentioned that a two-step nucleation mechanism via an intermediate liquid phase can effectively lower the nucleation barrier. However, Peng *et al.*¹⁷¹ noticed that the formation of an intermediate liquid phase is not always necessary.

For the colloidal crystal, one can control the flow velocity (v). They found that when $v \leq 10 \text{ nm s}^{-1}$, the nucleation at the grain boundary follows the above two-step diffusive process. When $v > 10 \text{ nm s}^{-1}$, the $\square \rightarrow \Delta$ phase transition does not involve an intermediate step.

When the nucleus grows larger, it develops both coherent [I and II in **Fig. 15(d)**] and incoherent [III and IV in **Fig. 15(d)**] facets with the original \square -lattice. The coherent facets are energetically favorable and the system tends to maintain their flat shape [see the ledges in **Fig. 15(d)**] and let them grow. Grain boundaries have different mismatch angles and inclination angles, which can promote the formation of incoherent facets. Incoherent facets are rough and have many sites to attach particles, which in turn allow continuous transformation of the \square -lattice into the Δ -lattice.

Peng *et al.*¹⁷¹ further investigated a special situation for grain boundaries, where a symmetric triple junction is formed [see **Figs. 15(e)–15(h)**]. A key finding was that even in the case of a small flow velocity ($v = 2 \text{ nm s}^{-1}$), the formation of an intermediate liquid phase is not necessary if the nucleation occurs at a symmetric triple junction of grain boundaries. This was because when the Δ -nucleus is formed

inside the symmetric triple junction, the facets can all be coherent with very low interfacial energies. In this case, the nucleus could continuously grow without much energy penalty and, thus, does not need to involve an intermediate liquid phase.

2. Grain-boundary transformation

The above example focused on the role of grain boundaries as an extended defect that influences the bulk phase transformation kinetics. However, grain boundaries themselves can have various ordered structures, and structural transformations may occur between these different ordered structures. As a conceptual advance, ordered grain boundaries may be considered as special grain-boundary phases.^{204,205} Experimentally, it is very challenging to directly observe grain-boundary phase transitions. Even theoretically, this is far from trivial, since commonly used MD simulations employ periodic supercells, which do not allow varying the atomic density in the core region of the grain boundary. However, realistic experimental conditions do not have such constraints. Consequently, the unphysical constraints in MD simulations tend to stabilize one particular grain-boundary structure and structural transitions between different grain-boundary phases are usually suppressed.

Frolov *et al.*²⁰⁶ tackled this challenge with an improved MD scheme, which facilitates grain-boundary density variations and allows the grain boundary to adopt the thermodynamically most favorable configuration. They first developed an algorithm to identify the possible grain-boundary structures at $T=0$ K while varying the atomic density at the grain boundary. Figure 16(a) shows the result for a $\Sigma 5(310)$ grain boundary in fcc Cu. There are two (local) minima in the plot of excess grain-boundary energy as a function of atomic density, which correspond to two stable grain-boundary phases. As depicted in Figs. 16(b) and 16(c), the minimum at 0 density refers to a normal-kites configuration [Fig. 16(b)], and the one at 0.4 (2/5 of the (310) plane) has a split-kites structure [Fig. 16(c)].

Using standard MD simulations with periodic supercells, one can observe the two types of grain-boundary phases at different temperatures. However, within this approach, one cannot see the direct transition from one grain-boundary phase to the other. Frolov *et al.*²⁰⁶ introduced a new simulation scheme, in which the grain boundary terminates at an open surface; the surface can act as a source or sink of atoms, allowing the grain boundary to adjust its density. Employing this improved scheme, it was then possible to observe the coexistence of the two grain-boundary phases at the same temperature and reversible transitions between them while

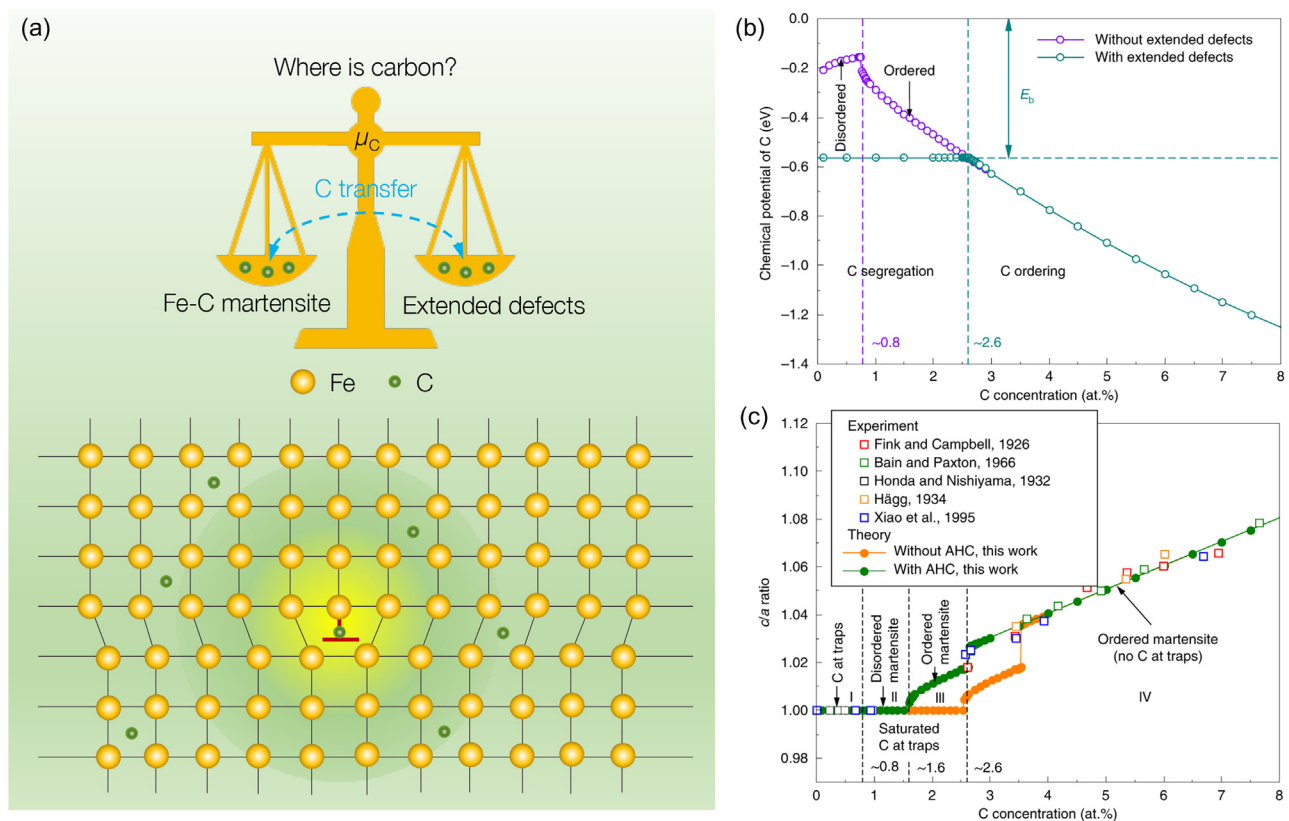


FIG. 13. (a) Schematic illustration of the competition between Fe–C martensite formation and C segregation to extended defects such as dislocations. (b) Chemical potential of C (μ_C) at room temperature as a function of C concentration. (c) Comparison between experimental and theoretically computed c/a ratio of Fe–C alloys as a function of C concentration at room temperature. Reproduced with permission from Zhang *et al.*, Nat. Mater. **19**, 849 (2020). Copyright 2020 Springer Nature.¹⁹⁵

changing the temperature. They demonstrated this behavior not only for different phases at the $\Sigma 5(310)$ grain boundary, but also at the $\Sigma 5(210)$ grain boundary, for which there are normal-kites, split-kites, and filled-kites phases.

Furthermore, they also examined the impact of point defects on the grain-boundary phase transitions using periodic supercells (in order to exclude all sources/sinks of atoms). As shown in Figs. 16(d)–16(f), the kites structure transitions to the split-kites configuration after interstitial defects are intentionally inserted into the vicinity of the $\Sigma 5(310)$ grain boundary. Upon annealing at 800 K, the interstitials diffuse into the core region of the grain boundary and lead to a disordered state. When the annealing proceeds, the grain boundary gradually evolves into the split-kites phase. Similarly, while further inserting vacancies into the grain boundary with the split-kites structure, the grain boundary transforms back to the initial kites phase after a small period of disordering in between. This demonstrated the reversibility of the grain-boundary phase transitions induced by point defects.

Recently, employing advanced HRSTEM Meiners *et al.*²⁰⁹ directly observed the coexistence of pearl and domino phases at $\Sigma 19b$ grain boundaries in Cu, which agreed remarkably well with the results from evolutionary search for grain-boundary structures using the USPEX code²¹⁰ and clustering analysis. This serves as strong direct experimental evidence for the existence of grain-boundary phases and structural transitions between them.

3. Grain-boundary premelting

In general, it has been speculated during the last decades that grain and phase boundaries can be analyzed using local equilibrium thermodynamics and may have their own phase diagrams in a manner analogous to bulk phases. Confined states at interfaces have been investigated, especially in grain boundaries, by HRSTEM as an attempt to explain phenomena like abnormal grain growth (especially, in

alumina), grain-boundary premelting, (liquid metal) grain-boundary embrittlement (noteworthy, Al-Ga, Ni-Bi, SiC, and Si_3N_4) and activated sintering^{204,211–213} that cannot be successfully described by purely mechanistic explanations.

The premelting at grain boundaries, and also at other defects, such as stacking faults and dislocations, has first been predicted by various theories. It has been shown by MD simulations, for example, that the free energy of two solid-liquid interfaces can be smaller than that of a solid-solid interface.^{214,215}

In another study, Fensin *et al.*²⁰⁷ have performed MD simulations to analyze the short-range structural interactions and corresponding disjoining potential causing grain-boundary embrittlement. The analysis is compared with the width histograms determined with averaged order parameters as shown in Fig. 17(a). The comparison yields a remarkable dependence of the disjoining potential on the character of the grain boundary. It decays exponentially with a decay length of approximately 0.25 nm for a $\Sigma 9$ twist grain boundary in Ni. In contrast, the disjoining potential of a $\Sigma 9$ tilt grain boundary shows a weak attractive minimum.

In addition to various MD studies, grain-boundary premelting has also been addressed by other methods. Phase-field crystal simulations performed by Berry *et al.*²⁰⁸ are shown in Fig. 17(b). One of the outcomes was that the nature of the premelting strongly depends on the question whether the corresponding solid-liquid phase transformation in the bulk is strongly first-order or not. A multi-phase field model has been used¹⁵⁰ to study the effects of the grain size and therefore of the grain-boundary density on the premelting. It determines the extension of the temperature interval for the overheating of a grain boundary, before the bulk melting temperature is reached. While the bulk melting goes along with a vanishing disjoining potential energy, the premelting is characterized by a finite disjoining potential energy. Such a situation is shown in Fig. 17(c), where in particular, the relevance of triple junctions for the formation of liquid pockets of macroscopic size becomes noticeable.

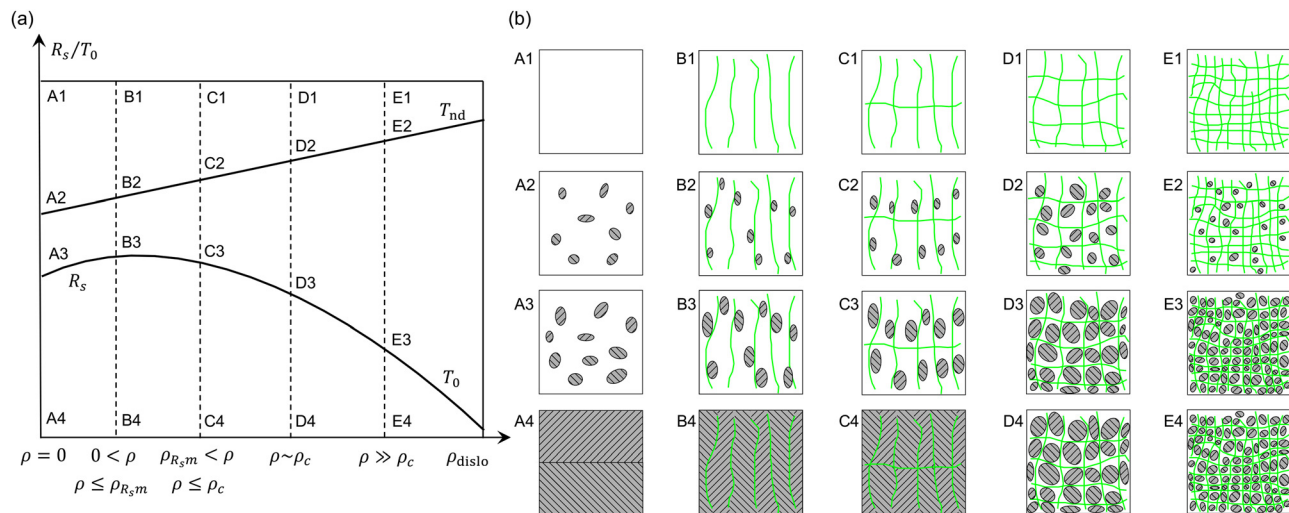


FIG. 14. (a) A simplified transition-temperature vs dislocation-density phase diagram of $\text{Ti}_{50}\text{Ni}_{45}\text{Fe}_5$, where the temperature of each microscopic picture is indicated. (b) Schematic illustration of the microscopic crossover behavior from normal R-martensite to dislocation-induced strain glass as a function of the dislocation density in $\text{Ti}_{50}\text{Ni}_{45}\text{Fe}_5$. The dislocations are depicted as green curved lines, while the R-martensite or nano-domains are represented in color gray and filled with oblique lines. Reproduced with permission from Zhang *et al.*, *Acta Mater.* **120**, 130 (2016). Copyright 2016 Elsevier.¹⁹⁷

One of the first experimental proofs has been provided by Divinski *et al.*²¹⁶ in the Cu–Bi system. To this end, they used radio-tracer diffusion measurements to detect the substantial enhancement in the grain-boundary diffusivity that is connected to the local transformation into the liquid state. At about the same time, Alsayed *et al.*²¹⁷ were able to visualize the premelting for colloidal crystals. The colloidal crystals were characterized by bright-field images of an upright microscope (Fig. 18). Here, every bright spot in the image represents a region of $0.75\ \mu\text{m}$ in diameter. The temperature is only slightly increased from the annealing temperature of $28.0\ ^\circ\text{C}$ to a measurement temperature of $28.2\ ^\circ\text{C}$. The impact on the grain boundary is, however, fundamental. One can clearly observe the molten structure in the grain boundary in Fig. 18.

Liquid–metal embrittlement is a related phenomenon that has been considered to be either caused by local electronic (i.e., charge transfer) or structural (“size”) effects induced by the presence of solute atoms at the grain boundary. In a recent article, Gibson and Schuh²¹⁸ used first-principles data to confirm that the grain-boundary cohesion (and hence embrittling tendency) correlate with the energy of the bonds formed by a solute. Lejcek and coworkers²¹⁹ critically evaluated and compared experimental and theoretical results on interfacial segregation in Ni and bcc Fe in both experiment and modeling. Furthermore, there have been a pool of atomistic modeling activities on the structure of interfaces and their impact on the microstructure (see, e.g., Ref. 220 for a review), including grain-boundary premelting and diffusion. Suggested mechanisms are the formation of strong directional bonds reducing dislocation motion during decohesion and structural-volumetric effects. However, these atomistic investigations are typically based on empirical interatomic potentials and do not

have, therefore, the advantages of first-principles approaches to fully resolve the electronic degrees of freedom.

D. Stacking faults

Stacking faults are intimately related to partial dislocations, and the stacking-fault energy directly determines the mobility of dislocations and thus materials deformation mechanisms. Naturally, stacking faults play an important role in the mechanical properties. A closely related example is that they may enhance the plasticity of metallic alloys through phase transformations. Beyond the mechanical aspect, stacking faults may also play some functional roles in semiconductors. For instance, in layered oxide electrode materials, stacking faults may enable a new phase transition path that stabilizes the electrode material and, thus, improves its energy storage performance.²²¹ We discuss the two types of roles of stacking faults in the following.

1. Transformation-induced plasticity

Stacking faults have a critical impact on the mechanical performance of structural materials and, in particular, of advanced high-strength steels. Alloying of Fe-based materials, e.g., by Mn can yield the stabilization of a stable or metastable fcc phase at room temperature. Under mechanical loads, specific deformation mechanisms, such as twinning induced plasticity (TWIP) and transformation induced plasticity (TRIP), are activated.²²² The latter is connected with a local phase transformation from austenite (fcc crystal structure) to ϵ -martensite (hexagonal close packed, hcp crystal structure). The

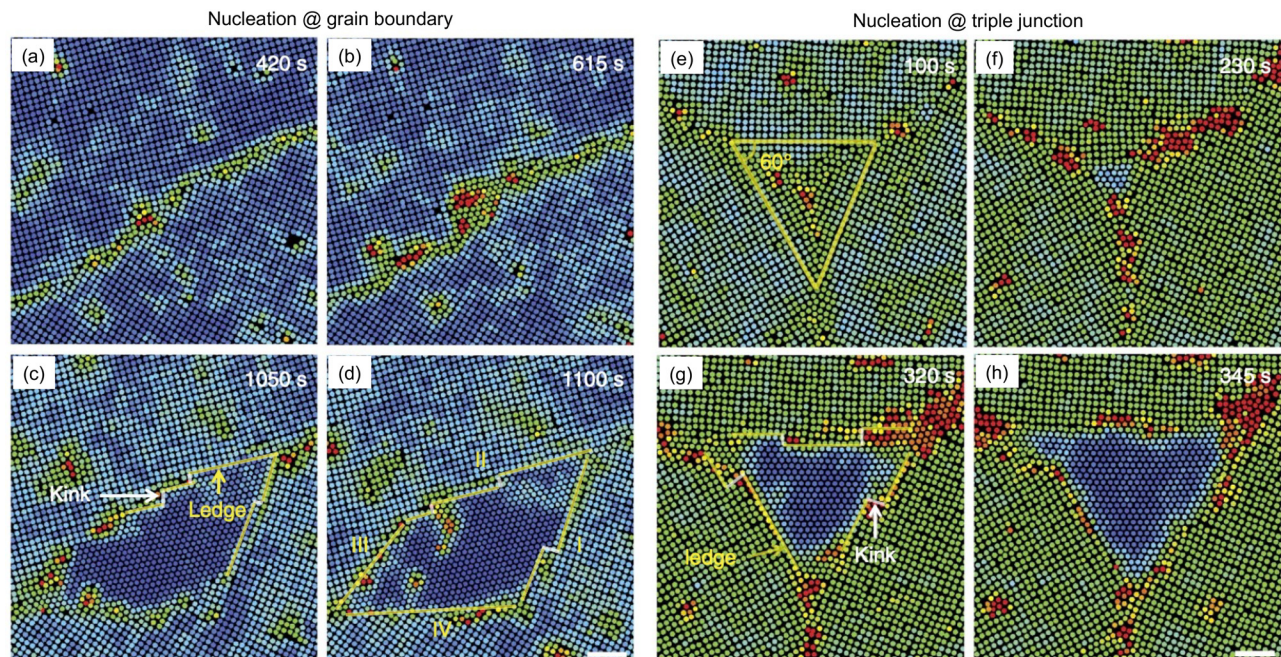


FIG. 15. (a)–(d) $\square \rightarrow \triangle$ nucleation at a grain boundary in a colloidal crystal with a flow velocity (v) of $36\ \text{nm s}^{-1}$. (e)–(h) $\square \rightarrow \triangle$ nucleation at a symmetric triple junction in a colloidal crystal with $v = 2\ \text{nm s}^{-1}$. The scale bar corresponds to $5\ \mu\text{m}$. The particles are colored according to the Lindemann order parameter. Reproduced with permission from Peng *et al.*, Nat. Commun. 8, 14978 (2017). Copyright 2017 Authors, licensed under a Creative Commons Attribution (CC BY) License.¹⁷¹

stacking fault energy is a key quantity, which controls the type of plasticity mechanism.²²³

In fcc materials, the intrinsic stacking fault (ISF) is a change of the stacking sequence from a periodic repetition of ABC to a sequence with one layer less, i.e., ABCAB | ABCABC (see also Fig. 5). As a consequence, the defect structure has locally the stacking sequence ABAB of an hcp crystal. In case an ISF is present on every second plane, the hcp phase extends over a larger region. Hence, the presence of the defect can have an impact on the martensitic phase transformation. This effect has, for example, been investigated with *in situ* neutron diffraction in CrCoNi medium entropy alloys.²²⁴ The quantitative analysis of the stacking-fault probability and the hcp volume fraction revealed that the formation and accumulation of ISFs are responsible for the fcc-hcp transformation. Similarly, it has been reported that an fcc-bcc phase transformation in shock-compressed noble metals is triggered by the presence of stacking faults.²²⁵

The connection between stacking faults and phase transformations is also reflected by the axial next-nearest-neighbor Ising (ANNNI) model,^{226,227} an established way to estimate the stacking-fault energy Γ_{SFE} . According to this model, the defect energy can be expressed by bulk energy differences: in lowest order, $\Gamma_{\text{SFE}} \approx E_{\text{hcp}} - E_{\text{fcc}}$.

Stacking faults that locally correspond to a different bulk phase are also observed in structurally more complex phases, like the C14 Laves phase. Here, the basal stacking-fault energy is described by the energy difference between the C15 and C14 phases.²²⁸ Stacking faults have, for example, been studied in the Nb-rich Fe₂Nb Laves phase.²²⁹ The bulk phase diagram of Fe-Nb indicates a low solubility of Nb in the C14 Laves phase, since the excess Nb will form the μ -phase with the composition Nb₆Fe₇. The experimental microstructure investigation has, however, revealed that the formation of this phase is suppressed due to the presence of a large number of different stacking faults.²²⁹ A detailed study of these defects has unveiled that some of

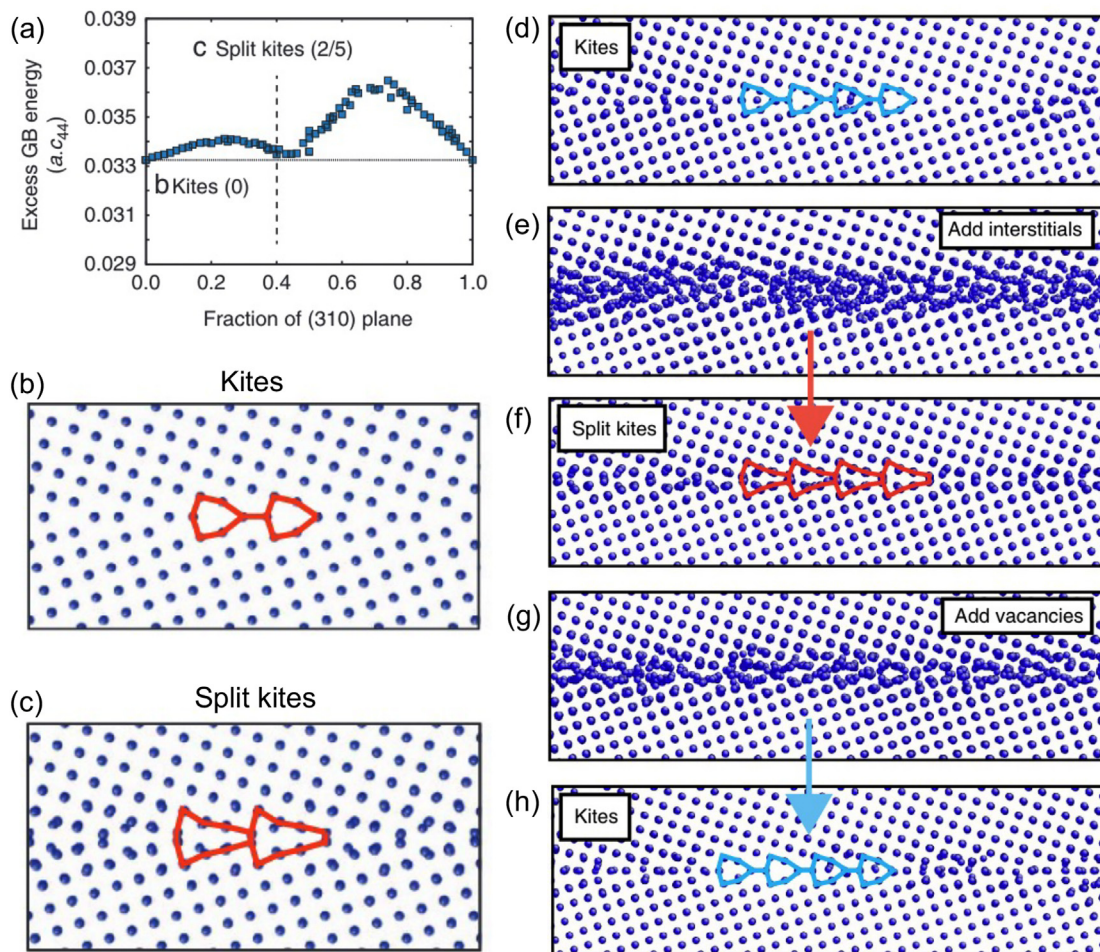


FIG. 16. (a) Grain-boundary energy vs atomic density in terms of fraction of atomic plane for the $\Sigma 5(310)$ grain boundary. (b) The kites structure for the $\Sigma 5(310)$ grain boundary. (c) The split-kites structure for the $\Sigma 5(310)$ grain boundary. (d)–(h) Grain-boundary phase transitions induced by point defects. (d) Initial normal-kite structure of Cu $\Sigma 5(310)$ grain boundary. (e) and (f) Transition from the normal-kite structure to a disordered state (e) and then to a split-kites structure (f), after adding interstitials to the grain boundary. (g) and (h) Subsequent transition to a disordered state (g) and then back to the normal-kite structure (h), after adding vacancies to the grain boundary. Reproduced with permission from Frolov *et al.*, Nat. Commun. 4, 1899 (2013). Copyright 2013 Authors, licensed under a Creative Commons Attribution (CC BY) License.²⁰⁶

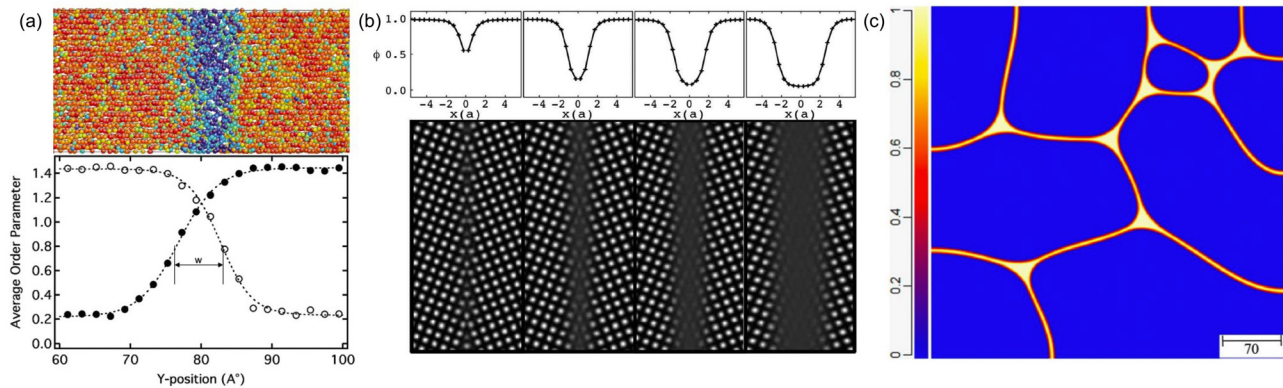


FIG. 17. (a) A snapshot of molecular dynamics simulation for a premelted grain boundary and the corresponding average order parameter vs distance across the grain boundary. The atoms are colored based on the order parameter. Reproduced with permission from Fensin *et al.*, Phys. Rev. E **81**, 031601 (2010). Copyright 2010 American Physical Society.²⁰⁷ (b) Phase-field simulation of grain-boundary premelting. Reproduced with permission from Berry *et al.*, Phys. Rev. B **77**, 224114 (2008). Copyright 2008 American Physical Society.²⁰⁸ (c) Phase-field simulation of grain-boundary premelting with the colors representing the order parameter. Reproduced with permission from Torabi Rad *et al.*, Sci. Rep. **10**, 21074 (2020). Copyright 2020 Authors, licensed under a Creative Commons Attribution (CC BY) License.¹⁵⁰

them contain one layer of the characteristic Zr_4Al_3 -type unit of the competing μ -phase, i.e., a phase that is stabilized by excess Nb. It should be called defect phase, because the confinement and stacking of atomic layers does not correspond to a bulk phase.

2. Intermediate phase formation

Stacking faults are very common planar defects in layered oxides,²³¹ which are key cathode materials for batteries. Upon charging and discharging various phase transitions can happen in these materials, which are critical for the electrochemical performance of batteries. Interestingly, stacking faults play a vital role in the phase transition kinetics in this context, which will be discussed here.

One of the commonly used sodium-ion battery cathode materials is $Na_{2/3}[Ni_{1/3}Mn_{2/3}]O_2$,^{232,233} which has a P2 crystal structure as

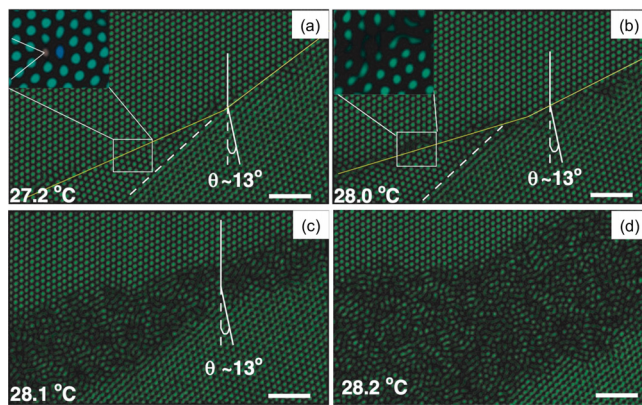


FIG. 18. (a)–(d) Experimental observation of grain-boundary premelting in a colloidal crystal with gradually increasing the temperature: (a) 27.2 °C, (b) 28.0 °C, (c) 28.1 °C, and (d) 28.2 °C. The scale bar corresponds to 5 μ m. Reproduced with permission from Alsayed *et al.*, Science **309**, 1207 (2005). Copyright 2005 AAAS.²¹⁷

shown in Fig. 19(a). When charged above 4.1 V, the P2 structure transitions to an O2 structure [see Fig. 19(a)].^{234,235} Atomistically, this phase transition is realized through gliding of the transition metal oxide slabs, which leads to a recoordination of the Na ions from trigonal prisms to octahedra. Consequently, the lattice along the c -axis undergoes a severe contraction, which is detrimental for the cycling stability.

By contrast, a structurally similar but chemically different cathode material P2- $Na_{2/3}[Fe_{1/2}Mn_{1/2}]O_2$ exhibits much better cycling stability compared to P2- $Na_{2/3}[Ni_{1/3}Mn_{2/3}]O_2$. The origin of the improved stability is that upon charging over 4.1 V a different phase transition pathway is adopted; instead of the O2 structure, a new phase with less severe volume contraction is formed. Despite the large number of studies on the identification and characterization of the new phase, the nature of the new phase has been heavily debated: some studies argued that the new phase has an OP4 structure (see, e.g., Ref. 236) as depicted in Fig. 19(a), while other findings suggested that the new phase is still an O2 phase but the Fe atoms migrate into tetrahedral sites of the Na layer (see, e.g., Ref. 237) because of this puzzling controversy, the new phase has also been termed “Z” phase.²³⁸

By employing *operando* XRD and STEM, Somerville *et al.*^{221,239} revealed the nature of the Z phase and recognized the importance of stacking faults for the new phase formation. They compared the *operando* XRD patterns of $Na_{2/3}[Ni_{1/3}Mn_{2/3}]O_2$ and $Na_{2/3}[Ni_{1/6}Mn_{1/2}Fe_{1/3}]O_2$ (i.e., with partial Fe substitution) during charging and discharging, where they observed clear differences when the voltage exceeds 4.1 V. For $Na_{2/3}[Ni_{1/3}Mn_{2/3}]O_2$, there is a decrease in the P2(002) intensity at $2\theta = 15.6^\circ$ and a new peak at $2\theta = 20.0^\circ$ appeared, which corresponds to the P2 \rightarrow O2 phase transition. However, as shown in Fig. 19(b), this is not the case for $Na_{2/3}[Ni_{1/6}Mn_{1/2}Fe_{1/3}]O_2$. The P2 (002) reflection peak at $2\theta = 15.6^\circ$ disappears and a new reflection arises at slightly greater 2θ , which is a signature of the Z phase. Once the Z phase is formed, Na ions can be continuously extracted through a solid-solution process, as evidenced by the gradual shift of the new reflection peak to greater 2θ values.

Using STEM measurements, they further peered into the structural information of the Z phase. As depicted in Fig. 19(c), Somerville *et al.*²²¹ found that the Z phase does not adopt the O2 structure, but contains a large number of O-type stacking faults. Instead of a solid solution upon Na extraction, the Z phase is actually a gradually evolving intergrowth structure.

The phase transformation mechanism is summarized in Fig. 19(d). Fe substitution disrupts the Na-ordering and the transition metal ordering in the P2 structure. Upon charging at voltages greater than 4.1 V, the extraction of Na⁺ from Na_{2/3}[Ni_{1/6}Mn_{1/2}Fe_{1/3}]O₂ generates highly depleted Na⁺ layers that are O-type stacking faults, which are distributed randomly in the P2 structure [Fig. 19(d)]. As charging further proceeds, the ratio of O-type stacking faults in the P2 structure increases. At 50% O-type stacking faults, the P2 phase transforms into a well-ordered structure of OP4 phase. Upon further charging, more O-type stacking faults are randomly formed in the OP4 structure, which may ultimately transform to a pure O2 phase [Fig. 19(d)].

This example nicely illustrates that stacking faults naturally appear in these layered oxides during charging or discharging, which serve as intermediate steps of the transitions between phases that differ in stacking type and sequence. The stepwise phase transition kinetics through stacking faults formation could profoundly enhance the cycling stability of the cathode materials and thus improve the electrochemical performance of batteries.

E. Surfaces

As a special type of planar defect, surfaces may also impact phase transition kinetics. While surface phases constitute a large research field on their own, surfaces affect phase transition kinetics in primarily two ways. First, as a major source of defects (e.g., vacancies, kinks, steps, etc.), surfaces influence phase transitions in the *bulk*. This effect is particularly pronounced when the system size approaches the nanoscale, where surface atoms constitute a large fraction of the material.²⁴⁰ Second, surfaces themselves may also experience phase transitions, leading to the formation of new phases in the vicinity of the surface. Common examples are surface reconstructions and surface-induced ordering.^{241,242} In this section, we illustrate these two aspects by using a few specific examples of the impact of surfaces on phase transition kinetics.

1. Undercooling of liquid droplets

Undercooling refers to the persistence of a liquid state below the melting point of a material. One reason why undercooling occurs is the small thermodynamic driving force (the difference in free energy between the solid and liquid) for the liquid-to-solid phase transition at the melting point; undercooling enhances the thermodynamic driving force. Furthermore, the nucleation kinetics is also affected by undercooling since in bulk materials the energy barrier for nucleation usually decreases with increasing undercooling.²⁴³

A typical undercooling to trigger the solidification of bulk liquids is only a small fraction of the melting temperature. Still, it strongly depends on the number of nucleation sites available within the melt, on the melt surface, or at the melt-container interface.²⁴⁴ For small liquid droplets, the number of nucleation sites is substantially reduced or may even be almost eliminated if the active nucleation sites are

primarily trace impurities. As the major source of defects that may catalyze nucleation in these droplets, surfaces play a decisive role in the nucleation kinetics and the maximum undercooling. These systems might be undercooled by $0.3 - 0.4T_m$ before nucleation occurs, where T_m is the melting temperature.²⁴⁵ For instance, it has been shown in the pioneering work of Turnbull and Cech²⁴⁶ that liquid droplets of Au (20–50 μm) could be undercooled by ~221 K using a Pyrex glass flux.

The impact of gas environment further demonstrates the importance of surface-related defects in accelerating the nucleation kinetics.²⁴⁷ For instance, when O₂ is added to an Ar gas environment (~500 ppm for O₂), the maximum undercooling of Au droplets is significantly reduced from ~212 K to ~120 K.²⁴⁸ This was explained by the fact that oxygen can be absorbed by the surface of liquid Au droplets or even diffuse into the droplets, which may lead to (surface) oxide formation that then acts as sites for nucleation.

To further reduce the surface sites that activate solidification and reach larger undercoolings, glass encapsulation can be employed. However, it has been found that an initial conditioning treatment that involves multiple, successive melting and freezing cycles is often required to achieve pronounced enhancement.²⁴⁹ The microscopic mechanism for this phenomenon was revealed by Wilde *et al.*²⁴⁸ they suggested that oxygen interacts with trace impurities, leading to the formation of defect complexes that may promote the nucleation kinetics. A self-consistent model that accounts for this effect was formulated. These examples demonstrate the critical impact of surface-related defects on phase transition (i.e., nucleation) kinetics, in particular by affecting the availability of suitable nucleation sites.

2. Phase transitions in nanoparticles

It is known experimentally that while approaching the nanoscale, materials may become stable in new phases,²⁵⁰ which are originally unstable or unfavorable in bulk materials under ambient conditions. In other words, crystal or grain size variations might also impose phase transitions and alter phase transition pathways. For instance, perovskite oxides, such as BaTiO₃ and PbTiO₃, undergo a cubic → tetragonal transition when gradually reducing the crystal size.^{251–255} Further examples include, but are not limited to, the hcp → fcc transition in Co,²⁵⁶ hcp → bcc transition in Ti,²⁵⁷ rutile → anatase transition in TiO₂,²⁵⁸ wurtzite → rock salt transition in CdSe and CdS,^{259,260} and tetragonal → monoclinic transition in the ZrO₂-Y₂O₃ system.^{261,262}

A number of mechanisms were proposed to explain the presence of these “unusual” phases in nanocrystalline materials,^{250,262} including a lack of nucleation sites,²⁶⁰ the Gibbs–Thomson effect (i.e., an enhanced internal pressure as a result of high surface/interface curvature),²⁶³ or surface-energy differences between allotropic phases.²⁵⁸ Among these mechanisms, the surface-energy difference argument has been most commonly adopted. The key idea is that, compared to bulk materials, the surface energy becomes more dominant in the total free energy of nanocrystalline materials, and unusual phases that have low surface energies may, thus, become energetically more favorable at small crystal sizes.

Figure 20 shows the impact of crystal size on the phase diagram of the ZrO₂-Y₂O₃ system.²⁶² The solid black lines depict the phase diagram of bulk ZrO₂-Y₂O₃.²⁶⁴ Using the DSC technique, the tetragonal → monoclinic phase-transition temperatures for different

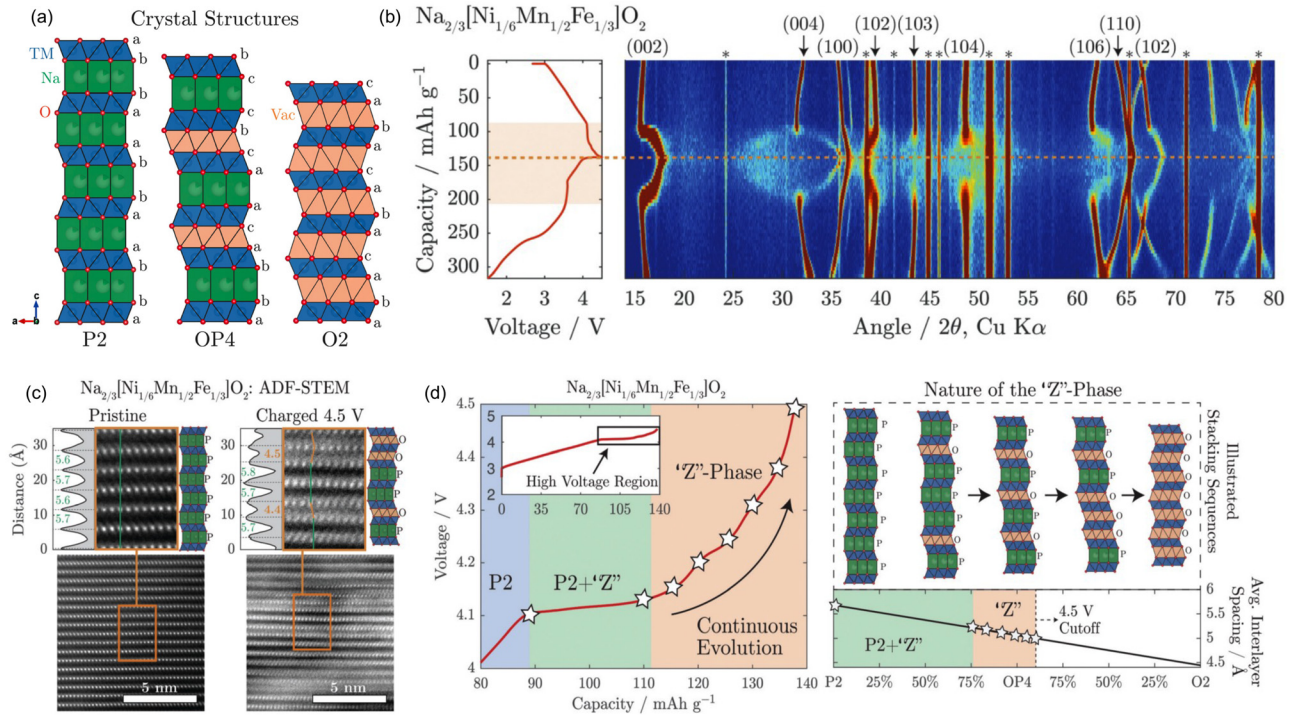


FIG. 19. (a) P2, OP4, and O2 crystal structures, and the corresponding stacking sequences. Here, “P” and “O” stand for trigonal prismatic and octahedral coordination, respectively.²³⁰ (b) Operando x-ray diffraction (XRD) analysis of the first complete electrochemical cycle for Na_{2/3}[Ni_{1/6}Mn_{1/2}Fe_{1/3}]O₂. (c) Scanning transmission electron microscopy (STEM) images of Na_{2/3}[Ni_{1/6}Mn_{1/2}Fe_{1/3}]O₂ pristine and charged to 4.5 V. The highlighted region shows the stacking layers in P-type without (green line) and O-type with (orange line) transition metal offset. (d) Mechanism of the transition from the P2 to O2 phases with the OP4 phase as an intermediate step in Na_{2/3}[Ni_{1/6}Mn_{1/2}Fe_{1/3}]O₂, leading to the formation of a “Z” phase; reproduced with permission from Somerville *et al.*, Energy Environ. Sci. **12**, 2223 (2019). Copyright 2019 Authors, licensed under a Creative Commons Attribution (CC BY) License.²²¹

compositions and different crystal sizes were measured. Furthermore, Mayo *et al.*²⁵⁰ derived the dependence of the transition temperature (T_c) on the crystal size (D),

$$T_c = \frac{\Delta H_{vol} + 10\Delta h_{surf}/D}{\Delta S_{vol} + 10\Delta s_{surf}/D}, \quad (6)$$

where ΔH_{vol} and Δh_{surf} are the volumetric and surface contributions to the total enthalpy difference between two phases, respectively. ΔS_{vol} and Δs_{surf} are the corresponding contributions to the entropy difference. By parametrizing the enthalpy and entropy differences, Mayo *et al.*²⁵⁰ calculated the tetragonal \rightarrow monoclinic transition temperatures for different compositions and different crystal sizes, which are shown by the dashed lines in Fig. 20. Clearly, a pronounced reduction of the transition temperature with decreasing crystal size is observed, which is mainly triggered by the surface-energy difference.

In addition to temperature-induced phase transitions, pressure-induced phase transitions also exhibit interesting transformation mechanisms in nanocrystals. For instance, the critical pressure of the wurtzite \rightarrow rock salt phase transition in CdSe increases with decreasing crystal size. Based on MD²⁶⁵ and transition path sampling simulations,^{266–268} the fundamental origin of the size dependence and a clear difference in the nucleation mechanism in nanocrystals as compared to bulk systems were revealed. The proposed mechanisms for the

wurtzite \rightarrow rock salt phase transition in CdSe include a concerted rearrangement,²⁶⁵ a coherent sliding of atomic planes,²⁶⁶ or nucleation at the surface followed by an atomic shuffle.^{267,268} Only the latter is consistent with the experimentally observed size trend in activation enthalpies, highlighting the importance of surface nucleations for phase transitions in nanocrystals.

In addition to unusual phase formation, pronounced size effects have also been observed for the phase separation temperature (e.g., in Cr–W alloys^{269,270}) or the miscibility gap (e.g., in Ni–Cu alloys^{271–273}). The clear crystal/grain size dependence demonstrates the important role of surfaces in the thermodynamics and kinetics of phase transitions, which becomes especially apparent in nanoscale materials.

3. Surface reconstruction and ordering

Surface reconstructions are a common phenomenon. Metallic surfaces often reconstruct to increase the surface packing density with either long-range migration or short-range displacements. Due to the directionality of covalent bonding, semiconducting surfaces often reconstruct by involving a number of atomic layers and forming more complex symmetries. A famous example is the (7×7) reconstruction of the Si(111) surface, which involves 49 sites of the surface layer and extends into a few subsurface layers.^{274–276} Even if a clean surface does

not reconstruct, reconstructions might also be induced by adsorption of foreign atoms or molecules.^{277,278} In addition to structural rearrangements, chemically disordered alloys might exhibit ordering in the vicinity of the surfaces as well. In the following, we employ specific examples to discuss surface reconstructions in metals and semiconductors, as well as surface-induced ordering.

Figure 21 schematically shows an example of surface reconstruction in ultrathin Fe films on Cu(001). Cu has an fcc crystal structure and the lattice constant is also close to that of fcc Fe, which is unstable at room temperature. Hence, experimentalists attempted to grow thin fcc Fe films on Cu substrates. However, the atomic structure of the grown ultrathin Fe films on Cu(001) is not fcc but exhibits thickness-dependent structural modulations [see Fig. 21(a)] and magnetic configurations.^{280–282} As shown in Fig. 21(b), there exist three distinct regions. In region I ($1 < N \leq 4$ ML), the entire film experiences lattice modulations with a ferromagnetic (FM) state. In region II ($1 < N \leq 10$ ML), only the top two layers are modulated; the film switches to an overall antiferromagnetic (AFM) state with the top two layers always ferromagnetically coupled. In region III ($N > 10$ ML), the entire film transitions to FM bcc Fe without any surface reconstruction.

Despite the fact that the complex surface reconstructions in ultrathin Fe films on Cu(001) have been observed experimentally using different techniques, the atomic nature and origin of the modulated structure had been puzzling for a long time. Zhang *et al.*³⁵ approached this problem from the perspective of phase transitions with the presence of surfaces and interfaces. Employing first-principles NEB calculations, they found that the modulated structure stems from an intermediate structure along the transition pathway of FM fcc \rightarrow bcc Fe within the Pitsch²⁷⁹ orientation relationship as enforced by the substrate [see Fig. 21(c)]; the intermediate structure discussed here is the same as the MIS discussed in Sec. IV A 1. Hence, different regions observed in experiments can be interpreted as the result of an fcc \rightarrow MIS \rightarrow bcc transition in Fe at different film thicknesses.

As mentioned above, the (7×7) reconstruction of Si(111) is one of the most complicated surface phase transitions.²⁸³ The final reconstructed surface contains defective units such as dimers, adatoms, and stacking faults.²⁸⁴ Even though the exact atomic structure of this reconstruction has been systematically characterized and interpreted, the atomistic mechanism for the formation kinetics of the reconstruction had been a mystery for more than half a century.

The large size of the Si(111)- (7×7) reconstruction sets a computational challenge for first-principles simulations. Typical empirical potentials for Si are, unfortunately, not able to capture the correct ground-state structure of this reconstruction. Recently, Hu *et al.*²⁸⁵ developed an accurate artificial neural-network potential for Si and employed the potential to study the atomistic mechanism of the kinetic formation process of the Si(111)- (7×7) reconstruction. They systematically revealed a step-mediated atom-hop rate-limiting process, which triggers massive non-conserved rearrangements of atoms. A key ingredient of the atomistic mechanism is collective vacancy diffusion [see Fig. 22(a)], which further mediates a sequential pattern formation of selective dimers, corner holes, stacking faults, and dimer lines. Ultimately, this sophisticated atomistic process leads to the formation of the complex Si(111)- (7×7) reconstruction [see Figs. 22(b) and 22(c)].

Alloys are oftentimes chemically disordered, but they can undergo a disorder \rightarrow order transition in the vicinity of the

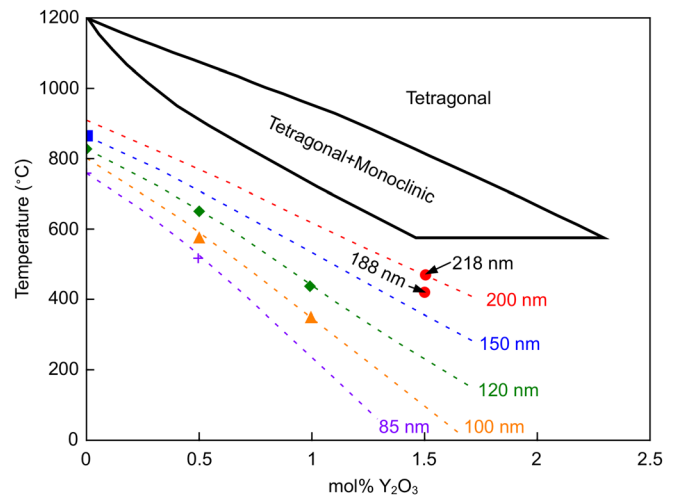


FIG. 20. Decrease of tetragonal \rightarrow monoclinic phase-transition temperature with reducing the crystal size of $\text{ZrO}_2\text{-Y}_2\text{O}_3$ powders. Reproduced with permission from Suresh *et al.*, *J. Mater. Res.* **18**, 2912 (2003). Copyright 2003 Materials Research Society.²⁶²

surface.^{286–292} For instance, chemically ordered $\text{Al}_x\text{Ga}_{1-x}\text{N}$ surface alloys ($0 < x < 1$) have been experimentally observed using TEM and XRD.²⁹¹ The surface-induced chemical ordering changes the bandgap and other optical properties of the alloys as compared to the disordered alloys. Thus, the surface chemical ordering adds an additional degree of freedom to tune the electronic and optoelectronic properties of semiconductor alloys. Using first-principles calculations, it was found that the chemical ordering results from the growth kinetics at surface steps. The Al–N bond is stronger than the Ga–N bond, because of which incorporation of Al atoms on certain crystallographic sites (B2) at surface steps is energetically preferable during growth. Recently, a new chemical intraplane ordering was first observed in a nominal InN monolayer epitaxially grown on GaN(0001).²⁹² The surface was identified to be a chemically ordered $\text{In}_x\text{Ga}_{1-x}\text{N}$ alloy with a mean In concentration of 25%. This chemical ordering was rationalized by an elastically frustrated rehybridization (from sp^3 to planar sp^2) mechanism, which prevents In atoms from occupying low-coordinated surface sites.

Beyond crystalline materials, the surfaces of amorphous materials might also exhibit special ordering that is absent in the bulk. For instance, when compacting amorphous particles of $\text{Fe}_{90}\text{Sc}_{10}$, the surfaces undergo structural and magnetic transitions.^{293,294} The paramagnetic disordered surfaces that are brought in close contact transform to an interface structure with special medium-range order coupled with ferromagnetism.²⁹⁵ Making use of this transition, the concept of nanoglasses (i.e., amorphous domains connected by interfaces as transformed from amorphous surfaces) has been proposed,^{296,297} which opened up a new pathway to improve the properties of glasses.

F. Interfaces

In this section, we focus on interfaces between different phases, i.e., phase boundaries, which directly link the parent and product phases during phase transitions. Naturally, one may expect that these

interfaces impact or even dominate the phase transition kinetics, since the phase transition occurs in the vicinity of the interface and proceeds via interface migration. Indeed, as we will show in the following, the constraints and chemomechanical coupling at the interfaces have a profound influence on the atomic displacements/rearrangements and atomic diffusion, which, thus, directly shape the phase transition kinetics.

1. Adaptive martensite

In Ni–Mn–Ga magnetic shape-memory alloys, there is a martensitic transition from cubic $L2_1$ austenite to tetragonal $L1_0$ martensite [see Fig. 23(a)] while cooling from high to low temperatures.^{299,300} After the martensitic transformation, in addition to the tetragonal martensite, there are also a number of so-called modulated phases [see, e.g., the 5M phase in Fig. 23(a); here “5” denotes the periodicity along the c direction] that have been experimentally observed.^{301–303} It has been shown that the presence of the modulated phases are actually essential to achieve high field-induced strains and entropy changes in moderate magnetic fields.³⁰⁴

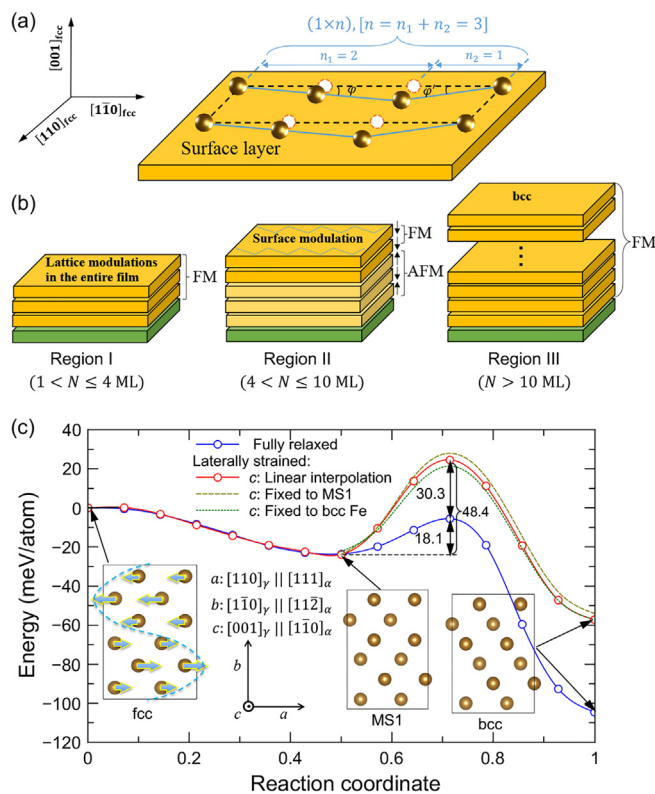


FIG. 21. (a) Schematic illustration of the $(1 \times n)$ reconstructions in ultrathin Fe films on Cu(001). (b) Thickness-dependent surface reconstructions including three distinct regions. N is the number of monolayers (MLs). “FM” refers to ferromagnetic state and “AFM” denotes antiferromagnetic state. (c) Minimum-energy paths of the fcc \rightarrow bcc Fe transition within the Pitsch²⁷⁹ orientation relationship. Reproduced with permission from Zhang *et al.*, Phys. Rev. Lett. **118**, 073106 (2017). Copyright 2017 American Physical Society.³⁵

The modulated phases have relatively complicated crystal structures, making them difficult to interpret and understand, even though the exact crystal structures can be determined based on experimental techniques such as XRD. Motivated by the concept of “adaptive phase formation” as first suggested by Khachatryan,^{308,309} Kaufmann *et al.*³¹⁰ proposed a physically very intuitive mechanism to rationalize the formation of the modulated phases in Ni–Mn–Ga alloys; the modulated phases were termed “adaptive martensite.”

The central idea of adaptive martensite is that the modulated phases should not be considered as thermodynamically stable bulk phases, instead they are metastable structures characterized by ultra-fine twinning. As schematically shown in Fig. 23(b), the modulated phases are formed by adapting to interfacial constraints of the austenite phase at the habit plane (i.e., the interface); the formation of the adaptive modulated martensites could help to minimize the elastic energy at the interface due to lattice mismatches between cubic austenite and tetragonal martensite. Different modulated phases (such as 5M, 7M, 9M, 10M, and 14M) are characterized by different twinning periodicities as a result of different lattice mismatches at the habit plane. However, consistently, all of the phases can ultimately be traced back to the non-modulated (NM) tetragonal martensite phases in the form of nanotwin lamellae.

The key requirements for the concept of adaptive martensite to work are twofold: (i) a simple martensitic transformation path, and (ii) a very low nanotwin boundary energy. To more intuitively and quantitatively discuss these aspects, we look at another example of adaptive martensite formation in an fcc $Fe_{70}Pd_{30}$ alloy, which was demonstrated by Kauffmann-Weiss *et al.*²⁹⁸ using both theory and experiment. As depicted in Fig. 23(c), when the ideal relative atomic positions is fixed in the fcc $Fe_{70}Pd_{30}$ alloy and only the tetragonality (c/a ratio) is varied, the fcc austenite phase is most stable. However, if one allows atomic relaxations, the bcc phase becomes the ground state, and in addition to the bcc phase ($c/a = 0.707$) there is also another metastable minimum at $c/a > 1$. The bcc phase corresponds to the stable non-modulated phase, which can be transformed from the fcc austenite via the simple Bain path. The metastable structure at $c/a > 1$ is actually an adaptive martensite, which can be formed by a simple tetragonal deformation of the fcc austenite along the opposite direction of the Bain path plus additional adaptive twinning [see the inset of Fig. 23(b)].

Figure 23(d) shows the twin-boundary energy (γ_{twin}) as a function of the tetragonality of the twinned adaptive phase (c/a_{twin}). It can be seen that the twin-boundary energy decreases dramatically with increasing tetragonality, which implies that the adaptive martensite has an extremely low twin-boundary energy. This is the reason why the adaptive martensite is energetically favorable to form, despite the fact that as a “bulk” phase, it has a higher energy than the ground-state non-modulated martensite [see Fig. 23(c)].

The example of adaptive martensite formation nicely demonstrates the important impact of interfaces on phase transition kinetics and intuitively shows how the interfacial constraints due to lattice mismatches alter the transformation pathway and lead to the formation of metastable adaptive modulated phases. When simulating phase transformation kinetics, in particular, for cases where coherent interfaces can be formed, the elastic energy due to interfacial lattice mismatches needs to be carefully taken into account. To minimize the elastic energy at the interface, the phase transition may adopt different pathways.

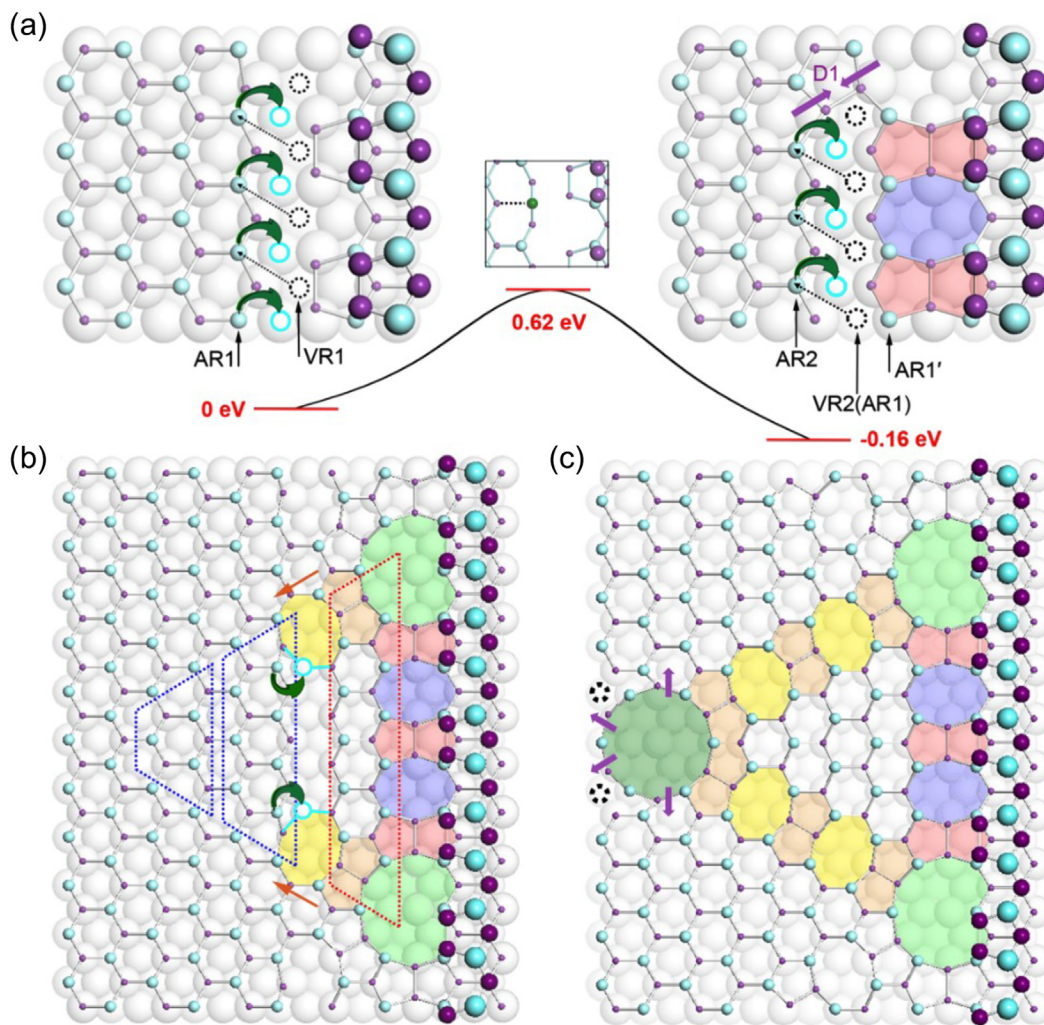


FIG. 22. (a) Collective vacancy diffusion during the formation of Si(7 × 7) reconstruction. (b) The resulting atomic structure of the collective vacancy diffusion. (c) The final reconstructed structure, corresponding to the faulted half unit cell of Si(7 × 7) reconstruction. Reproduced with permission from Hu *et al.*, Phys. Rev. Lett. **126**, 176101 (2021). Copyright 2021 American Physical Society.²⁸⁵

2. Heterophase interfaces

For structural transformations between two different crystal-line phases that proceed via nucleation and growth, the properties of the heterophase interface significantly impact the transformation kinetics. As the transformation is characterized by structural rearrangements at the interface, the velocity of the phase boundary strongly depends on the orientation relationship, the mismatch, the density, etc. The $\square \rightarrow \Delta$ phase transition in colloidal crystals discussed in Sec. IV C 1 exhibits a strong correlation between the coherency of the interface and the mobility of the phase boundary. During growth, the interface velocity is lowest perpendicular to coherent interfaces and highest perpendicular to incoherent interfaces.¹⁷⁰ A disordered interface layer that is most pronounced at incoherent interfaces enhances the mobility of particles and, consequently, of the interface.

As an example of heterophase interfaces in metallic systems, we discuss the transformation between cubic and topologically close packed (TCP) phases.³¹¹ These are of importance in high-performance alloys, such as Ni-based superalloys³¹² and steels,³¹³ where the formation of TCP-phase precipitates affects the materials properties. In elemental W, the transformation between bcc and A15 (one of the TCP phases) is of particular interest since bcc W is a promising candidate for metallic interconnects in microelectronics,^{314–316} while A15 W is considered for spintronic devices based on the spin Hall effect.^{317–319}

The transformation mechanism between bcc and A15 has been studied computationally for a model system in Mo with AKMC³⁰⁵ (see Sec. III A 3). In Fig. 24(a), a setup of the simulation cell is shown, indicating a disordered interface region that facilitates the structural rearrangement during phase boundary migration, similar to the

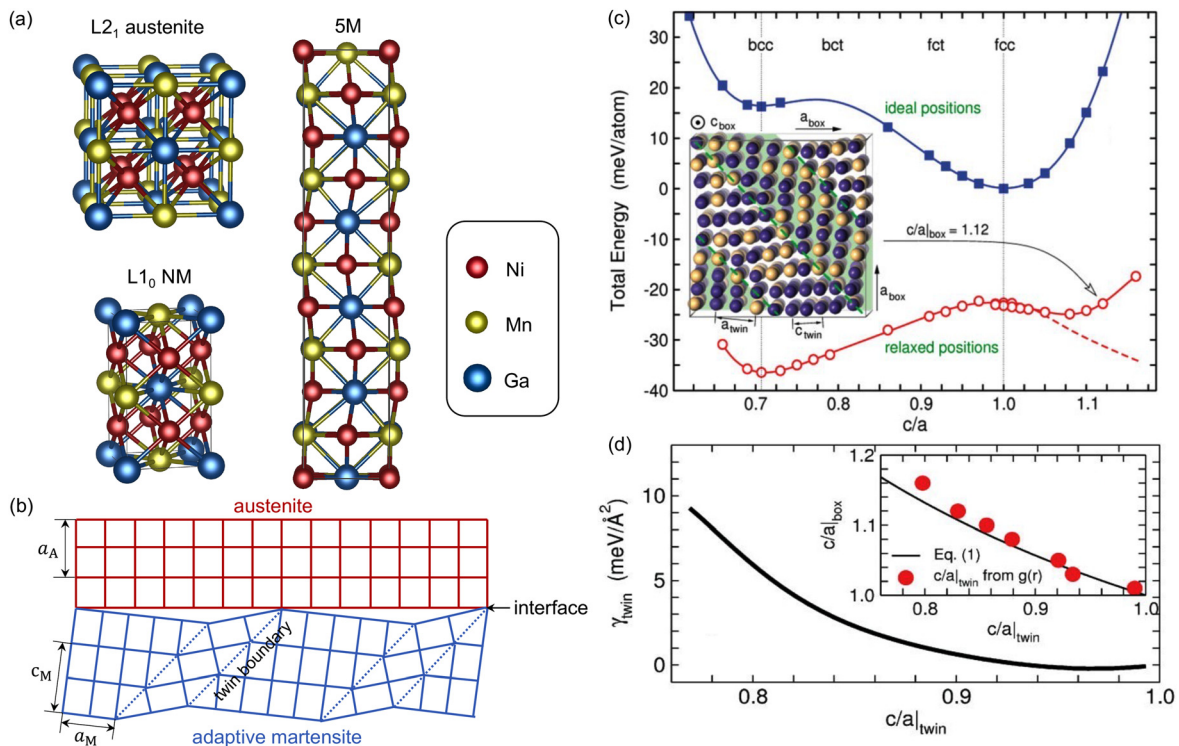


FIG. 23. (a) Crystal structures of $L2_1$ austenite, $L1_0$ non-modulated (NM), and 5M modulated phases. (b) Schematic illustration of the formation of adaptive martensite at interfaces to satisfy matching of lattice constants. (c) *Ab initio* computed total energy of Fe-Pd alloys as a function of the tetragonality (i.e., c/a ratio). (d) Twin-boundary energy (γ_{twin}) as a function of the tetragonal distortion of the twin ($c/a|_{twin}$). The inset depicts the correlation of the tetragonal distortion of the *ab initio* simulation box ($c/a|_{box}$) representing the epitaxial constraint and the resulting tetragonal distortion of the twin ($c/a|_{twin}$). (c) and (d) Reproduced with permission from Kauffmann-Weiss *et al.*, Phys. Rev. Lett. **107**, 206105 (2011). Copyright 2011 American Physical Society.²⁹⁸

experimental observations for colloidal particles. The change in potential energy during an AKMC simulation is displayed in Fig. 24(b), which exhibits plateau regions between a decrease in energy as the transformation takes place. The plateau regions can be associated with the formation of a new bcc layer as the transition proceeds layer-by-layer. An Arrhenius plot of the rate constants for the formation of a bcc layer extracted from the AKMC simulations is shown in Fig. 24(c), where the slope yields an effective barrier of $\Delta E \approx 0.5$ eV for the transformation mechanism through the disordered interface. This effective barrier and, correspondingly, the mobility of the phase boundary cannot be associated with a single atomistic mechanism but reflects the features of the complex energy landscape explored during the transformation.

The bcc-A15 transformation has also been studied by a combination of the solid-state dimer (SSD)⁵⁴ and SSNEB⁵³ approaches. The dimer method¹²⁵ is a single-ended saddle point search, where, in contrast to NEB, only the initial configuration is required. In SSD, both the cell and atomic degrees of freedom are evolved together, which is essential in the study of phase transformations. The concerted mechanism for the bcc-A15 transformation obtained with SSD in a small simulation cell was used to create an initial path for subsequent SSNEB calculations. The relaxed MEP revealed a nucleation and growth mechanism with again several smaller barriers associated with the formation of new bcc layers during the transformation.⁵⁴

The disorder at the heterophase interface results in a very rugged energy landscape with a large number of shallow, local minima representing the different arrangements of atoms in the disordered layer, similar to an amorphous phase. This makes it challenging and computationally expensive to sample with, for example, AKMC. Enhanced sampling schemes that sweep over the energy landscape and project the free energy along a given, low-dimensional collective variable (CV) can alleviate this problem. It is, however, not entirely trivial to construct a CV that properly represents the complex mechanism of the phase boundary migration.

In Ref. 306, a machine-learning approach was used to classify the local, structural environment around each atom [Fig. 24(d)]. The output of the classification neural network (NN) can be combined into global classifiers and the phase transformation described as a path in this classifier space.^{306,307} This approach does not assume any particular atomistic mechanism but utilizes the decision function of the classification NN to locally drive the system between different structural motifs. The resulting CV was then used in combination with metadynamics^{96–98} and driven adiabatic free-energy dynamics (d-AFED)^{99–101} to enhance the sampling of the phase space. The evolution of the CV during a number of d-AFED simulations is shown in Fig. 24(e). Again, several plateau regions can be identified that correspond to the formation of new bcc layers during the transformation. Note that the transformation in the enhanced sampling can be

observed within a few nanoseconds, whereas in an unbiased simulation, the transformation takes place on the order of tens of microseconds, highlighting the significant speedup in the exploration of the phase space. The potential of mean force along the corresponding CV extracted from several d-AFED runs is shown in Fig. 24(f). The energy profile exhibits a series of minima separated by barriers of $\Delta F \approx 0.5$ eV. This again reflects the layer-by-layer transformation through a disordered interface as also seen in the AKMC study.

The transformation enthalpy and effective barrier for the bcc-A15 transformation of W thin films have been assessed in a combined experimental and theoretical study.³²⁰ The results of first-principles calculations and high-temperature MD simulations were in good agreement with the values extracted from DSC measurements for these quantities. The transformation mechanism was again described as proceeding via a collective rearrangement of atoms in the disordered interface layer.

As discussed in Sec. IV A 1, the presence of interstitials can greatly affect the transformation kinetics. This has also been observed for the bcc-A15 transition in W thin films when doping with O. A recent experimental and theoretical study revealed the impact of O in driving the transformation from bcc to A15.³²² As the amount of O in the bcc phase is increased, it induces a distortion of the lattice such that the local environment around the O interstitials becomes comparable to A15, indicating that O doping promotes the transformation from bcc to A15 and also stabilizes the A15 phase.

Recently, it has been shown by both HRTEM imaging and atomistic simulations that misfit dislocations at the heterophase interface of Cu/Cu₂O have a critical impact on the phase transition kinetics.³²³ The lateral flow of interfacial ledges is pinned at the core of dislocations until the dislocation migrates to the new interface location during the phase transition. This leads to a stop-and-go mechanism for the interfacial phase transition kinetics as induced by misfit dislocations at the heterophase interface. For heterophase interfaces where the transformation between the different crystalline phases requires a significant rearrangement of atoms, the formation of disordered or amorphous regions appears to be of importance in determining the transformation kinetics. In addition, the presence of interstitial defects can affect the relative stability and transformation mechanism, which needs to be taken into account in the study of these systems.

3. Interfacial complexions

An interfacial complexion refers to a metastable interfacial state confined and stabilized at the interface of the adjacent phases.³²⁴ It can adopt states that have distinct interfacial structures and/or composition profiles correlated with local minima in free energy and may undergo reversible structural transitions when the thermodynamic conditions vary. In this case, the interface itself is also a confined phase with finite thickness, and may participate in the bulk phase transition. In the following, we use two examples to show how interfacial complexions are formed and how they may influence the phase transition kinetics: one is about diffusional-displacive pearlite transformation in Fe-C alloys, and the other relates to diffusionless martensitic transformation in Ti alloys.

Pearlite is an important microstructure in steels,³²⁶ which is formed by a decomposition of fcc austenite (γ phase) into bcc ferrite (α phase) and orthorhombic carbide cementite (Fe₃C). When ferrite

and cementite are periodically arranged in a lamellar manner, the microstructure is termed pearlite (in contrast to another microstructure named bainite) [see Fig. 25(a)].

The pearlite transformation involves three phases and multiple interfaces, because of which the phase transformation kinetics is very complicated. Of particular interest and importance is the diffusion and redistribution of C atoms. Fcc austenite has a large C solubility, but bcc ferrite can only accommodate a very small concentration of C atoms. During the decomposition of austenite into ferrite and cementite (25 at. % C), C would need to diffuse toward the interface and accumulate in some way to form cementite.

Despite the fact that this is a text-book phase transformation in such a conventional material system, the mechanism of this transformation including the redistribution of C at the interface is not well understood. For instance, Fig. 25(b) shows the experimentally measured growth velocities of pearlite at different temperatures, in comparison with simulation results. Even though the pearlite lamellar microstructure can be nicely simulated using phase field [Figs. 25(c) and 25(d)], the theoretically obtained growth velocities are drastically lower.

In particular, Nakajima *et al.*³²¹ systematically investigated the impact of different C diffusion pathways on the phase transition kinetics. They considered two scenarios: (i) C only diffuses in austenite, and (ii) C also diffuses in ferrite in addition to scenario (i). As a result, scenario (ii) indeed enhances the growth velocities of pearlite as compared to scenario (i); however, the magnitude of the growth velocities is still much lower than the experimental values. This clearly demonstrates that our understanding of the atomistic pearlite transformation mechanism is limited and incomplete, in particular, the C diffusion and redistribution mechanisms at the interfaces.

To understand the complete atomistic picture of the pearlite transformation, Zhang *et al.*³²⁵ approached this problem from a different perspective. They started from analyzing the crystal structure of the complicated carbide cementite and relaxed the atomic structure of cementite after removing C atoms from this phase employing first principles. Interestingly, this relaxation did not lead to ferrite, but a new structure that is between fcc austenite and bcc ferrite. This new structure is not a stable bulk phase, but is only metastable due to the interfacial confinement, i.e., an interfacial complexion.

The new structure naturally connects austenite, ferrite, and cementite and forms the basis for a unified set of transition pathways and interfaces between three phases [see Fig. 26(a)]. The unified transition pathways always proceed via the new structure as an intermediate step, because of which the new structure is called MIS as we also discussed in Sec. IV A 1.

By performing SSNEB calculations, the atomistic mechanisms for the structural transformations among austenite, ferrite, and cementite were revealed [Fig. 26(b)]. The MIS serves as a central link for the three phases, and structural transitions can take place by shuffling the Fe lattice coupled with periodic C segregation.

Since the austenite/ferrite and austenite/cementite interfaces have now been characterized as MIS, this interfacial complexion may also enable fast diffusion and provide redistribution channels for C atoms at the interface, which may explain the observed discrepancy between phase-field simulations and experiments for pearlite growth velocities. More detailed investigations into the kinetics are still required.

This example intuitively shows how important the interface is for the phase transition kinetics and how an interfacial complexion, such

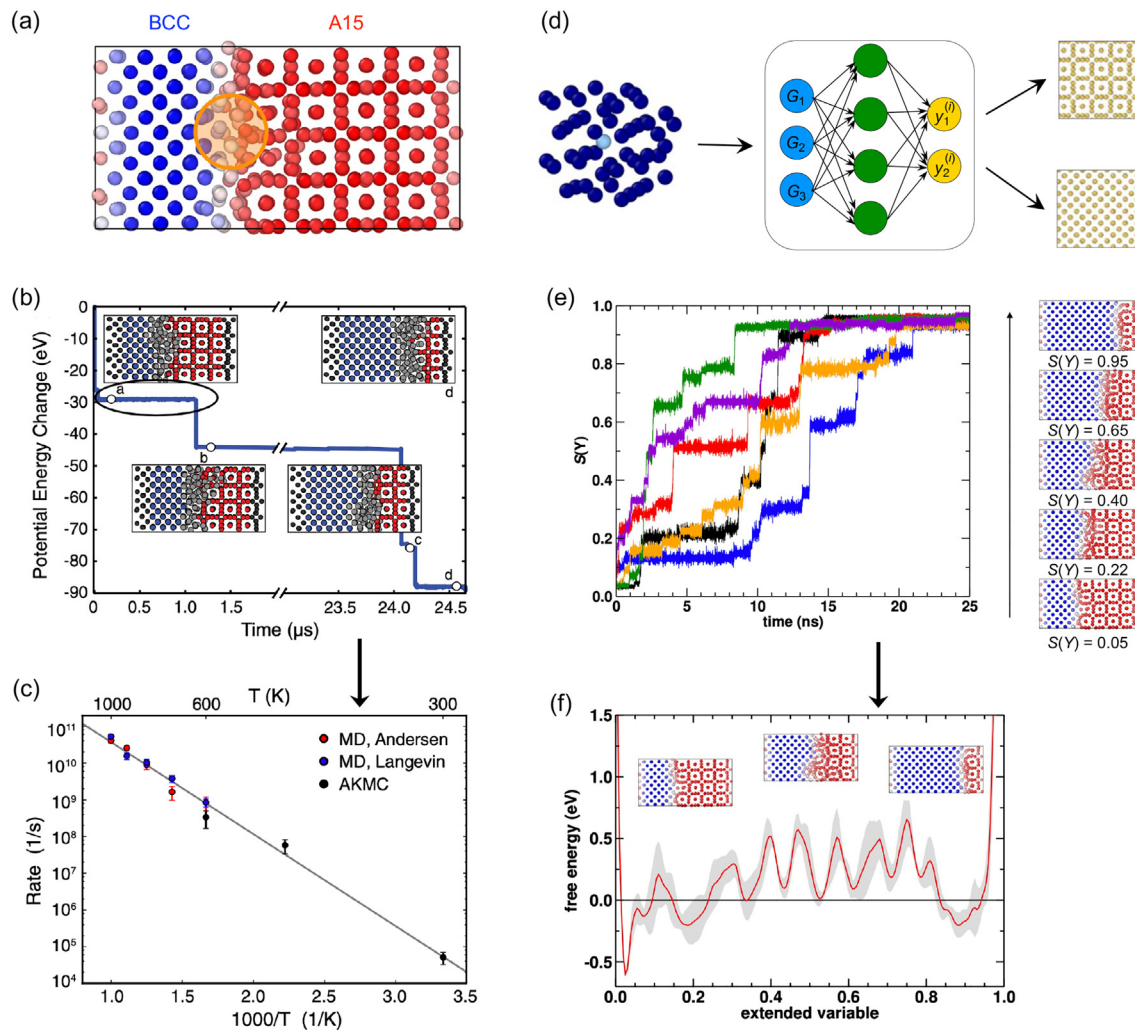


FIG. 24. (a) Illustration of the interface between bcc and A15 phases. Blue atoms represent the bcc phase and red atoms are the A15 phase. (b) Evolution of potential energy during an adaptive kinetic Monte Carlo (AKMC) simulation at $T = 300$ K and snapshots indicating the transformation mechanism from the A15 (red spheres) to the bcc phase (blue spheres). (c) Arrhenius plot for the layer transformation rate of a bcc layer extracted from AKMC simulations. The slope yields an effective barrier for the layer transformation of $\Delta E \approx 0.5$ eV. Reproduced with permission from Duncan *et al.*, Phys. Rev. Lett. **116**, 035701 (2016). Copyright 2016 Authors, licensed under a Creative Commons Attribution 3.0 License.³⁰⁵ (d) Schematic of a machine-learning-based local structure identification. (e) Evolution of the collective variable during driven adiabatic free energy dynamics (dAFED) at $T = 300$ K. The enhanced sampling facilitates a fast exploration of the phase space and the transformation can be observed within a few ns. (f) Potential of mean force extracted from dAFED simulations. The energy profile indicates an effective barrier of $\Delta E \approx 0.5$ eV, similar to the one extracted from the AKMC simulations. Adapted with permission from Rogal *et al.*, Phys. Rev. Lett. **123**, 245701 (2019). Copyright 2019 American Physical Society.³⁰⁶ Reproduced with permission from J. Rogal and M. E. Tuckerman, *Multiscale Dynamics Simulations: Nano and Nano-bio Systems in Complex Environments*. Copyright 2021 Royal Society of Chemistry.³⁰⁷

as the MIS, may facilitate unified transformation pathways and fast channels for solute diffusion and redistribution.

The above example focuses on diffusional-displacive transformation, where an interfacial complexion plays a critical role in the phase transition kinetics. However, also for purely displacive martensitic transformation, interfacial complexions can be essential for the phase transition pathways. For instance, Zhang *et al.*³²⁷ recently identified an interfacial-complexion-mediated martensitic phase transformation in the Ti-23Nb-0.7Ta-2Zr (at.%) system, which is a high-temperature shape-memory alloy. The shape-memory effect originates from a

reversible $\beta \rightarrow \alpha''$ martensitic transformation under temperature and stress variations. The $\beta \rightarrow \alpha''$ martensitic transformation is thermo-elastic and results in a microstructure with self-accommodated α'' twins. Also, the system is strongly prone to a $\beta \rightarrow a\text{-}\omega$ transition upon cooling. The transformation paths and kinetics of both $\beta \rightarrow \alpha''$ and $\beta \rightarrow a\text{-}\omega$ transitions are very sensitive to alloying elements and external/local stresses.

As shown in Fig. 27, during the $\beta \rightarrow \alpha''$ transition, the growth of α'' martensite builds up a shear stress along the phase or twin boundaries. With distinct thermodynamic conditions, the interfaces promote

the matrix to overcome a low free-energy barrier of the $\beta \rightarrow a\text{-}\omega$ transition. The $a\text{-}\omega$ is, in principle, thermodynamically unstable at this temperature, but it is formed and stabilized with the assistance of stress [Figs. 27(a) and 27(b)]. The formation of $a\text{-}\omega$ interfacial complexions accommodates the α''/β interfacial strain and hence decreases the interfacial stress [step 2 in Fig. 27(a)]. When the local stress drops to values below the critical value, the growth of $a\text{-}\omega$ layers stops, since the $a\text{-}\omega$ is still thermodynamically unfavorable, and subsequently step 3 in Fig. 27(a) proceeds. This is also the reason why the occurrence of $\beta \rightarrow \alpha''$ transition is strictly confined to the interface region. As the $a\text{-}\omega$ transformation produces shear along the $(\bar{2}11)[\bar{1}\bar{1}\bar{1}]_{\beta}$ component, α''_{τ} of the $\{220\}_{\alpha''}/\{211\}_{\beta}$ compound twinning character is formed due to the requirement of interface energy minimization. This is in contrast with binary Ti–Nb, where one step $\beta \rightarrow \alpha''$ transition occurs with the major twinning mode of $\{111\}_{\alpha''}$ type-I twinning and no compound twins. As a result, a new transformation-induced interfacial complexion of ω structure is found.

It possesses the athermal character and reversibility through the reversible $\beta \rightarrow a\text{-}\omega$ transition. The confinement and reversibility of this interface nanolaminate, consisting of adjacent orthorhombic α'' , hexagonal ω and twinned α'' nano-layers inside the host β matrix realize an interfacial complexion state [Fig. 27(c)]. It forms from the β matrix to accommodate the interfacial strain of α''/β phase boundaries during $\beta \rightarrow \alpha''$ martensitic transition and further mediates the transition kinetics by influencing the twinning mode to be $\{220\}_{\alpha''}$ compound twin and results in a final nanolaminate composite microstructure throughout the bulk Ti alloy upon cooling [Fig. 27(d)].

4. Morphology of nanoprecipitates

During the structural transformation from matrix to precipitates, the kinetics and the morphology of the precipitates may be dominated by the energetics of the involved interfaces between the precipitates and the confining matrix. This has been demonstrated in a recent study³²⁸ of Fe_3C precipitation in the well-established Fe–C system [Fig. 28(a)]. Fe_3C was found to grow along a particular direction as indicated by the red arrow in Fig. 28(b). This is realized by a sophisticated cooperative mechanism that combines interstitial segregation (C) with collective host-lattice (bcc Fe) reconstruction at the interface front.

There are three orthogonal interfaces between Fe_3C and the ferrite matrix as shown in Fig. 28(c). Interface II is a coherent twin boundary, thus is naturally energetically favorable. Interface III (which is parallel to the image and not depicted) is also favorable, since a readjustment of the positions of some C atoms leads to energetically more favorable sites at the interface than those in bulk cementite. Atomistic calculations of the interface energies showed that upon Fe_3C growth, the increase in the areas of interfaces II and III will be much easier than that of the energetically more costly interface I. Therefore, preferential growth will occur along the direction perpendicular to interface I, which rationalizes the experimental observation.

Nevertheless, to transform ferrite into cementite, accumulation of C atoms at interface I has to occur at the same time, as the C concentration is initially only a few at. % in the ferrite matrix, while the cementite crystal structure possesses 25 at. % C. By evaluating the MEP of C migration to interface I using NEB calculations (see Sec. III A 2), Wang *et al.*³²⁸ identified a thermodynamic driving force for C

to diffuse from the ferrite matrix to the advancing interface [Fig. 28(c)]. This indicates that the segregation of C atoms to interface I is nearly spontaneous. A collective reconstruction of the bcc ferrite lattice at interface I then occurs by a shear-like shuffle of the Fe atoms along $[111]$ directions [Fig. 28(c)], which cooperatively accommodates the incoming C atoms, realizing the transformation from ferrite to Fe_3C .

This example demonstrates that, when nanoprecipitation occurs, the energetics of the coherent interface between the matrix and precipitate profoundly impacts the morphology of the precipitate. Furthermore, the atomic structure of the interface plays a key role in the compositional adjustment in order to satisfy the chemical composition required for the precipitate. All of these insights prototypically illustrate the importance of the matrix/precipitate interface for nano-scale phase transition kinetics during precipitation.

V. SUMMARY AND OUTLOOK

In this review, we used representative examples to systematically discuss various roles that different types of point and extended defects can play in different types of phase transition kinetics. We were aiming to reflect the broadness of this field and the importance for a wide variety of materials. Through our comprehensive review of the selected examples, we summarize and highlight the following impacts that point, line, and planar defects may have on phase transition kinetics.

- (i) As lattice imperfections, defects (including point, line, and planar defects) may generally serve as heterogeneous nucleation sites and promote nucleation rates by reducing the nucleation barrier within, e.g., a two-step phase transition pathway; in this case an intermediate ordered or disordered phase can be involved. However, such a two-step nucleation mechanism is not always necessary, but depends on the symmetry of the defects and the character of the phase transition (diffusive or diffusionless). Even without an intermediate phase formation, grain boundaries with incoherent facets can help to reduce the nucleation barrier and promote diffusive nucleation kinetics. Similarly, high-symmetry grain-boundary junctions with coherent facets may also promote nucleation in a diffusionless martensitic fashion, as the interface energies are low and interface progression can continuously proceed via well-defined atomic shuffle with the low-energy interfaces maintained. These mechanisms have been identified and verified through both theory and experiment. As a model system, colloidal crystals have enabled very intuitive direct experimental observations of the kinetic processes and mechanisms.
- (ii) Point defects usually suppress martensitic transformations, leading to different transition pathways and/or different phase formation. When the host lattice undergoes a diffusionless martensitic transformation, the point defects do not necessarily follow the displacive lattice transformation; instead, they may locally displace and redistribute to neighboring sites. The presence of point defects generally enhances the martensitic phase transition barrier, suppressing the martensite formation. This is a negative impact if one would like to maximize the martensite formation, as in the case of martensitic steels. However, this suppression of martensite formation could also be turned into a positive outcome. For

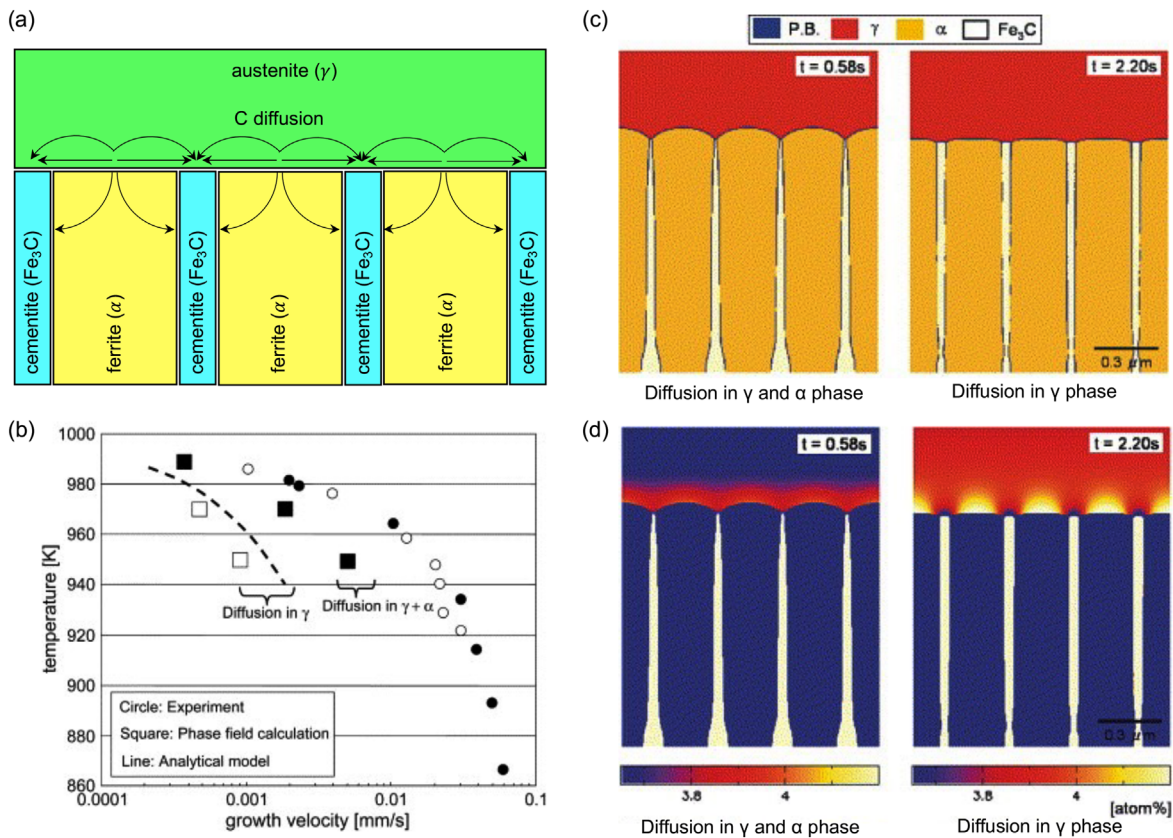


FIG. 25. (a) Possible diffusion paths (the black arrows) for carbon during the pearlite transformation. (b) Dependence of growth velocity on temperature for different diffusion scenarios. (c) Comparison of phase-field-simulated microstructures considering different diffusion paths for carbon. (d) Comparison of phase-field-simulated carbon concentration fields considering different diffusion paths for carbon. Reproduced with permission from Nakajima *et al.*, *Acta Mater.* **54**, 3665 (2006). Copyright 2006 Elsevier.³²¹

instance, impurities block the $\alpha \rightarrow \omega$ transition in Ti alloys, which helps to improve the stability of the favorable, ductile α phase. Similarly, in oxide battery cathodes, vacancies can block unfavorable phase transitions and assist ion migration, which is beneficial for the cycling stability. Furthermore, point defects may lead to the formation of a strain-glass state in ferroelastic systems, which gives rise to novel properties that are absent in conventional martensitic alloys. For the strain-glass formation, in addition to point defects, dislocations and nanoprecipitates can exhibit a similar effect as well.

- (iii) Extended defects, such as dislocations and grain boundaries, contain excess volume, which can act as a trap for alloying elements in the bulk phase. This, in turn, may impact the phase transition kinetics in the bulk. When alloying elements are incorporated into the lattice with the purpose to stabilize certain phases or promote specific phase transitions, segregation of alloying elements to extended defects may act as a competing mechanism against the desired bulk phase transition. Trapped by extended defects, the alloying elements may be in vain and could thus not realize the expected functionalities. This is a general concern for

alloying and doping in a wide spectrum of materials, which should be carefully considered.

- (iv) As a planar defect, grain boundaries themselves can also stabilize some interfacial phases with well-defined structural motifs, which further undergo structural transitions between different grain-boundary phases. Temperature and/or atomic-density (which can be changed through inserting interstitials or vacancies) variations can trigger reversible transitions between different grain-boundary phases. Grain-boundary phase transitions have been directly observed in both MD simulations and *in situ* HRSTEM experiments. In addition to transitions between different ordered phases, grain boundaries can also undergo transitions to nanoscale liquid-like disordered states, even below the bulk melting temperature, which is referred to as grain-boundary premelting. Grain-boundary premelting can drastically reduce the shear resistance of the materials, which ultimately leads to catastrophic materials failure.
- (v) Stacking faults are commonly present in a variety of materials. Since many phase transitions involve slip of atomic layers, stacking faults may naturally impact the kinetics of phase transitions. The discussed examples illustrate that the

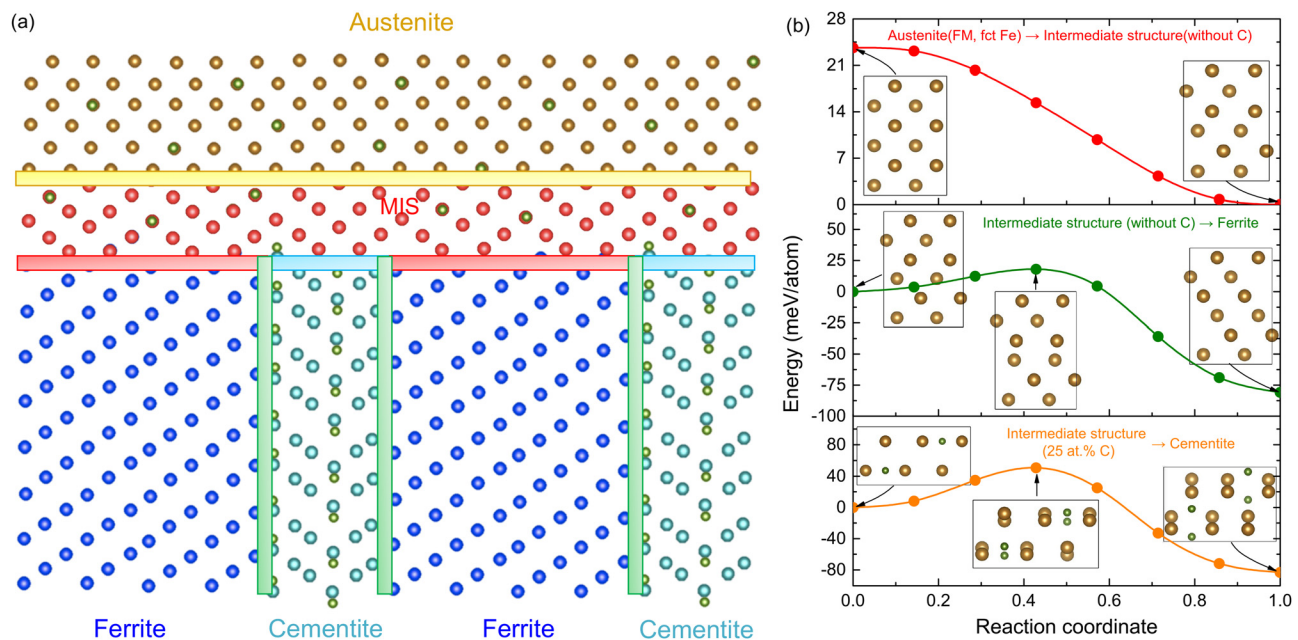


FIG. 26. (a) Schematic illustration of the interfaces during a pearlite transformation (i.e., austenite decomposition into ferrite and cementite) with the metastable intermediate structure (MIS) formed at the interface. (b) Minimum-energy paths for the transformations between austenite, MIS, ferrite and cementite. Zhang *et al.*, *Acta Mater.* **99**, 281 (2015). Reproduced with permission from Copyright 2015 Authors, licensed under a Creative Commons Attribution (CC BY-NC-ND) License.³²⁵

roles that stacking faults can play are bidirectional. Positively, they have the capability to mediate and drive some martensitic transitions in metallic alloys, or serve as intermediate transition steps in layered oxides. On the negative side, stacking faults can also suppress the formation of intermetallic Laves phases. The specific role that stacking faults play in phase transition kinetics needs to be investigated case by case.

- (vi) Surfaces are naturally present in materials and also influence the thermodynamics and kinetics of phase transitions in, most notably, nanomaterials. In liquid droplets, surfaces can affect the maximum undercooling before solidification, since they are the primary source of nucleation sites. In nanomaterials, the total free energy is dominated by contributions from surfaces, which can lead to the formation of new unusual phases that are not observed as bulk phases under ambient conditions; the phase-transition diagram may be remarkably altered while reducing the crystal size. As a defect phase, surfaces themselves might also undergo phase transitions such as reconstructions and chemical ordering, which result in the formation of new defect phases.
- (vii) The lattice mismatches at interfaces can serve as geometric constraints on the product phase, which may lead to the formation of so-called adaptive martensite. The central idea is to utilize nanotwinned modulated martensitic phases to accommodate the interfacial lattice mismatches between the parent and product phases, and thus to minimize the elastic strain energy. This concept has been demonstrated in magnetic shape-memory alloys, where different modulated martensitic phases have been experimentally observed, but their

interpretation was difficult prior to the emergence of the idea of adaptive martensite.

- (viii) When a coherent phase boundary is difficult to achieve, semicoherent or incoherent interfaces can also substantially impact the phase transition kinetics. On the one hand, a disordered interface region may facilitate a collective structural rearrangement while the phase boundary migrates. The phase transition can proceed in a layer-by-layer fashion, as revealed in AKMC and other enhanced sampling techniques. Misfit dislocations at the interfaces may also have a profound impact on the phase transition kinetics. They may pin the lateral flow of interfacial ledges at their core, and only allow the ledges to move when the dislocations themselves have migrated to the new interface location during interfacial transformation. On the other hand, intermediate interfacial phases, termed complexions, may also form, which can act as a buffer zone for the structural transformation and as a channel for fast atomic migration at the interface front.
- (ix) During the formation and growth of nanoprecipitates, the interfaces between the matrix and precipitate also play an important role for the growth kinetics. The matrix-precipitate interfaces impact the thermodynamics and kinetics of phase transitions; for the kinetic aspect, the effects of interfaces are threefold: First, precipitates form different interfaces with the matrix, which also have different interface energies depending on the lattice mismatches and atomic arrangements. The difference in the interface energy may promote preferential growth of the precipitate along certain directions, forming specific morphology.

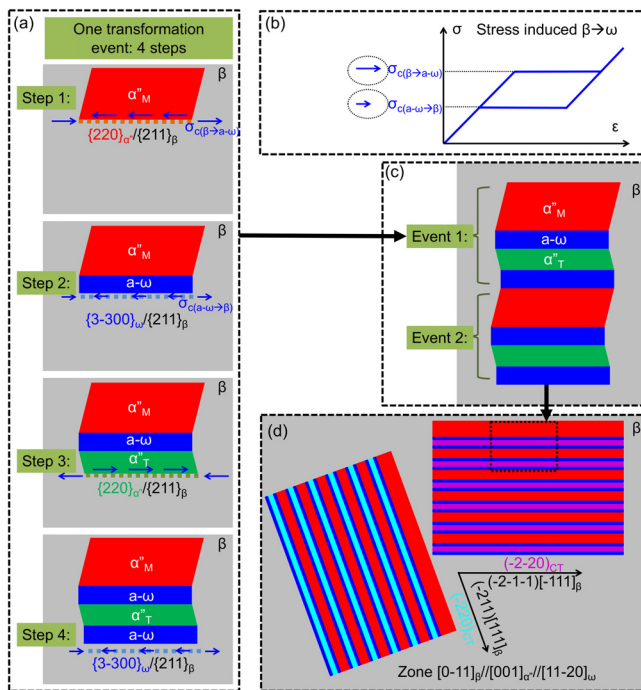


FIG. 27. Schematic illustration of the formation of nanolaminate through the complexion-mediated martensitic phase transformation. (a) Four steps of one event of complexion-mediated martensitic phase transformation. (b) Schematic illustration of stress-strain curve for the stress-induced $\beta \leftrightarrow a-\omega$ transformation. (c) Transformation proceeds by repeating 4 steps in (a). (d) Two blocks of nanocomposite formed in a $[011]_{\beta}$ grain. Reproduced with permission from Zhang *et al.*, Nat. Commun. **8**, 14210 (2017). Copyright 2017 Authors, licensed under a Creative Commons Attribution (CC BY) License.³²⁷

Second, the interface could provide energetically favorable sites for solute segregation, which allows to adjust the local chemical composition that is required for the formation of the precipitate. Third, the interface undergoes atomic shuffles, which need to cooperate with solute segregation in order to transition to the precipitate phase. This is by no means trivial and sophisticated transformation mechanisms are required. The growth kinetics depends sensitively on the transition barrier at the interface.

In addition to the key points summarized above, there certainly could be other types of defect-characterized phase transition kinetics. Both defects and phase transition kinetics have been extensively studied in the literature, but studies of the interplay between defects and phase transition kinetics are still limited. There is an abundance of different aspects that still need to be explored in order to present a systematic and complete physical picture for the various types of defect-characterized phase transition kinetics. We hope this review will help to open up a new chapter for the research in this field. From our current understanding and perspective, we envision the following potential and promising research directions in this growing field.

(i) Currently, the types of defects, phase transitions, and materials that have been carefully researched from the

perspective of defect-characterized phase transition kinetics are relatively limited, which makes it still rather difficult to present a complete physical picture and to derive more general laws and mechanisms. Hence, it would be invaluable to apply the presently available theoretical and experimental techniques to different types of defect-characterized phase transitions in a wider spectrum of materials. This accumulation of data and knowledge is long-lasting, but is extremely helpful for expanding our horizon on the possible roles that defects can play in phase transition kinetics. Presently unknown functions or the unexpected interplay between defects and phase transition kinetics are anticipated to be uncovered; this could also lead to the derivation of general trends and mechanisms.

(ii) From the computational perspective, despite the significant advances in simulation methodology and the profound increase in computing power in recent years, it remains difficult to simulate defect-characterized phase transition kinetics. The challenges lie in overcoming the limited length and time scales in simulations, and in reaching presently unavailable levels of reliability and accuracy. Many advanced techniques for simulating and sampling phase transition pathways in systems with complicated energy landscapes are under developments,^{329–338} which with further improvements are expected to generate large impacts. Density functional theory based first-principles calculations are becoming increasingly more accurate with the emergence of more accurate exchange-correlation functionals^{339–342} and with the theoretical advances, e.g., in capturing finite-temperature effects.^{343–347} The high computational demand is still a critical obstacle for applying first-principles calculations to the studies of phase transition kinetics. Computationally affordable empirical potentials oftentimes suffer from the lack of sufficient accuracy and transferability. Interatomic potentials and force fields based on advanced machine-learning techniques with first-principles training datasets are actively being developed, which may significantly improve the accuracy without being limited to small simulation cells; the transferability is unfortunately still a concern, which may need further investigations and improvements. Hierarchical or coupled multiscale simulations would also be extremely helpful to derive a full understanding of the mechanisms of defect-characterized phase transition kinetics.

(iii) On the experimental side, *in situ* characterizations of phase transition kinetics have become gradually common, but direct observations with atomic resolution and complete chemical information are still rare. Characterizations of defects, in particular point defects, are still extremely challenging. Colloidal crystals often serve as a model system, which allows intuitive observations of the phase transition kinetics and the impacts of defects using video microscopy. However, it is not entirely certain that the mechanisms extracted from these systems can be directly applied to more complex materials. Still, reaching a similar level of accuracy and intuitiveness for the complex microstructure in more “realistic” materials would be desired for electron microscopes, which will also allow direct comparison with

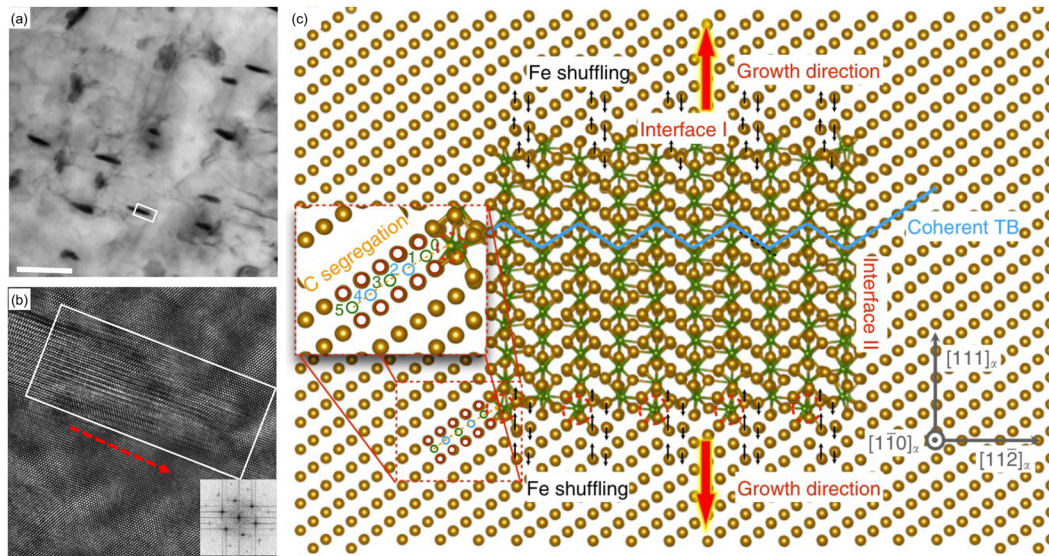


FIG. 28. (a) Needle-shaped Fe₃C precipitates (black) with preferential growth direction in a ferrite matrix (gray). (b) A high-resolution transmission electron microscopy (HRTEM) image of the cementite precipitate in (a) enclosed by a rectangle. (c) Atomic structures of a cementite nanoprecipitate in ferrite matrix. Reproduced with permission from Wang *et al.*, Nat. Commun. 9, 4017 (2018). Copyright 2018 Authors, licensed under a Creative Commons Attribution (CC BY) License.³²⁸

first-principles and atomistic simulation results. Promising studies have already emerged.^{209,348–357} In addition to direct observations, more quantitative analyses of the evolution of the structural and chemical information during phase transitions, and how they can be altered by the presence of defects are of particular interest, but might be very difficult tasks to accomplish. Active developments are still ongoing in order to push the current limits of experimental techniques.

- (iv) Once the diverse roles of defects in phase transition kinetics have been comprehensively established, enormous opportunities for novel research directions in manipulating phase transition kinetics through defect engineering will open up. With the remarkable advances in theoretical modeling and experimental characterization techniques, this approach may even enable new paradigms for the design of a wide spectrum of advanced materials. The performance of materials may be traced back to specific phase transitions and defects, and could then be tailored by changing the chemistry, atomic structure, and/or density of the defects of interest.

ACKNOWLEDGMENTS

This work was supported by the National Natural Science Foundation of China (Grant Nos. 52172136, U1930402, 52171007, 11991060, 12088101, and 52222407). H.W. acknowledges funding by the Deutsche Forschungsgemeinschaft (DFG) through project A1 and A2 of the collaborative research centre under Grant No. SFB/TR 103. H.-Y.L. acknowledges additional financial support from the Chongqing Science and Technology Bureau (Grant Nos. cstc2019cyjqqX0006 and cstc2021ycjh-bgzxm0075). T.H. was supported by the DFG within the project CRC1394 “Structural and

chemical complexity—from defect phases to material properties.” J.R. acknowledges financial support from the DFG through the Heisenberg Programme under Project No. 428315600.

AUTHOR DECLARATIONS

Conflict of Interest

The authors have no conflicts to disclose.

Author Contributions

Xie Zhang: Conceptualization (lead); Funding acquisition (lead); Investigation (lead); Project administration (lead); Supervision (lead); Visualization (lead); Writing – original draft (lead); Writing – review & editing (lead). **Jian Zhang:** Conceptualization (equal); Funding acquisition (equal); Visualization (equal); Writing – original draft (equal); Writing – review & editing (equal). **Hongcai Wang:** Conceptualization (equal); Visualization (equal); Writing – original draft (equal); Writing – review & editing (equal). **Jutta Rogal:** Writing – original draft (equal); Writing – review & editing (equal). **Hong-Yi Li:** Funding acquisition (equal); Supervision (equal); Writing – original draft (equal); Writing – review & editing (equal). **Su-Huai Wei:** Supervision (equal); Writing – review & editing (equal). **Tilmann Hickel:** Funding acquisition (equal); Writing – original draft (equal); Writing – review & editing (equal).

DATA AVAILABILITY

Data sharing is not applicable to this article as no new data were created or analyzed in this study.

REFERENCES

- 1D. L. Goodstein, *States of Matter* (Dover Publications, Mineola, 2002).

- ²D. Lencer, M. Salinga, B. Grabowski, T. Hickel, J. Neugebauer, and M. Wuttig, "A map for phase-change materials," *Nat. Mater.* **7**, 972–977 (2008).
- ³F. Körmann, A. Dick, B. Grabowski, B. Hallstedt, T. Hickel, and J. Neugebauer, "Free energy of bcc iron: Integrated *ab initio* derivation of vibrational, electronic, and magnetic contributions," *Phys. Rev. B* **78**, 033102 (2008).
- ⁴J. L. F. Da Silva, A. Walsh, S.-H. Wei, and H. Lee, "Atomistic origins of the phase transition mechanism in $\text{Ge}_2\text{Sb}_2\text{Te}_5$," *J. Appl. Phys.* **106**, 113509 (2009).
- ⁵L.-F. Huang and J. M. Rondinelli, "Electrochemical phase diagrams for Ti oxides from density functional calculations," *Phys. Rev. B* **92**, 245126 (2015).
- ⁶M. Lai, C. Tasan, J. Zhang, B. Grabowski, L. Huang, and D. Raabe, "Origin of shear induced β to ω transition in Ti–Nb-based alloys," *Acta Mater.* **92**, 55–63 (2015).
- ⁷L.-F. Huang, B. Grabowski, J. Zhang, M.-J. Lai, C. C. Tasan, S. Sandlöbes, D. Raabe, and J. Neugebauer, "From electronic structure to phase diagrams: A bottom-up approach to understand the stability of titanium–transition metal alloys," *Acta Mater.* **113**, 311–319 (2016).
- ⁸T. Chakraborty, J. Rogal, and R. Drautz, "Unraveling the composition dependence of the martensitic transformation temperature: A first-principles study of Ti–Ta alloys," *Phys. Rev. B* **94**, 224104 (2016).
- ⁹W. Wang, A. Janotti, and C. G. Van de Walle, "Phase transformations upon doping in WO_3 ," *J. Chem. Phys.* **146**, 214504 (2017).
- ¹⁰J. Yang, P. Zhang, and S.-H. Wei, "Band structure engineering of $\text{Cs}_2\text{AgBiBr}_6$ perovskite through order-disordered transition: A first-principle study," *J. Phys. Chem. Lett.* **9**, 31–35 (2018).
- ¹¹M. Lai, T. Li, and D. Raabe, " ω phase acts as a switch between dislocation channeling and joint twinning- and transformation-induced plasticity in a metastable β titanium alloy," *Acta Mater.* **151**, 67–77 (2018).
- ¹²A. Ferrari, D. G. Sangiovanni, J. Rogal, and R. Drautz, "First-principles characterization of reversible martensitic transformations," *Phys. Rev. B* **99**, 094107 (2019).
- ¹³X. Cai, H.-X. Deng, and S.-H. Wei, "Carrier-stabilized hexagonal Ge," *Phys. Rev. B* **103**, 245202 (2021).
- ¹⁴Y. Mishin, M. J. Mehl, D. A. Papaconstantopoulos, A. F. Voter, and J. D. Kress, "Structural stability and lattice defects in copper: *Ab initio*, tight-binding, and embedded-atom calculations," *Phys. Rev. B* **63**, 224106 (2001).
- ¹⁵C. Freysoldt, B. Grabowski, T. Hickel, J. Neugebauer, G. Kresse, A. Janotti, and C. G. Van de Walle, "First-principles calculations for point defects in solids," *Rev. Mod. Phys.* **86**, 253–305 (2014).
- ¹⁶J. Rogal, S. V. Divinski, M. W. Finnis, A. Glensk, J. Neugebauer, J. H. Perepezko, S. Schuwalow, M. H. F. Sluiter, and B. Sundman, "Perspectives on point defect thermodynamics: Point defect thermodynamics," *Phys. Status Solidi B* **251**, 97–129 (2014).
- ¹⁷A. Alkauskas, M. D. McCluskey, and C. G. Van de Walle, "Tutorial: Defects in semiconductors—Combining experiment and theory," *J. Appl. Phys.* **119**, 181101 (2016).
- ¹⁸P. Zhang and S.-H. Wei, "Origin of charge compensation and its effect on the stability of oxide cathodes for Li-ion batteries: The case of orthosilicates," *Electrochim. Acta* **270**, 409–416 (2018).
- ¹⁹M. E. Turiansky, A. Alkauskas, L. C. Bassett, and C. G. Van de Walle, "Dangling bonds in hexagonal boron nitride as single-photon emitters," *Phys. Rev. Lett.* **123**, 127401 (2019).
- ²⁰X. Zhang, J.-X. Shen, M. E. Turiansky, and C. G. Van de Walle, "Minimizing hydrogen vacancies to enable highly efficient hybrid perovskites," *Nat. Mater.* **20**, 971–976 (2021).
- ²¹J. Kang, J. Li, and S.-H. Wei, "Atomic-scale understanding on the physics and control of intrinsic point defects in lead halide perovskites," *Appl. Phys. Rev.* **8**, 031302 (2021).
- ²²M. W. Swift and J. L. Lyons, "Deep levels in cesium lead bromide from native defects and hydrogen," *J. Mater. Chem. A* **9**, 7491–7495 (2021).
- ²³M. Allain, "Possible defect-mediated phase transition in a lyotropic liquid crystal. Electron microscopy observations," *Europhys. Lett.* **2**, 597–602 (1986).
- ²⁴A. Janotti and S.-H. Wei, "Epitaxially stabilized AgGaSe_2 for high-efficiency spin-polarized electron source," *J. Phys. Chem. Solids* **64**, 1881–1885 (2003).
- ²⁵J. Dziarmaga, "Dynamics of a quantum phase transition in the random Ising model: Logarithmic dependence of the defect density on the transition rate," *Phys. Rev. B* **74**, 064416 (2006).
- ²⁶J. Howe, R. Pond, and J. Hirth, "The role of disconnections in phase transformations," *Prog. Mater. Sci.* **54**, 792–838 (2009).
- ²⁷J. Zhang, C. Somsen, T. Simon, X. Ding, S. Hou, S. Ren, X. Ren, G. Eggeler, K. Otsuka, and J. Sun, "Leaf-like dislocation substructures and the decrease of martensitic start temperatures: A new explanation for functional fatigue during thermally induced martensitic transformations in coarse-grained Ni-rich Ti–Ni shape memory alloys," *Acta Mater.* **60**, 1999–2006 (2012).
- ²⁸X. Meng, Z. Chen, Z. Chen, F. Wu, S.-S. Li, J. Li, J. Wu, and S.-H. Wei, "Enhancing structural transition by carrier and quantum confinement: Stabilization of cubic InN quantum dots by Mn incorporation," *Appl. Phys. Lett.* **103**, 253102 (2013).
- ²⁹T. Prolov, S. V. Divinski, M. Asta, and Y. Mishin, "Effect of interface phase transformations on diffusion and segregation in high-angle grain boundaries," *Phys. Rev. Lett.* **110**, 255502 (2013).
- ³⁰J. Schmidt, V. Popkov, and A. Schadschneider, "Defect-induced phase transition in the asymmetric simple exclusion process," *Europhys. Lett.* **110**, 20008 (2015).
- ³¹W. Wang, A. Janotti, and C. G. Van de Walle, "Role of oxygen vacancies in crystalline WO_3 ," *J. Mater. Chem. C* **4**, 6641–6648 (2016).
- ³²X. Ou, J. Sietsma, and M. J. Santofimia, "Molecular dynamics simulations of the mechanisms controlling the propagation of bcc/fcc semi-coherent interfaces in iron," *Modell. Simul. Mater. Sci. Eng.* **24**, 055019 (2016).
- ³³H.-S. Kim, J. B. Cook, H. Lin, J. S. Ko, S. H. Tolbert, V. Ozolins, and B. Dunn, "Oxygen vacancies enhance pseudocapacitive charge storage properties of MoO_{3-x} ," *Nat. Mater.* **16**, 454–460 (2017).
- ³⁴A. Dobrovolsky, A. Merdasa, E. L. Unger, A. Yartsev, and I. G. Scheblykin, "Defect-induced local variation of crystal phase transition temperature in metal-halide perovskites," *Nat Commun.* **8**, 34 (2017).
- ³⁵X. Zhang, T. Hickel, J. Rogal, and J. Neugebauer, "Origin of structural modulations in ultrathin Fe films on $\text{Cu}(001)$," *Phys. Rev. Lett.* **118**, 236101 (2017).
- ³⁶Q. Liang, D. Wang, J. Zhang, Y. Ji, X. Ding, Y. Wang, X. Ren, and Y. Wang, "Novel B19' strain glass with large recoverable strain," *Phys. Rev. Mater.* **1**, 033608 (2017).
- ³⁷W. Guo, Y. Meng, X. Zhang, V. Bedekar, H. Bei, S. Hyde, Q. Guo, G. B. Thompson, R. Shivpuri, J.-m. Zuo, and J. D. Poplawsky, "Extremely hard amorphous-crystalline hybrid steel surface produced by deformation induced cementite amorphization," *Acta Mater.* **152**, 107–118 (2018).
- ³⁸I. Unzueta, D. A. de R-Lorente, E. Cesari, V. Sánchez-Alarcos, V. Recarte, J. I. Pérez-Landazábal, J. A. García, and F. Plazaola, "Experimental Observation of vacancy-assisted martensitic transformation shift in Ni–Fe–Ga alloys," *Phys. Rev. Lett.* **122**, 165701 (2019).
- ³⁹J.-P. Ma, J. Yin, Y.-M. Chen, Q. Zhao, Y. Zhou, H. Li, Y. Kuroiwa, C. Moriyoshi, Z.-Y. Li, O. M. Bakr, O. F. Mohammed, and H.-T. Sun, "Defect-triggered phase transition in cesium lead halide perovskite nanocrystals," *ACS Mater. Lett.* **1**, 185–191 (2019).
- ⁴⁰H. Wang, Y. Li, E. Detemple, and G. Eggeler, "Revealing the two-step nucleation and growth mechanism of vanadium carbonitrides in microalloyed steels," *Scr. Mater.* **187**, 350–354 (2020).
- ⁴¹J. Zhang, T. Chen, W. Li, J. Bednarcik, and A.-C. Dippel, "High temperature superelasticity realized in equiatomic Ti–Ni conventional shape memory alloy by severe cold rolling," *Mater. Des.* **193**, 108875 (2020).
- ⁴²Y. Yang, P. Zhang, and S.-H. Wei, "Chemical trends of cation-vacancy-induced d^0 ferromagnetism in dilute zinc chalcogenides," *J. Phys. D: Appl. Phys.* **54**, 375001 (2021).
- ⁴³C. Xiong, Y. Li, J. Zhang, Y. Wang, W. Qu, Y. Ji, L. Cui, and X. Ren, "Superelasticity over a wide temperature range in metastable β -Ti shape memory alloys," *J. Alloys Compd.* **853**, 157090 (2021).
- ⁴⁴Z. Zhang, W. Liu, B. Zhang, B. Sateesh, L. Yuan, D. Zhu, P. Guan, S. J. Pennycook, and J. Guo, "Defect-nucleated phase transition in atomically-thin WS_2 ," *2D Mater.* **8**, 025017 (2021).
- ⁴⁵P. Li, R. Jiang, L. Zhao, H. Peng, P. Zhao, S. Jia, H. Zheng, and J. Wang, "Cation defect mediated phase transition in potassium tungsten bronze," *Inorg. Chem.* **60**, 18199–18204 (2021).

- ⁴⁶Z. Yin, J. Leng, C. Zhao, J. Liu, B. Wu, and S. Jin, "Defect-Induced inhomogeneous phase transition in 2D perovskite single crystals at low temperatures," *ACS Omega* **6**, 35427–35432 (2021).
- ⁴⁷X. Ou, J. Sietsma, and M. J. Santofimia, "Fundamental study of nonclassical nucleation mechanisms in iron," *Acta Mater.* **226**, 117655 (2022).
- ⁴⁸J. Rogal and P. G. Bolhuis, "Multiple state transition path sampling," *J. Chem. Phys.* **129**, 224107 (2008).
- ⁴⁹J. S. Kim, T. LaGrange, B. W. Reed, M. L. Taheri, M. R. Armstrong, W. E. King, N. D. Browning, and G. H. Campbell, "Imaging of transient structures using nanosecond *in situ* TEM," *Science* **321**, 1472–1475 (2008).
- ⁵⁰J. Rogal and P. G. Bolhuis, "On the efficiency of biased sampling of the multiple state path ensemble," *J. Chem. Phys.* **133**, 034101 (2010).
- ⁵¹J. Hu, Y. Hong, C. Muratore, M. Su, and A. A. Voevodin, "*In situ* transmission electron microscopy of solid–liquid phase transition of silica encapsulated bismuth nanoparticles," *Nanoscale* **3**, 3700 (2011).
- ⁵²C.-M. Wang, X. Li, Z. Wang, W. Xu, J. Liu, F. Gao, L. Kovarik, J.-G. Zhang, J. Howe, D. J. Burton, Z. Liu, X. Xiao, S. Thevuthasan, and D. R. Baer, "*In situ* TEM investigation of congruent phase transition and structural evolution of nanostructured silicon/carbon anode for lithium ion batteries," *Nano Lett.* **12**, 1624–1632 (2012).
- ⁵³D. Sheppard, P. Xiao, W. Chemelewski, D. D. Johnson, and G. Henkelman, "A generalized solid-state nudged elastic band method," *J. Chem. Phys.* **136**, 74103 (2012).
- ⁵⁴P. Xiao, D. Sheppard, J. Rogal, and G. Henkelman, "Solid-state dimer method for calculating solid-solid phase transitions," *J. Chem. Phys.* **140**, 174104 (2014).
- ⁵⁵A. Ahadi and Q. Sun, "Stress-induced nanoscale phase transition in superelastic NiTi by *in situ* x-ray diffraction," *Acta Mater.* **90**, 272–281 (2015).
- ⁵⁶D. Şopu, J. Rogal, and R. Drautz, "Thermodynamic and kinetic solid–liquid interface properties from transition path sampling," *J. Chem. Phys.* **145**, 244703 (2016).
- ⁵⁷Q. Lu and B. Yildiz, "Voltage-controlled topotactic phase transition in thin-film SrCoO_x monitored by *in situ* x-ray diffraction," *Nano Lett.* **16**, 1186–1193 (2016).
- ⁵⁸P. Kalita, P. Specht, S. Root, N. Sinclair, A. Schuman, M. White, A. L. Cornelius, J. Smith, and S. Sinogeikin, "Direct observations of a dynamically driven phase transition with *in situ* x-ray diffraction in a simple ionic crystal," *Phys. Rev. Lett.* **119**, 255701 (2017).
- ⁵⁹X. Zhang, F. Wang, B.-B. Zhang, G. Zha, and W. Jie, "Ferroelastic domains in a CsPbBr₃ single crystal and their phase transition characteristics: An *in situ* TEM study," *Cryst. Growth Des.* **20**, 4585–4592 (2020).
- ⁶⁰I. Cora, Z. Fogarassy, R. Fornari, M. Bosi, A. Rečnik, and B. Pécz, "*In situ* TEM study of $K \rightarrow \beta$ and $K \rightarrow \gamma$ phase transformations in Ga₂O₃," *Acta Mater.* **183**, 216–227 (2020).
- ⁶¹J. Zhang, Y. Li, and W. Li, "Metastable phase diagram on heating in quenched Ti–Nb high-temperature shape memory alloys," *J. Mater. Sci.* **56**, 11456–11468 (2021).
- ⁶²J. Rogal, "Reaction coordinates in complex systems—a perspective," *Eur. Phys. J. B* **94**, 223 (2021).
- ⁶³S. Korte-Kerzel, T. Hickel, L. Huber, D. Raabe, S. Sandlöbes-Haut, M. Todorova, and J. Neugebauer, "Defect phases—thermodynamics and impact on material properties," *Int. Mater. Rev.* **67**, 89–117 (2022).
- ⁶⁴E. J. Mittemeijer, *Fundamentals of Materials Science: The Microstructure–Property Relationship Using Metals as Model Systems* (Springer, Berlin, Heidelberg, 2020).
- ⁶⁵S. Puri, *Kinetics of Phase Transitions* (CRC Press, Boca Raton, 2009).
- ⁶⁶C. Rao and K. Rao, *Phase Transitions in Solids: An Approach to the Study of the Chemistry and Physics of Solids* (McGraw Hill, Maidenhead, 1978).
- ⁶⁷G. Jaeger, "The Ehrenfest classification of phase transitions: Introduction and evolution," *Arch. Hist. Exact Sci.* **53**, 51–81 (1998).
- ⁶⁸M. Kuzmina, M. Herbig, D. Ponge, S. Sandlöbes, and D. Raabe, "Linear complexes: Confined chemical and structural states at dislocations," *Science* **349**, 1080–1083 (2015).
- ⁶⁹Y. Yang, F. Gao, S. Gao, and S.-H. Wei, "Origin of the stability of two-dimensional perovskites: A first-principles study," *J. Mater. Chem. A* **6**, 14949–14955 (2018).
- ⁷⁰C. J. Humphreys, "Stem imaging of crystals and defects," in *Introduction to Analytical Electron Microscopy*, edited by J. J. Hren, J. I. Goldstein, and D. C. Joy (Springer, Boston, 1979), pp. 305–332.
- ⁷¹D. C. Rapaport, *The Art of Molecular Dynamics Simulation*, 2nd ed. (Cambridge University Press, Cambridge, New York, 2004).
- ⁷²L. Woodcock, "Isothermal molecular dynamics calculations for liquid salts," *Chem. Phys. Lett.* **10**, 257–261 (1971).
- ⁷³H. C. Andersen, "Molecular dynamics simulations at constant pressure and/or temperature," *J. Chem. Phys.* **72**, 2384–2393 (1980).
- ⁷⁴H. J. C. Berendsen, J. P. M. Postma, W. F. van Gunsteren, A. DiNola, and J. R. Haak, "Molecular dynamics with coupling to an external bath," *J. Chem. Phys.* **81**, 3684–3690 (1984).
- ⁷⁵S. Nosé, "A unified formulation of the constant temperature molecular dynamics methods," *J. Chem. Phys.* **81**, 511–519 (1984).
- ⁷⁶W. G. Hoover, "Canonical dynamics: Equilibrium phase-space distributions," *Phys. Rev. A* **31**, 1695–1697 (1985).
- ⁷⁷M. Parrinello and A. Rahman, "Polymorphic transitions in single crystals: A new molecular dynamics method," *J. Appl. Phys.* **52**, 7182–7190 (1981).
- ⁷⁸J. C. Maxwell, "V. Illustrations of the dynamical theory of gases. I. On the motions and collisions of perfectly elastic spheres," *London, Edinburgh, Dublin Philos. Mag. J. Sci.* **19**, 19–32 (1860).
- ⁷⁹L. Boltzmann, "Weitere studien über das wärme-gleichgewicht unter gasmolekülen," in *Kinetische Theorie II* (Vieweg+Teubner Verlag, Wiesbaden, 1970), pp. 115–225.
- ⁸⁰J. E. Jones, "On the determination of molecular fields. I. From the variation of the viscosity of a gas with temperature," *Proc. R. Soc. Lond. A* **106**, 441–462 (1924).
- ⁸¹J. E. Jones, "On the determination of molecular fields. II. From the equation of state of a gas," *Proc. R. Soc. London A* **106**, 463–477 (1924).
- ⁸²J. E. Lennard-Jones, "Cohesion," *Proc. Phys. Soc.* **43**, 461–482 (1931).
- ⁸³F. H. Stillinger and T. A. Weber, "Computer simulation of local order in condensed phases of silicon," *Phys. Rev. B* **31**, 5262–5271 (1985).
- ⁸⁴M. S. Daw and M. I. Baskes, "Embedded-atom method: Derivation and application to impurities, surfaces, and other defects in metals," *Phys. Rev. B* **29**, 6443–6453 (1984).
- ⁸⁵G. Kresse and J. Hafner, "*Ab initio* molecular dynamics for liquid metals," *Phys. Rev. B* **47**, 558–561 (1993).
- ⁸⁶M. E. Tuckerman, "*Ab initio* molecular dynamics: Basic concepts, current trends and novel applications," *J. Phys.: Condens. Matter* **14**, R1297–R1355 (2002).
- ⁸⁷D. Marx and J. Hutter, *Ab Initio Molecular Dynamics: Basic Theory and Advanced Methods* (Cambridge University Press, 2009).
- ⁸⁸J. Behler and G. Csányi, "Machine learning potentials for extended systems: A perspective," *Eur. Phys. J. B* **94**, 142 (2021).
- ⁸⁹T. Wen, L. Zhang, H. Wang, W. E, and D. J. Srolovitz, "Deep potentials for materials science," *Mater. Futures* **1**, 022601 (2022).
- ⁹⁰B. Grabowski, Y. Ikeda, P. Srinivasan, F. Körmann, C. Freysoldt, A. I. Duff, A. Shapeev, and J. Neugebauer, "*Ab initio* vibrational free energies including anharmonicity for multicomponent alloys," *npj Comput. Mater.* **5**, 80 (2019).
- ⁹¹T. Kostiuhenko, F. Körmann, J. Neugebauer, and A. Shapeev, "Impact of lattice relaxations on phase transitions in a high-entropy alloy studied by machine-learning potentials," *npj Comput. Mater.* **5**, 55 (2019).
- ⁹²T. Kostiuhenko, A. V. Ruban, J. Neugebauer, A. Shapeev, and F. Körmann, "Short-range order in face-centered cubic VCoNi alloys," *Phys. Rev. Mater.* **4**, 113802 (2020).
- ⁹³A. F. Voter, "Hyperdynamics: Accelerated molecular dynamics of infrequent events," *Phys. Rev. Lett.* **78**, 3908–3911 (1997).
- ⁹⁴A. F. Voter, "Parallel replica method for dynamics of infrequent events," *Phys. Rev. B* **57**, R13985–R13988 (1998).
- ⁹⁵M. R. So/rensen and A. F. Voter, "Temperature-accelerated dynamics for simulation of infrequent events," *J. Chem. Phys.* **112**, 9599–9606 (2000).
- ⁹⁶A. Laio and M. Parrinello, "Escaping free-energy minima," *Proc. Natl. Acad. Sci. U. S. A.* **99**, 12562–12566 (2002).
- ⁹⁷A. Laio and F. L. Gervasio, "Metadynamics: A method to simulate rare events and reconstruct the free energy in biophysics, chemistry and material science," *Rep. Prog. Phys.* **71**, 126601 (2008).
- ⁹⁸A. Barducci, M. Bonomi, and M. Parrinello, "Metadynamics," *WIREs Comput. Mol. Sci.* **1**, 826–843 (2011).
- ⁹⁹L. Rosso and M. E. Tuckerman, "An adiabatic molecular dynamics method for the calculation of free energy profiles," *Mol. Simul.* **28**, 91–112 (2002).

- ¹⁰⁰L. Rosso, P. Mináry, Z. Zhu, and M. E. Tuckerman, "On the use of the adiabatic molecular dynamics technique in the calculation of free energy profiles," *J. Chem. Phys.* **116**, 4389–4402 (2002).
- ¹⁰¹J. B. Abrams and M. E. Tuckerman, "Efficient and direct generation of multidimensional free energy surfaces via adiabatic dynamics without coordinate transformations," *J. Phys. Chem. B* **112**, 15742–15757 (2008).
- ¹⁰²C. Dellago, P. G. Bolhuis, and D. Chandler, "Efficient transition path sampling: Application to Lennard–Jones cluster rearrangements," *J. Chem. Phys.* **108**, 9236–9245 (1998).
- ¹⁰³C. Dellago, P. G. Bolhuis, F. S. Csajka, and D. Chandler, "Transition path sampling and the calculation of rate constants," *J. Chem. Phys.* **108**, 1964–1977 (1998).
- ¹⁰⁴R. J. Allen, D. Frenkel, and P. R. ten Wolde, "Simulating rare events in equilibrium or nonequilibrium stochastic systems," *J. Chem. Phys.* **124**, 024102 (2006).
- ¹⁰⁵R. J. Allen, D. Frenkel, and P. R. ten Wolde, "Forward flux sampling-type schemes for simulating rare events: Efficiency analysis," *J. Chem. Phys.* **124**, 194111 (2006).
- ¹⁰⁶P. G. Bolhuis and C. Dellago, "Trajectory-Based rare event simulation," in *Reviews in Computational Chemistry*, edited by K. B. Lipkowitz (John Wiley & Sons, Inc., Hoboken, 2010), pp. 111–210.
- ¹⁰⁷B. Peters, "Recent advances in transition path sampling: Accurate reaction coordinates, likelihood maximisation and diffusive barrier-crossing dynamics," *Mol. Simul.* **36**, 1265–1281 (2010).
- ¹⁰⁸P. G. Bolhuis and D. W. H. Swenson, "Transition path sampling as Markov chain Monte Carlo of trajectories: Recent algorithms, software, applications, and future outlook," *Adv. Theory Simul.* **4**, 2000237 (2021).
- ¹⁰⁹G. Henkelman, G. Jóhannesson, and H. Jónsson, "Methods for finding saddle points and minimum energy paths," in *Theoretical Methods in Condensed Phase Chemistry*, edited by S. D. Schwartz (Kluwer Academic Publishers, Dordrecht, 2002), Vol. 5, pp. 269–302.
- ¹¹⁰D. Sheppard, R. Terrell, and G. Henkelman, "Optimization methods for finding minimum energy paths," *J. Chem. Phys.* **128**, 134106 (2008).
- ¹¹¹G. Henkelman, B. P. Uberuaga, H. Jónsson, and H. Jónsson, "Climbing image nudged elastic band method for finding saddle points and minimum energy paths," *J. Chem. Phys.* **113**, 9901–9904 (2000).
- ¹¹²T. Hickel, B. Grabowski, F. Körmann, and J. Neugebauer, "Advancing density functional theory to finite temperatures: Methods and applications in steel design," *J. Phys. Condens. Matter* **24**, 053202 (2012).
- ¹¹³L. Sandoval, H. M. Urbassek, and P. Entel, "The Bain versus Nishiyama–Wassermann path in the martensitic transformation of Fe," *New J. Phys.* **11**, 103027 (2009).
- ¹¹⁴K. Wang, S.-L. Shang, Y. Wang, Z.-K. Liu, and F. Liu, "Martensitic transition in Fe via Bain path at finite temperatures: A comprehensive first-principles study," *Acta Mater.* **147**, 261–276 (2018).
- ¹¹⁵H. Hu, Z. Lu, and W. Yang, "QM/MM minimum free-energy path: Methodology and application to triosephosphate isomerase," *J. Chem. Theory Comput.* **3**, 390–406 (2007).
- ¹¹⁶A. Bortz, M. Kalos, and J. Lebowitz, "A new algorithm for Monte Carlo simulation of Ising spin systems," *J. Comput. Phys.* **17**, 10–18 (1975).
- ¹¹⁷D. T. Gillespie, "A general method for numerically simulating the stochastic time evolution of coupled chemical reactions," *J. Comput. Phys.* **22**, 403–434 (1976).
- ¹¹⁸K. A. Fichtorn and W. H. Weinberg, "Theoretical foundations of dynamical Monte Carlo simulations," *J. Chem. Phys.* **95**, 1090–1096 (1991).
- ¹¹⁹A. F. Voter, "Introduction to the kinetic Monte Carlo method," in *Radiation Effects in Solids*, edited by K. E. Sickafus, E. A. Kotomin, and B. P. Uberuaga (Springer, Netherlands, Dordrecht, 2007), Vol. 235, pp. 1–23.
- ¹²⁰G. H. Vineyard, "Frequency factors and isotope effects in solid state rate processes," *J. Phys. Chem. Solids* **3**, 121–127 (1957).
- ¹²¹G. Henkelman and H. Jónsson, "Long time scale kinetic Monte Carlo simulations without lattice approximation and predefined event table," *J. Chem. Phys.* **115**, 9657–9666 (2001).
- ¹²²L. Xu and G. Henkelman, "Adaptive kinetic Monte Carlo for first-principles accelerated dynamics," *J. Chem. Phys.* **129**, 114104 (2008).
- ¹²³F. El-Mellouhi, N. Mousseau, and L. J. Lewis, "Kinetic activation-relaxation technique: An off-lattice self-learning kinetic Monte Carlo algorithm," *Phys. Rev. B* **78**, 153202 (2008).
- ¹²⁴L. K. Béland, P. Brommer, F. El-Mellouhi, J.-F. Joly, and N. Mousseau, "Kinetic activation-relaxation technique," *Phys. Rev. E* **84**, 046704 (2011).
- ¹²⁵G. Henkelman and H. Jónsson, "A dimer method for finding saddle points on high dimensional potential surfaces using only first derivatives," *J. Chem. Phys.* **111**, 7010–7022 (1999).
- ¹²⁶S. T. Chill and G. Henkelman, "Molecular dynamics saddle search adaptive kinetic Monte Carlo," *J. Chem. Phys.* **140**, 214110 (2014).
- ¹²⁷N. Moelans, B. Blanpain, and P. Wollants, "An introduction to phase-field modeling of microstructure evolution," *Calphad* **32**, 268–294 (2008).
- ¹²⁸A. G. Khachaturyan, *Theory of Structural Transformations in Solids* (Wiley, New York, 1983).
- ¹²⁹L.-Q. Chen, "Phase-field models for microstructure evolution," *Annu. Rev. Mater. Res.* **32**, 113–140 (2002).
- ¹³⁰Y. Wang, L.-Q. Chen, and A. Khachaturyan, "Kinetics of strain-induced morphological transformation in cubic alloys with a miscibility gap," *Acta Metall. Mater.* **41**, 279–296 (1993).
- ¹³¹Y. Wang and A. Khachaturyan, "Three-dimensional field model and computer modeling of martensitic transformations," *Acta Mater.* **45**, 759–773 (1997).
- ¹³²A. Artemev, Y. Jin, and A. Khachaturyan, "Three-dimensional phase field model of proper martensitic transformation," *Acta Mater.* **49**, 1165–1177 (2001).
- ¹³³Y. Wang, D. Banerjee, C. Su, and A. Khachaturyan, "Field kinetic model and computer simulation of precipitation of L12 ordered intermetallics from f.c.c. solid solution," *Acta Mater.* **46**, 2983–3001 (1998).
- ¹³⁴D. Li and L. Chen, "Shape evolution and splitting of coherent particles under applied stresses," *Acta Mater.* **47**, 247–257 (1998).
- ¹³⁵Y. L. Li, S. Y. Hu, Z. K. Liu, and L. Q. Chen, "Phase-field model of domain structures in ferroelectric thin films," *Appl. Phys. Lett.* **78**, 3878–3880 (2001).
- ¹³⁶S. Choudhury, Y. Li, C. Krilliii, and L. Chen, "Phase-field simulation of polarization switching and domain evolution in ferroelectric polycrystals," *Acta Mater.* **53**, 5313–5321 (2005).
- ¹³⁷J. Zhang and L. Chen, "Phase-field microelasticity theory and micromagnetic simulations of domain structures in giant magnetostrictive materials," *Acta Mater.* **53**, 2845–2855 (2005).
- ¹³⁸M. Ode, S. G. Kim, and T. Suzuki, "Recent advances in the phase-field model for solidification," *ISIJ Int.* **41**, 1076–1082 (2001).
- ¹³⁹W. J. Boettinger, J. A. Warren, C. Beckermann, and A. Karma, "Phase-field simulation of solidification," *Annu. Rev. Mater. Res.* **32**, 163–194 (2002).
- ¹⁴⁰A. A. Wheeler, W. J. Boettinger, and G. B. McFadden, "Phase-field model for isothermal phase transitions in binary alloys," *Phys. Rev. A* **45**, 7424–7439 (1992).
- ¹⁴¹S. G. Kim, W. T. Kim, and T. Suzuki, "Phase-field model for binary alloys," *Phys. Rev. E* **60**, 7186–7197 (1999).
- ¹⁴²I. Steinbach, F. Pezzolla, B. Nestler, M. Seefelberg, R. Prieler, G. Schmitz, and J. Rezende, "A phase field concept for multiphase systems," *Phys. Nonlinear Phenom.* **94**, 135–147 (1996).
- ¹⁴³I. Steinbach, L. Zhang, and M. Plapp, "Phase-field model with finite interface dissipation," *Acta Mater.* **60**, 2689–2701 (2012).
- ¹⁴⁴L. Zhang and I. Steinbach, "Phase-field model with finite interface dissipation: Extension to multi-component multi-phase alloys," *Acta Mater.* **60**, 2702–2710 (2012).
- ¹⁴⁵K. R. Elder, M. Katakowski, M. Haataja, and M. Grant, "Modeling elasticity in crystal growth," *Phys. Rev. Lett.* **88**, 245701 (2002).
- ¹⁴⁶K. R. Elder and M. Grant, "Modeling elastic and plastic deformations in nonequilibrium processing using phase field crystals," *Phys. Rev. E* **70**, 051605 (2004).
- ¹⁴⁷A. Adland, A. Karma, R. Spatschek, D. Buta, and M. Asta, "Phase-field-crystal study of grain boundary premelting and shearing in bcc iron," *Phys. Rev. B* **87**, 024110 (2013).
- ¹⁴⁸C. Hüter, J. Neugebauer, G. Boussinot, B. Svendsen, U. Prahl, and R. Spatschek, "Modelling of grain boundary dynamics using amplitude equations," *Continuum Mech. Thermodyn.* **29**, 895–911 (2017).
- ¹⁴⁹R. Spatschek and A. Karma, "Amplitude equations for polycrystalline materials with interaction between composition and stress," *Phys. Rev. B* **81**, 214201 (2010).
- ¹⁵⁰M. Torabi Rad, G. Boussinot, and M. Apel, "Dynamics of grain boundary premelting," *Sci. Rep.* **10**, 21074 (2020).
- ¹⁵¹C. Guo, J. Wang, J. Li, Z. Wang, Y. Huang, J. Gu, and X. Lin, "Coupling eutectic nucleation mechanism investigated by phase field crystal model," *Acta Mater.* **145**, 175–185 (2018).

- ¹⁵²Z.-F. Huang and K. R. Elder, "Mesoscopic and microscopic modeling of island formation in strained film epitaxy," *Phys. Rev. Lett.* **101**, 158701 (2008).
- ¹⁵³K.-A. Wu and P. W. Voorhees, "Stress-induced morphological instabilities at the nanoscale examined using the phase field crystal approach," *Phys. Rev. B* **80**, 125408 (2009).
- ¹⁵⁴Y. Tao, C. Zheng, Z. Jing, D. Weiping, and W. Lin, "Phase field crystal study on the temporal evolution and coarsening mechanism of precipitates during spinodal decomposition," *Rare Met. Mater. Eng.* **42**, 1773–1778 (2013).
- ¹⁵⁵K. A. Moats, E. Asadi, and M. Laradji, "Phase field crystal simulations of the kinetics of Ostwald ripening in two dimensions," *Phys. Rev. E* **99**, 012803 (2019).
- ¹⁵⁶W. H. Bragg, "The nature of γ and x-rays," *Nature* **77**, 270–271 (1908).
- ¹⁵⁷W. H. Bragg and W. L. Bragg, "The reflection of x-rays by crystals," *Proc. R. Soc. London A* **88**, 428–438 (1913).
- ¹⁵⁸W. Friedrich, P. Knipping, and M. Laue, "Interferenzerscheinungen bei Röntgenstrahlen," *Ann. Phys.* **346**, 971–988 (1913).
- ¹⁵⁹H. M. Rietveld, "A profile refinement method for nuclear and magnetic structures," *J. Appl. Crystallogr.* **2**, 65–71 (1969).
- ¹⁶⁰J. Li and J. Gong, "Operando characterization techniques for electrocatalysis," *Energy Environ. Sci.* **13**, 3748–3779 (2020).
- ¹⁶¹M. Hayat, *Basic Techniques for Transmission Electron Microscopy* (Elsevier Science, Saint Louis, 2014).
- ¹⁶²J. C. Crocker and D. G. Grier, "Methods of digital video microscopy for colloidal studies," *J. Colloid Interface Sci.* **179**, 298–310 (1996).
- ¹⁶³P. Habdas and E. R. Weeks, "Video microscopy of colloidal suspensions and colloidal crystals," *Curr. Opin. Colloid Interface Sci.* **7**, 196–203 (2002).
- ¹⁶⁴K. Zahn, R. Lenke, and G. Maret, "Two-stage melting of paramagnetic colloidal crystals in two dimensions," *Phys. Rev. Lett.* **82**, 2721–2724 (1999).
- ¹⁶⁵A. van Blaaderen, R. Ruel, and P. Wiltzius, "Template-directed colloidal crystallization," *Nature* **385**, 321–324 (1997).
- ¹⁶⁶H. M. Lindsay and P. M. Chaikin, "Elastic properties of colloidal crystals and glasses," *J. Chem. Phys.* **76**, 3774–3781 (1982).
- ¹⁶⁷V. J. Anderson and H. N. W. Lekkerkerker, "Insights into phase transition kinetics from colloid science," *Nature* **416**, 811–815 (2002).
- ¹⁶⁸B. Li, D. Zhou, and Y. Han, "Assembly and phase transitions of colloidal crystals," *Nat. Rev. Mater.* **1**, 15011 (2016).
- ¹⁶⁹L. Li, C. Goodrich, H. Yang, K. R. Phillips, Z. Jia, H. Chen, L. Wang, J. Zhong, A. Liu, J. Lu, J. Shuai, M. P. Brenner, F. Spaepen, and J. Aizenberg, "Microscopic origins of the crystallographically preferred growth in evaporation-induced colloidal crystals," *Proc. Natl. Acad. Sci. U. S. A.* **118**, e2107588118 (2021).
- ¹⁷⁰Y. Peng, F. Wang, Z. Wang, A. M. Alsayed, Z. Zhang, A. G. Yodh, and Y. Han, "Two-step nucleation mechanism in solid–solid phase transitions," *Nat. Mater.* **14**, 101–108 (2015).
- ¹⁷¹Y. Peng, W. Li, F. Wang, T. Still, A. G. Yodh, and Y. Han, "Diffusive and martensitic nucleation kinetics in solid–solid transitions of colloidal crystals," *Nat. Commun.* **8**, 14978 (2017).
- ¹⁷²M. Schmidt and H. Löwen, "Freezing between two and three dimensions," *Phys. Rev. Lett.* **76**, 4552–4555 (1996).
- ¹⁷³A. Fortini and M. Dijkstra, "Phase behaviour of hard spheres confined between parallel hard plates: Manipulation of colloidal crystal structures by confinement," *J. Phys.: Condens. Matter* **18**, L371–L378 (2006).
- ¹⁷⁴J. N. Shapiro, "Lindemann law and lattice dynamics," *Phys. Rev. B* **1**, 3982–3989 (1970).
- ¹⁷⁵M. Avrami, "Kinetics of phase change. I General theory," *J. Chem. Phys.* **7**, 1103–1112 (1939).
- ¹⁷⁶M. Avrami, "Kinetics of phase change. II. Transformation-time relations for random distribution of nuclei," *J. Chem. Phys.* **8**, 212–224 (1940).
- ¹⁷⁷M. Avrami, "Granulation, phase change, and microstructure kinetics of phase change. III," *J. Chem. Phys.* **9**, 177–184 (1941).
- ¹⁷⁸X. Zhang, T. Hickel, J. Rogal, and J. Neugebauer, "Interplay between interstitial displacement and displacive lattice transformations," *Phys. Rev. B* **94**, 104109 (2016).
- ¹⁷⁹E. C. Bain and N. Y. Dunkirk, "The nature of martensite," *Trans. AIME* **79**, 25–46 (1924).
- ¹⁸⁰G. Kurdjumov and G. Sachs, "Ueber den Mechanismus der Stahlhärtung," *Z. Phys.* **64**, 325–343 (1930).
- ¹⁸¹O. D. Sherby, J. Wadsworth, D. R. Lesuer, and C. K. Syn, "Revisiting the structure of martensite in iron-carbon steels," *Mater. Trans.* **49**, 2016–2027 (2008).
- ¹⁸²G. Kurdjumov and A. Khachaturyan, "Nature of axial ratio anomalies of the martensite lattice and mechanism of diffusionless $\gamma \rightarrow \alpha$ transformation," *Acta Metall.* **23**, 1077–1088 (1975).
- ¹⁸³L. Bourgeois, Y. Zhang, Z. Zhang, Y. Chen, and N. V. Medhekar, "Transforming solid-state precipitates via excess vacancies," *Nat. Commun.* **11**, 1248 (2020).
- ¹⁸⁴K. C. Russell, "The role of excess vacancies in precipitation," *Scr. Metall.* **3**, 313–316 (1969).
- ¹⁸⁵P. E. Marth, H. I. Aaronson, G. W. Lorimer, T. L. Bartel, and K. C. Russell, "Application of heterogeneous nucleation theory to precipitate nucleation at GP zones," *Metall. Trans. A* **7**, 1519–1528 (1976).
- ¹⁸⁶K. Shimokawa, T. Atsumi, N. L. Okamoto, T. Kawaguchi, S. Imashuku, K. Wagatsuma, M. Nakayama, K. Kanamura, and T. Ichitsubo, "Structure design of long-life spinel-oxide cathode materials for magnesium rechargeable batteries," *Adv. Mater.* **33**, 2007539 (2021).
- ¹⁸⁷J. Zhang, Y. Wang, X. Ding, Z. Zhang, Y. Zhou, X. Ren, D. Wang, Y. Ji, M. Song, K. Otsuka, and J. Sun, "Spontaneous strain glass to martensite transition in a $\text{Ti}_{50}\text{Ni}_{44.5}\text{Fe}_{5.5}$ strain glass," *Phys. Rev. B* **84**, 214201 (2011).
- ¹⁸⁸D. Wang, Y. Wang, Z. Zhang, and X. Ren, "Modeling Abnormal strain states in ferroelastic systems: The role of point defects," *Phys. Rev. Lett.* **105**, 205702 (2010).
- ¹⁸⁹P. Lloveras, T. Castán, M. Porta, A. Planes, and A. Saxena, "Influence of elastic anisotropy on structural nanoscale textures," *Phys. Rev. Lett.* **100**, 165707 (2008).
- ¹⁹⁰P. Lloveras, T. Castán, M. Porta, A. Planes, and A. Saxena, "Glassy behavior in martensites: Interplay between elastic anisotropy and disorder in zero-field-cooling/field-cooling simulation experiments," *Phys. Rev. B* **80**, 054107 (2009).
- ¹⁹¹A. Jayaraman, W. Klement, and G. C. Kennedy, "Solid-solid transitions in titanium and zirconium at high pressures," *Phys. Rev.* **131**, 644–649 (1963).
- ¹⁹²Y. Vohra, S. Sikka, S. Vaidya, and R. Chidambaram, "Impurity effects and reaction kinetics of the pressure-induced $\alpha \rightarrow \omega$ transformation in Ti," *J. Phys. Chem. Solids* **38**, 1293–1296 (1977).
- ¹⁹³C. W. Greeff, D. R. Trinkle, and R. C. Albers, "Shock-induced α - ω transition in titanium," *J. Appl. Phys.* **90**, 2221–2226 (2001).
- ¹⁹⁴R. G. Hennig, D. R. Trinkle, J. Bouchet, S. G. Srinivasan, R. C. Albers, and J. W. Wilkins, "Impurities block the alpha to omega martensitic transformation in titanium," *Nat. Mater.* **4**, 129–133 (2005).
- ¹⁹⁵X. Zhang, H. Wang, T. Hickel, J. Rogal, Y. Li, and J. Neugebauer, "Mechanism of collective interstitial ordering in Fe–C alloys," *Nat. Mater.* **19**, 849–854 (2020).
- ¹⁹⁶Y. Vohra, "Electronic basis for omega phase stability in group IV transition metals and alloys," *Acta Metall.* **27**, 1671–1675 (1979).
- ¹⁹⁷J. Zhang, D. Xue, X. Cai, X. Ding, X. Ren, and J. Sun, "Dislocation induced strain glass in $\text{Ti}_{50}\text{Ni}_{45}\text{Fe}_5$ alloy," *Acta Mater.* **120**, 130–137 (2016).
- ¹⁹⁸C. Zener, "Theory of strain interaction of solute atoms," *Phys. Rev.* **74**, 639–647 (1948).
- ¹⁹⁹A. Udyansky, J. von Pezold, A. Dick, and J. Neugebauer, "Orientational ordering of interstitial atoms and martensite formation in dilute Fe-based solid solutions," *Phys. Rev. B* **83**, 184112 (2011).
- ²⁰⁰R. Naraghi, M. Selleby, and J. Ågren, "Thermodynamics of stable and metastable structures in Fe–C system," *Calphad* **46**, 148–158 (2014).
- ²⁰¹A. V. Ruban, "Self-trapping of carbon atoms in α -Fe during the martensitic transformation: A qualitative picture from *ab initio* calculations," *Phys. Rev. B* **90**, 144106 (2014).
- ²⁰²Y. Ji, X. Ding, T. Lookman, K. Otsuka, and X. Ren, "Heterogeneities and strain glass behavior: Role of nanoscale precipitates in low-temperature-aged $\text{Ti}_{48.7}\text{Ni}_{51.3}$ alloys," *Phys. Rev. B* **87**, 104110 (2013).
- ²⁰³Z. Zhou, J. Cui, and X. Ren, "Strain glass state as the boundary of two phase transitions," *Sci. Rep.* **5**, 13377 (2015).
- ²⁰⁴P. R. Cantwell, M. Tang, S. J. Dillon, J. Luo, G. S. Rohrer, and M. P. Harmer, "Grain boundary complexions," *Acta Mater.* **62**, 1–48 (2014).
- ²⁰⁵P. R. Cantwell, T. Frolov, T. J. Rupert, A. R. Krause, C. J. Marvel, G. S. Rohrer, J. M. Rickman, and M. P. Harmer, "Grain boundary complexion transitions," *Annu. Rev. Mater. Res.* **50**, 465–492 (2020).

- ²⁰⁶T. Frolov, D. L. Olmsted, M. Asta, and Y. Mishin, "Structural phase transformations in metallic grain boundaries," *Nat. Commun.* **4**, 1899 (2013).
- ²⁰⁷S. J. Fensin, D. Olmsted, D. Buta, M. Asta, A. Karma, and J. J. Hoyt, "Structural disjoining potential for grain-boundary premelting and grain coalescence from molecular-dynamics simulations," *Phys. Rev. E* **81**, 031601 (2010).
- ²⁰⁸J. Berry, K. R. Elder, and M. Grant, "Melting at dislocations and grain boundaries: A phase field crystal study," *Phys. Rev. B* **77**, 224114 (2008).
- ²⁰⁹T. Meiners, T. Frolov, R. E. Rudd, G. Dehm, and C. H. Liebscher, "Observations of grain-boundary phase transformations in an elemental metal," *Nature* **579**, 375–378 (2020).
- ²¹⁰C. W. Glass, A. R. Oganov, and N. Hansen, "USPEX—Evolutionary crystal structure prediction," *Comput. Phys. Commun.* **175**, 713–720 (2006).
- ²¹¹M. P. Harmer, "The phase behavior of interfaces," *Science* **332**, 182–183 (2011).
- ²¹²M. Tang, W. C. Carter, and R. M. Cannon, "Grain boundary transitions in binary alloys," *Phys. Rev. Lett.* **97**, 075502 (2006).
- ²¹³J. Luo, H. Cheng, K. M. Asl, C. J. Kiely, and M. P. Harmer, "The role of a bilayer interfacial phase on liquid metal embrittlement," *Science* **333**, 1730–1733 (2011).
- ²¹⁴J. Q. Broughton and G. H. Gilmer, "Thermodynamic criteria for grain-boundary melting: A molecular-dynamics study," *Phys. Rev. Lett.* **56**, 2692–2695 (1986).
- ²¹⁵S. R. Phillpot, J. F. Lutsko, D. Wolf, and S. Yip, "Molecular-dynamics study of lattice-defect-nucleated melting in silicon," *Phys. Rev. B* **40**, 2831–2840 (1989).
- ²¹⁶S. Divinski, M. Lohmann, C. Herzig, B. Straumal, B. Baretzky, and W. Gust, "Grain-boundary melting phase transition in the Cu–Bi system," *Phys. Rev. B* **71**, 104104 (2005).
- ²¹⁷A. M. Alsayed, M. F. Islam, J. Zhang, P. J. Collings, and A. G. Yodh, "Premelting at defects within bulk colloidal crystals," *Science* **309**, 1207–1210 (2005).
- ²¹⁸M. A. Gibson and C. A. Schuh, "A survey of ab-initio calculations shows that segregation-induced grain boundary embrittlement is predicted by bond-breaking arguments," *Scr. Mater.* **113**, 55–58 (2016).
- ²¹⁹P. Lejček, M. Šob, and V. Paidar, "Interfacial segregation and grain boundary embrittlement: An overview and critical assessment of experimental data and calculated results," *Prog. Mater. Sci.* **87**, 83–139 (2017).
- ²²⁰Y. Mishin, M. Asta, and J. Li, "Atomistic modeling of interfaces and their impact on microstructure and properties," *Acta Mater.* **58**, 1117–1151 (2010).
- ²²¹J. W. Somerville, A. Sobkowiak, N. Tapia-Ruiz, J. Billaud, J. G. Lozano, R. A. House, L. C. Gallington, T. Ericsson, L. Häggström, M. R. Roberts, U. Maitra, and P. G. Bruce, "Nature of the 'Z'-phase in layered Na-ion battery cathodes," *Energy Environ. Sci.* **12**, 2223–2232 (2019).
- ²²²G. Frommeyer, U. Brück, and P. Neumann, "Supra-ductile and high-strength manganese-TRIP/TWIP steels for high energy absorption purposes," *ISIJ Int.* **43**, 438–446 (2003).
- ²²³T. Hickel, S. Sandlöbes, R. Marceau, A. Dick, I. Bleskov, J. Neugebauer, and D. Raabe, "Impact of nanodiffusion on the stacking fault energy in high-strength steels," *Acta Mater.* **75**, 147–155 (2014).
- ²²⁴H. He, M. Naeem, F. Zhang, Y. Zhao, S. Harjo, T. Kawasaki, B. Wang, X. Wu, S. Lan, Z. Wu, W. Yin, Y. Wu, Z. Lu, J.-J. Kai, C.-T. Liu, and X.-L. Wang, "Stacking fault driven phase transformation in CrCoNi medium entropy alloy," *Nano Lett.* **21**, 1419–1426 (2021).
- ²²⁵S. M. Sharma, S. J. Turneaure, J. M. Winey, and Y. M. Gupta, "What determines the fcc-bcc structural transformation in shock compressed noble metals?," *Phys. Rev. Lett.* **124**, 235701 (2020).
- ²²⁶P. J. H. Denteneer and W. van Haeringen, "Stacking-fault energies in semiconductors from first-principles calculations," *J. Phys. C: Solid State Phys.* **20**, L883–L887 (1987).
- ²²⁷P. Denteneer and J. Soler, "Energetics of point and planar defects in aluminium from first-principles calculations," *Solid State Commun.* **78**, 857–861 (1991).
- ²²⁸F. Chu, A. H. Ormeci, T. E. Mitchell, J. M. Wills, D. J. Thoma, R. C. Albers, and S. P. Chen, "Stacking fault energy of the NbCr₂ laves phase," *Philos. Mag. Lett.* **72**, 147–153 (1995).
- ²²⁹M. Šlapáková, A. Zendegani, C. Liebscher, T. Hickel, J. Neugebauer, T. Hammerschmidt, A. Ormeci, J. Grin, G. Dehm, K. Kumar, and F. Stein, "Atomic scale configuration of planar defects in the Nb-rich C14 Laves phase NbFe₂," *Acta Mater.* **183**, 362–376 (2020).
- ²³⁰C. Delmas, C. Fouassier, and P. Hagenmuller, "Structural classification and properties of the layered oxides," *Phys. B+C* **99**, 81–85 (1980).
- ²³¹K. Kubota, N. Yabuuchi, H. Yoshida, M. Dahbi, and S. Komaba, "Layered oxides as positive electrode materials for Na-ion batteries," *MRS Bull.* **39**, 416–422 (2014).
- ²³²D. Kundu, E. Talaie, V. Duffort, and L. F. Nazar, "The emerging chemistry of sodium ion batteries for electrochemical energy storage," *Angew. Chem. Int. Ed.* **54**, 3431–3448 (2015).
- ²³³Y. Yoda, K. Kubota, H. Isozumi, T. Horiba, and S. Komaba, "Poly- γ -glutamate binder to enhance electrode performances of P2-Na_{2/3}[Ni_{1/3}Mn_{2/3}O₂] for Na-ion batteries," *ACS Appl. Mater. Interfaces* **10**, 10986–10997 (2018).
- ²³⁴Z. Lu and J. R. Dahn, "In situ x-ray diffraction study of P2-Na_{2/3}[Ni_{1/3}Mn_{2/3}O₂]," *J. Electrochem. Soc.* **148**, A1225 (2001).
- ²³⁵D. H. Lee, J. Xu, and Y. S. Meng, "An advanced cathode for Na-ion batteries with high rate and excellent structural stability," *Phys. Chem. Chem. Phys.* **15**, 3304 (2013).
- ²³⁶N. Yabuuchi, M. Kajiyama, J. Iwatate, H. Nishikawa, S. Hitomi, R. Okuyama, R. Usui, Y. Yamada, and S. Komaba, "P2-type Na_x[Fe_{1/2}Mn_{1/2}]O₂ made from earth-abundant elements for rechargeable Na batteries," *Nat. Mater.* **11**, 512–517 (2012).
- ²³⁷E. Talaie, V. Duffort, H. L. Smith, B. Fultz, and L. F. Nazar, "Structure of the high voltage phase of layered P2-Na_{2/3-z}[Mn_{1/2}Fe_{1/2}]O₂ and the positive effect of Ni substitution on its stability," *Energy Environ. Sci.* **8**, 2512–2523 (2015).
- ²³⁸B. Mortemard de Boisse, D. Carlier, M. Guignard, L. Bourgeois, and C. Delmas, "P2-Na_xMn_{1/2}Fe_{1/2}O₂ Phase used as positive electrode in na batteries: structural changes induced by the electrochemical (De)intercalation process," *Inorg. Chem.* **53**, 11197–11205 (2014).
- ²³⁹J. W. Somerville, R. A. House, N. Tapia-Ruiz, A. Sobkowiak, S. Ramos, A. V. Chadwick, M. R. Roberts, U. Maitra, and P. G. Bruce, "Identification and characterisation of high energy density P2-type Na_{2/3}[Ni_{1/3-y/2}Mn_{2/3-y/2}Fe_y]O₂ compounds for Na-ion batteries," *J. Mater. Chem. A* **6**, 5271–5275 (2018).
- ²⁴⁰G. Wilde, "Structural phase transformations in nanoscale systems," *Adv. Eng. Mater.* **23**, 2001387 (2021).
- ²⁴¹L. Roelofs, "Phase transitions and kinetics of ordering," in *Handbook of Surface Science* (Elsevier, 1996), Vol. 1, pp. 713–807.
- ²⁴²*Spontaneous Ordering in Semiconductor Alloys*, edited by A. Mascarenhas (Springer, Boston, 2002).
- ²⁴³J. Perepezko and G. Wilde, "Melt undercooling and nucleation kinetics," *Curr. Opin. Solid State Mater. Sci.* **20**, 3–12 (2016).
- ²⁴⁴J. Perepezko, J. Sebright, P. Höckel, and G. Wilde, "Undercooling and solidification of atomized liquid droplets," *Mater. Sci. Eng. A* **326**, 144–153 (2002).
- ²⁴⁵J. H. Perepezko, "Nucleation in undercooled liquids," *Mater. Sci. Eng.* **65**, 125–135 (1984).
- ²⁴⁶D. Turnbull and R. E. Cech, "Microscopic observation of the solidification of small metal droplets," *J. Appl. Phys.* **21**, 804–810 (1950).
- ²⁴⁷F. J. Bradshaw, M. E. Gasper, and S. Pearson, "The supercooling of gold as affected by some catalysts," *J. Inst. Met.* **87**, 15–18 (1958).
- ²⁴⁸G. Wilde, J. Sebright, and J. Perepezko, "Bulk liquid undercooling and nucleation in gold," *Acta Mater.* **54**, 4759–4769 (2006).
- ²⁴⁹J. Fehling and E. Scheil, "Untersuchung der Unterkühlbarkeit von Metallschmelzen," *Int. J. Mater. Res.* **53**, 593–600 (1962).
- ²⁵⁰M. Mayo, A. Suresh, and W. Porter, "Thermodynamics for nanosystems: Grain and particle-size dependent phase diagrams," *Rev. Adv. Mater. Sci.* **5**, 100–109 (2003).
- ²⁵¹B. D. Begg, E. R. Vance, and J. Nowotny, "Effect of particle size on the room-temperature crystal structure of barium titanate," *J. Am. Ceram. Soc.* **77**, 3186–3192 (1994).
- ²⁵²S. Schlag, H.-F. Eicke, and W. B. Stern, "Size driven phase transition and thermodynamic properties of nanocrystalline BaTiO₃," *Ferroelectrics* **173**, 351–369 (1995).
- ²⁵³M. H. Frey and D. A. Payne, "Grain-size effect on structure and phase transformations for barium titanate," *Phys. Rev. B* **54**, 3158–3168 (1996).

- ²⁵⁴G. A. Rossetti, J. P. Cline, and A. Navrotsky, "Phase transition energetics and thermodynamic properties of ferroelectric PbTiO_3 ," *J. Mater. Res.* **13**, 3197–3206 (1998).
- ²⁵⁵E. K. Akdogan, W. Mayo, A. Safari, C. J. Rawn, and E. A. Payzant, "Structure-property relations in mesoscopic BaTiO_3 and PbTiO_3 ," *Ferroelectrics* **223**, 11–18 (1999).
- ²⁵⁶H. Sato, O. Kitakami, T. Sakurai, Y. Shimada, Y. Otani, and K. Fukamichi, "Structure and magnetism of hcp-Co fine particles," *J. Appl. Phys.* **81**, 1858–1862 (1997).
- ²⁵⁷W. Shi, J. Kong, H. Shen, G. Du, W. Yao, and Z. Qi, "An investigation of anomalous structure of nanocrystal Ti and Zr films," *Vacuum* **42**, 1070–1071 (1991).
- ²⁵⁸H. Zhang and J. F. Banfield, "Thermodynamic analysis of phase stability of nanocrystalline titania," *J. Mater. Chem.* **8**, 2073–2076 (1998).
- ²⁵⁹C.-C. Chen, A. B. Herhold, C. S. Johnson, and A. P. Alivisatos, "Size dependence of structural metastability in semiconductor nanocrystals," *Science* **276**, 398–401 (1997).
- ²⁶⁰S. H. Tolbert and A. P. Alivisatos, "Size Dependence of a First Order Solid-Solid Phase Transition: The Wurtzite to Rock Salt Transformation in CdSe Nanocrystals," *Science* **265**, 373–376 (1994).
- ²⁶¹A. Suresh, M. J. Mayo, W. D. Porter, and C. J. Rawn, "Crystallite and grain-size-dependent phase transformations in yttria-doped zirconia," *J. Am. Ceram. Soc.* **86**, 360–362 (2003).
- ²⁶²A. Suresh, M. J. Mayo, and W. D. Porter, "Thermodynamics of the tetragonal-to-monoclinic phase transformation in fine and nanocrystalline yttria-stabilized zirconia powders," *J. Mater. Res.* **18**, 2912–2921 (2003).
- ²⁶³G. Skandan, C. Foster, H. Frase, M. Ali, J. Parker, and H. Hahn, "Phase characterization and stabilization due to grain size effects of nanostructured Y_2O_3 ," *Nanostruct. Mater.* **1**, 313–322 (1992).
- ²⁶⁴H. G. Scott, "Phase relationships in the zirconia-yttria system," *J. Mater. Sci.* **10**, 1527–1535 (1975).
- ²⁶⁵M. Grünwald, E. Rabani, and C. Dellago, "Mechanisms of the wurtzite to rocksalt transformation in CdSe nanocrystals," *Phys. Rev. Lett.* **96**, 255701 (2006).
- ²⁶⁶M. Grünwald, C. Dellago, and P. L. Geissler, "An efficient transition path sampling algorithm for nanoparticles under pressure," *J. Chem. Phys.* **127**, 154718 (2007).
- ²⁶⁷M. Grünwald and C. Dellago, "Transition state analysis of solid-solid transformations in nanocrystals," *J. Chem. Phys.* **131**, 164116 (2009).
- ²⁶⁸M. Grünwald and C. Dellago, "Nucleation and growth in structural transformations of nanocrystals," *Nano Lett.* **9**, 2099–2102 (2009).
- ²⁶⁹M. Park and C. A. Schuh, "Accelerated sintering in phase-separating nanostructured alloys," *Nat. Commun.* **6**, 6858 (2015).
- ²⁷⁰A. V. Shishulin and V. B. Fedoseev, "Size effect in the phase separation of Cr–W solid solutions," *Inorg. Mater.* **54**, 546–549 (2018).
- ²⁷¹A. S. Shirinyan, "Two-phase equilibrium states in individual Cu–Ni nanoparticles: Size, depletion and hysteresis effects," *Beilstein J. Nanotechnol.* **6**, 1811–1820 (2015).
- ²⁷²Y. Iguchi, G. L. Katona, C. Cserhádi, G. A. Langer, and Z. Erdélyi, "On the miscibility gap of Cu–Ni system," *Acta Mater.* **148**, 49–54 (2018).
- ²⁷³R. Duran, P. Stender, S. M. Eich, and G. Schmitz, "Atom probe study of the miscibility gap in CuNi thin films and microstructure development," *Microsc. Microanal.* **28**, 1359–1369 (2022).
- ²⁷⁴J. B. Hannon, H. Hibino, N. C. Bartelt, B. S. Swartzentruber, T. Ogino, and G. L. Kellogg, "Dynamics of the silicon (111) surface phase transition," *Nature* **405**, 552–554 (2000).
- ²⁷⁵D. Segev and C. G. Van de Walle, "Surface reconstructions on InN and GaN polar and nonpolar surfaces," *Surf. Sci.* **601**, L15–L18 (2007).
- ²⁷⁶M. S. Miao, A. Janotti, and C. G. Van de Walle, "Reconstructions and origin of surface states on AlN polar and nonpolar surfaces," *Phys. Rev. B* **80**, 155319 (2009).
- ²⁷⁷J. Neugebauer, T. Zywiets, M. Scheffler, J. E. Northrup, and C. G. Van de Walle, "Clean and As-covered zinc-blende GaN (001) Surfaces: Novel surface structures and surfactant behavior," *Phys. Rev. Lett.* **80**, 3097–3100 (1998).
- ²⁷⁸C. G. Van de Walle and J. Neugebauer, "Role of hydrogen in surface reconstructions and growth of GaN," *J. Vac. Sci. Technol., B* **20**, 1640 (2002).
- ²⁷⁹W. Pitsch, "The martensite transformation in thin foils of iron-nitrogen alloys," *Philos. Mag.* **4**, 577–584 (1959).
- ²⁸⁰W. A. A. Macedo and W. Keune, "Magnetism of epitaxial fcc-Fe(100) films on Cu(100) investigated *in situ* by conversion-electron Mössbauer spectroscopy in ultrahigh vacuum," *Phys. Rev. Lett.* **61**, 475–478 (1988).
- ²⁸¹J. Thomassen, F. May, B. Feldmann, M. Wuttig, and H. Ibach, "Magnetic live surface layers in Fe/Cu(100)," *Phys. Rev. Lett.* **69**, 3831–3834 (1992).
- ²⁸²S. Müller, P. Bayer, C. Reischl, K. Heinz, B. Feldmann, H. Zillgen, and M. Wuttig, "Structural instability of ferromagnetic fcc Fe Films on Cu(100)," *Phys. Rev. Lett.* **74**, 765–768 (1995).
- ²⁸³R. E. Schlier and H. E. Farnsworth, "Structure and adsorption characteristics of clean surfaces of germanium and silicon," *J. Chem. Phys.* **30**, 917–926 (1959).
- ²⁸⁴K. Takayanagi, Y. Tanishiro, M. Takahashi, and S. Takahashi, "Structural analysis of Si(111)- 7×7 by UHV-transmission electron diffraction and microscopy," *J. Vac. Sci. Technol., A* **3**, 1502–1506 (1985).
- ²⁸⁵L. Hu, B. Huang, and F. Liu, "Atomistic mechanism underlying the Si(111)- (7×7) surface reconstruction revealed by artificial neural-network potential," *Phys. Rev. Lett.* **126**, 176101 (2021).
- ²⁸⁶S. Froyen and A. Zunger, "Surface-induced ordering in GaInP," *Phys. Rev. Lett.* **66**, 2132–2135 (1991).
- ²⁸⁷J. Wang, A. J. Davenport, H. S. Isaacs, and B. M. Ocko, "Surface charge—Induced ordering of the Au(111) surface," *Science* **255**, 1416–1418 (1992).
- ²⁸⁸J. E. Northrup, L. T. Romano, and J. Neugebauer, "Surface energetics, pit formation, and chemical ordering in InGaN alloys," *Appl. Phys. Lett.* **74**, 2319–2321 (1999).
- ²⁸⁹S. M ller, "Bulk and surface ordering phenomena in binary metal alloys," *J. Phys.: Condens. Matter* **15**, R1429–R1500 (2003).
- ²⁹⁰B. C. Han, A. Van der Ven, G. Ceder, and B.-J. Hwang, "Surface segregation and ordering of alloy surfaces in the presence of adsorbates," *Phys. Rev. B* **72**, 205409 (2005).
- ²⁹¹M. Albrecht, L. Lymperakis, J. Neugebauer, J. E. Northrup, L. Kirste, M. Leroux, I. Grzegory, S. Porowski, and H. P. Strunk, "Chemically ordered $\text{Al}_x\text{Ga}_{1-x}\text{N}$ alloys: Spontaneous formation of natural quantum wells," *Phys. Rev. B* **71**, 035314 (2005).
- ²⁹²L. Lymperakis, T. Schulz, C. Freysoldt, M. Anikeeva, Z. Chen, X. Zheng, B. Shen, C. Chêze, M. Siekacz, X. Q. Wang, M. Albrecht, and J. Neugebauer, "Elastically frustrated rehybridization: Origin of chemical order and compositional limits in InGaN quantum wells," *Phys. Rev. Mater.* **2**, 011601 (2018).
- ²⁹³R. Witte, T. Feng, J. X. Fang, A. Fischer, M. Ghafari, R. Kruk, R. A. Brand, D. Wang, H. Hahn, and H. Gleiter, "Evidence for enhanced ferromagnetism in an iron-based nanoglass," *Appl. Phys. Lett.* **103**, 073106 (2013).
- ²⁹⁴D. Şopu, K. Albe, Y. Ritter, and H. Gleiter, "From nanoglasses to bulk massive glasses," *Appl. Phys. Lett.* **94**, 191911 (2009).
- ²⁹⁵M. Ghafari, S. Kohara, H. Hahn, H. Gleiter, T. Feng, R. Witte, and S. Kamali, "Structural investigations of interfaces in $\text{Fe}_{90}\text{Sc}_{10}$ nanoglasses using high-energy x-ray diffraction," *Appl. Phys. Lett.* **100**, 133111 (2012).
- ²⁹⁶H. Gleiter, T. Schimmel, and H. Hahn, "Nanostructured solids—From nanoglasses to quantum transistors," *Nano Today* **9**, 17–68 (2014).
- ²⁹⁷H. Gleiter, "Nanoglasses: A new kind of noncrystalline material and the way to an age of new technologies?," *Small* **12**, 2225–2233 (2016).
- ²⁹⁸S. Kauffmann-Weiss, M. E. Gruner, A. Backen, L. Schultz, P. Entel, and S. Fähler, "Magnetic nanostructures by adaptive twinning in strained epitaxial films," *Phys. Rev. Lett.* **107**, 206105 (2011).
- ²⁹⁹M. A. Uijtewaal, T. Hickel, J. Neugebauer, M. E. Gruner, and P. Entel, "Understanding the phase transitions of the NiMnGa magnetic shape memory system from first principles," *Phys. Rev. Lett.* **102**, 035702 (2009).
- ³⁰⁰B. Dutta, A. Çakır, C. Giacobbe, A. Al-Zubi, T. Hickel, M. Acet, and J. Neugebauer, "Ab initio prediction of martensitic and intermartensitic phase boundaries in Ni–Mn–Ga," *Phys. Rev. Lett.* **116**, 025503 (2016).
- ³⁰¹K. Ullakko, J. K. Huang, C. Kantner, R. C. O'Handley, and V. V. Kokorin, "Large magnetic-field-induced strains in Ni_2MnGa single crystals," *Appl. Phys. Lett.* **69**, 1966–1968 (1996).
- ³⁰²A. Sozinov, A. A. Likhachev, N. Lanska, and K. Ullakko, "Giant magnetic-field-induced strain in NiMnGa seven-layered martensitic phase," *Appl. Phys. Lett.* **80**, 1746–1748 (2002).

- ³⁰³T. Krenke, E. Duman, M. Acet, E. F. Wassermann, X. Moya, L. Mañosa, A. Planes, E. Suard, and B. Ouladidaf, "Magnetic superelasticity and inverse magnetocaloric effect in Ni–Mn–In," *Phys. Rev. B* **75**, 104414 (2007).
- ³⁰⁴R. Niemann, U. K. Röfßler, M. E. Gruner, O. Heczko, L. Schultz, and S. Fähler, "The role of adaptive martensite in magnetic shape memory alloys," *Adv. Eng. Mater.* **14**, 562–581 (2012).
- ³⁰⁵J. Duncan, A. Harjunmaa, R. Terrell, R. Drautz, G. Henkelman, and J. Rogal, "Collective atomic displacements during complex phase boundary migration in solid-solid phase transformations," *Phys. Rev. Lett.* **116**, 035701 (2016).
- ³⁰⁶J. Rogal, E. Schneider, and M. E. Tuckerman, "Neural-network-based path collective variables for enhanced sampling of phase transformations," *Phys. Rev. Lett.* **123**, 245701 (2019).
- ³⁰⁷J. Rogal and M. E. Tuckerman, "Pathways in classification space: Machine learning as a route to predicting kinetics of structural transitions in atomic crystals," in *Multiscale Dynamics Simulations: Nano and Nano-bio Systems in Complex Environments*, Theoretical and Computational Chemistry Series, edited by D. R. Salahub and D. Wei (Royal Society of Chemistry, Cambridge, 2021), Chap. 11, pp. 312–348.
- ³⁰⁸A. G. Khachatryan, S. M. Shapiro, and S. Semenovskaya, "Adaptive phase formation in martensitic transformation," *Phys. Rev. B* **43**, 10832–10843 (1991).
- ³⁰⁹A. G. Khachatryan, S. M. Shapiro, and S. Semenovskaya, "Adaptive phase in martensitic transformation," *Mater. Trans. JIM* **33**, 278–281 (1992).
- ³¹⁰S. Kaufmann, U. K. Röfßler, O. Heczko, M. Wuttig, J. Buschbeck, L. Schultz, and S. Fähler, "Adaptive modulations of martensites," *Phys. Rev. Lett.* **104**, 145702 (2010).
- ³¹¹A. K. Sinha, "Topologically close-packed structures of transition metal alloys," *Prog. Mater. Sci.* **15**, 81–185 (1972).
- ³¹²C. Rae and R. Reed, "The precipitation of topologically close-packed phases in rhenium-containing superalloys," *Acta Mater.* **49**, 4113–4125 (2001).
- ³¹³A. Ladines, T. Hammerschmidt, and R. Drautz, "Structural stability of Fe-based topologically close-packed phases," *Intermetallics* **59**, 59–67 (2015).
- ³¹⁴D. Choi, B. Wang, S. Chung, X. Liu, A. Darbal, A. Wise, N. T. Nuhfer, K. Barmak, A. P. Warren, K. R. Coffey, and M. F. Toney, "Phase, grain structure, stress, and resistivity of sputter-deposited tungsten films," *J. Vac. Sci. Technol., A* **29**, 051512 (2011).
- ³¹⁵D. Choi, C. S. Kim, D. Naveh, S. Chung, A. P. Warren, N. T. Nuhfer, M. F. Toney, K. R. Coffey, and K. Barmak, "Electron mean free path of tungsten and the electrical resistivity of epitaxial (110) tungsten films," *Phys. Rev. B* **86**, 045432 (2012).
- ³¹⁶A. J. Knowles, D. Dye, R. J. Dodds, A. Watson, C. D. Hardie, and S. A. Humphry-Baker, "Tungsten-based bcc-superalloys," *Appl. Mater. Today* **23**, 110104 (2021).
- ³¹⁷C.-F. Pai, L. Liu, Y. Li, H. W. Tseng, D. C. Ralph, and R. A. Buhrman, "Spin transfer torque devices utilizing the giant spin Hall effect of tungsten," *Appl. Phys. Lett.* **101**, 122404 (2012).
- ³¹⁸Q. Hao, W. Chen, and G. Xiao, "Beta (β) tungsten thin films: Structure, electron transport, and giant spin Hall effect," *Appl. Phys. Lett.* **106**, 182403 (2015).
- ³¹⁹M. Costa, A. T. Costa, J. Hu, R. Q. Wu, and R. B. Muniz, " β -tungsten: A promising metal for spintronics," *J. Phys.: Condens. Matter* **30**, 305802 (2018).
- ³²⁰K. Barmak, J. Liu, L. Harlan, P. Xiao, J. Duncan, and G. Henkelman, "Transformation of topologically close-packed β -W to body-centered cubic α -W: Comparison of experiments and computations," *J. Chem. Phys.* **147**, 152709 (2017).
- ³²¹K. Nakajima, M. Apel, and I. Steinbach, "The role of carbon diffusion in ferrite on the kinetics of cooperative growth of pearlite: A multi-phase field study," *Acta Mater.* **54**, 3665–3672 (2006).
- ³²²A. Chattaraj, M. Balal, A. K. Yadav, S. R. Barman, A. K. Sinha, S. N. Jha, S. Joulie, V. Serin, A. Claverie, V. Kumar, and A. Kanjilal, "Unravelling oxygen driven α to β phase transformation in tungsten," *Sci. Rep.* **10**, 14718 (2020).
- ³²³X. Sun, D. Wu, L. Zou, S. D. House, X. Chen, M. Li, D. N. Zakharov, J. C. Yang, and G. Zhou, "Dislocation-induced stop-and-go kinetics of interfacial transformations," *Nature* **607**, 708–713 (2022).
- ³²⁴S. J. Dillon, M. Tang, W. C. Carter, and M. P. Harmer, "Complexion: A new concept for kinetic engineering in materials science," *Acta Mater.* **55**, 6208–6218 (2007).
- ³²⁵X. Zhang, T. Hickel, J. Rogal, S. Fähler, R. Drautz, and J. Neugebauer, "Structural transformations among austenite, ferrite and cementite in Fe–C alloys: A unified theory based on *ab initio* simulations," *Acta Mater.* **99**, 281–289 (2015).
- ³²⁶M. Durand-Charre, "The microstructure of steels and cast irons," in *Engineering Materials and Processes* (Springer, Berlin, New York, 2004).
- ³²⁷J. Zhang, C. C. Tasan, M. J. Lai, A. C. Dippel, and D. Raabe, "Complexion-mediated martensitic phase transformation in titanium," *Nat. Commun.* **8**, 14210 (2017).
- ³²⁸H. Wang, X. Zhang, D. Yan, C. Somsen, and G. Eggeler, "Interface dominated cooperative nanoprecipitation in interstitial alloys," *Nat. Commun.* **9**, 4017 (2018).
- ³²⁹G. Bussi and A. Laio, "Using metadynamics to explore complex free-energy landscapes," *Nat. Rev. Phys.* **2**, 200–212 (2020).
- ³³⁰F. Pietrucci, "Novel enhanced sampling strategies for transitions between ordered and disordered structures," in *Handbook of Materials Modeling*, edited by W. Andreoni and S. Yip (Springer International Publishing, Cham, 2020), pp. 597–619.
- ³³¹H. Sidky, W. Chen, and A. L. Ferguson, "Machine learning for collective variable discovery and enhanced sampling in biomolecular simulation," *Mol. Phys.* **118**, e1737742 (2020).
- ³³²J. Wang, P. R. Arantes, A. Bhattarai, R. V. Hsu, S. Pawnikar, Y.-m. M. Huang, G. Palermo, and Y. Miao, "Gaussian accelerated molecular dynamics: Principles and applications," *WIREs Comput. Mol. Sci.* **11**, e1521 (2021).
- ³³³N. Kondratyuk, V. Nikolskiy, D. Pavlov, and V. Stegailov, "GPU-accelerated molecular dynamics: State-of-art software performance and porting from Nvidia CUDA to AMD HIP," *Int. J. High Perform. Comput. Appl.* **35**, 312–324 (2021).
- ³³⁴J. Xu, X.-M. Cao, and P. Hu, "Accelerating metadynamics-based free-energy calculations with adaptive machine learning potentials," *J. Chem. Theory Comput.* **17**, 4465–4476 (2021).
- ³³⁵Q. Tong, X. Luo, A. A. Adeleke, P. Gao, Y. Xie, H. Liu, Q. Li, Y. Wang, J. Lv, Y. Yao, and Y. Ma, "Machine learning metadynamics simulation of reconstructive phase transition," *Phys. Rev. B* **103**, 054107 (2021).
- ³³⁶S. Biswas and B. M. Wong, "*Ab initio* metadynamics calculations reveal complex interfacial effects in acetic acid deprotonation dynamics," *J. Mol. Liq.* **330**, 115624 (2021).
- ³³⁷J. Yin, Z. Pei, and M. C. Gao, "Neural network-based order parameter for phase transitions and its applications in high-entropy alloys," *Nat. Comput. Sci.* **1**, 686–693 (2021).
- ³³⁸Z. Li, K. Meidani, P. Yadav, and A. Barati Farimani, "Graph neural networks accelerated molecular dynamics," *J. Chem. Phys.* **156**, 144103 (2022).
- ³³⁹J. C. Snyder, M. Rupp, K. Hansen, K.-R. Müller, and K. Burke, "Finding density functionals with machine learning," *Phys. Rev. Lett.* **108**, 253002 (2012).
- ³⁴⁰A. Ryabov, I. Akhatov, and P. Zhilyaev, "Neural network interpolation of exchange-correlation functional," *Sci. Rep.* **10**, 8000 (2020).
- ³⁴¹M. F. Kasim and S. M. Vinko, "Learning the exchange-correlation functional from nature with fully differentiable density functional theory," *Phys. Rev. Lett.* **127**, 126403 (2021).
- ³⁴²R. Nagai, R. Akashi, and O. Sugino, "Machine-learning-based exchange correlation functional with physical asymptotic constraints," *Phys. Rev. Res.* **4**, 013106 (2022).
- ³⁴³X. Zhang, B. Grabowski, F. Körmann, A. V. Ruban, Y. Gong, R. C. Reed, T. Hickel, and J. Neugebauer, "Temperature dependence of the stacking-fault Gibbs energy for Al, Cu, and Ni," *Phys. Rev. B* **98**, 224106 (2018).
- ³⁴⁴L. Monacelli and F. Mauri, "Time-dependent self-consistent harmonic approximation: Anharmonic nuclear quantum dynamics and time correlation functions," *Phys. Rev. B* **103**, 104305 (2021).
- ³⁴⁵L. Monacelli, R. Bianco, M. Cherubini, M. Calandra, I. Errea, and F. Mauri, "The stochastic self-consistent harmonic approximation: Calculating vibrational properties of materials with full quantum and anharmonic effects," *J. Phys.: Condens. Matter* **33**, 363001 (2021).
- ³⁴⁶R. Masuki, T. Nomoto, R. Arita, and T. Tadano, "Ab-initio structural optimization at finite temperatures based on anharmonic phonon theory: Application to the structural phase transitions of BaTiO₃," *arXiv:2205.08789* (2022).

- ³⁴⁷I. Novikov, B. Grabowski, F. Körmann, and A. Shapeev, “Magnetic Moment Tensor Potentials for collinear spin-polarized materials reproduce different magnetic states of bcc Fe,” *npj Comput. Mater.* **8**, 13 (2022).
- ³⁴⁸J. F. Nie, Y. M. Zhu, J. Z. Liu, and X. Y. Fang, “Periodic segregation of solute atoms in fully coherent twin boundaries,” *Sci.* **340**, 957–960 (2013).
- ³⁴⁹M. L. Bowers, C. Ophus, A. Gautam, F. Lançon, and U. Dahmen, “Step coalescence by collective motion at an incommensurate grain boundary,” *Phys. Rev. Lett.* **116**, 106102 (2016).
- ³⁵⁰J. Heo, D. Dumett Torres, P. Banerjee, and P. K. Jain, “*In situ* electron microscopy mapping of an order-disorder transition in a superionic conductor,” *Nat. Commun.* **10**, 1505 (2019).
- ³⁵¹A. J. Shahani, X. Xiao, E. M. Lauridsen, and P. W. Voorhees, “Characterization of metals in four dimensions,” *Mater. Res. Lett.* **8**, 462–476 (2020).
- ³⁵²C. He, Z. Li, H. Chen, N. Wilson, and J.-F. Nie, “Unusual solute segregation phenomenon in coherent twin boundaries,” *Nat. Commun.* **12**, 722 (2021).
- ³⁵³J. Nie, C. Hu, Q. Yan, and J. Luo, “Discovery of electrochemically induced grain boundary transitions,” *Nat. Commun.* **12**, 2374 (2021).
- ³⁵⁴X. Chen, Q. Wang, Z. Cheng, M. Zhu, H. Zhou, P. Jiang, L. Zhou, Q. Xue, F. Yuan, J. Zhu, X. Wu, and E. Ma, “Direct observation of chemical short-range order in a medium-entropy alloy,” *Nature* **592**, 712–716 (2021).
- ³⁵⁵M. Liu and J. Weissmüller, “Imaging the deformation-induced accumulation of defects in nanoporous gold,” *Mater. Res. Lett.* **9**, 359–365 (2021).
- ³⁵⁶H. Sheng, L. Zhang, H. Zhang, J. Wang, J. Eckert, and C. Gammer, “*In situ* TEM observation of phase transformation in bulk metallic glass composites,” *Mater. Res. Lett.* **9**, 189–194 (2021).
- ³⁵⁷X. Peng, F.-C. Zhu, Y.-H. Jiang, J.-J. Sun, L.-P. Xiao, S. Zhou, K. C. Bustillo, L.-H. Lin, J. Cheng, J.-F. Li, H.-G. Liao, S.-G. Sun, and H. Zheng, “Identification of a quasi-liquid phase at solid–liquid interface,” *Nat. Commun.* **13**, 3601 (2022).